Photoluminescence of High Quality Epitaxial p-type InN

Young-Wook Song

A thesis submitted in partial fulfillment
of the requirements for the degree of
Doctor of Philosophy in Physics
at the
University of Canterbury,
Christchurch, New Zealand

February 2013

Abstract

Indium nitride (InN) is a group III-V semiconductor that is part of the Al,Ga:N family. It is an infrared bandgap semiconductor with great potential for use in photovoltaic applications. Being an intrinsically n-type material, p-type doping is naturally one of the ongoing hot topics in InN research, which is of interest in the fabrication of pn junctions.

Plasma-assisted molecular beam epitaxy (PAMBE) grown Mg doped InN thin film was investigated via systematic optical characterizations. Photoluminescence (PL) measurement has been a key part of the research, exhibiting a wide range of spectral lines between 0.54 and 0.67 eV. In a critical Mg concentration range of 2.6×10^{17} and 1.0×10^{18} cm^{-3}, a strong luminescence line at 0.6 eV has been associated with a Mg-related deep acceptor. Correspondingly, a variable magnetic field Hall (VFH) effect measurement has successfully probed a buried hole-mediated conductivity path underneath a surface electron accumulation layer. This specific doping range also led to a manifestation of a "true" band-to-band transition at 0.67 eV. Such an observation has not previously been reported for InN and in our case this assignment is convincingly supported by the quadratic characteristic of the excitation power law. This established that a rigorous control of Mg flux can sufficiently compensate the background electron concentration of InN via the substitutional incorporation on In sites (Mg_{In}). However, introduction of donor-like complexes somewhat suppressed this process if too much Mg or even alternative dopants such as Zn and Mn were used. Also distinctively observed was a strongly quenched PL quantum efficiency from heavily doped films, where time-resolved differential transmission (TRDT) measurement showed a bi-exponential carrier lifetime decay curve owing to the onset of Auger recombination processes. These observations certainly have profound implications for devices and beyond.

Acknowledgements

Firstly, I would like to express my special thanks to my senior supervisor, Prof. Roger Reeves. It is impossible to complete this project without his great guidance, and amazing support. I also would like to sincerely thank my co-supervisor, Assoc. Prof. Steven Durbin for his never-ending enthusiasm towards this research and priceless advice.

Without the technicians, the operation of many useful experiments in the laser laboratory is beyond conception. I am very grateful to Mr. Wayne Smith, Mr. Graham MacDonald, Mr. Geoff Graham, and Mr. Bob Flygenring for their excellent assistance for the technical support and liquid Helium supply.

The coordination of the MBE growth and Hall measurements provided the fruitful path for development of my PhD thesis. These important experiments were performed by Dr. Chito Kendrick and Dr. Jessica Chai from the Department of Electrical and Computer Engineering, whose great contributions were much appreciated. The condensed matter research group in the Department of Physics and Astronomy also deserves an extra special mention here. I am indebted to Dr. Scott Choi, Dr. Ian Farrell, Dr. Martin Henseler, Dr. Rueben Mendelsberg, Dr. Paul Miller, and Mr. Masaed Almotari for sharing the wonderful experience of Physics and making the PhD student life very enjoyable.

I would like to acknowledge the Department of Physics and Astronomy and the MacDiarmid Institute for Advanced Materials and Nanotechnology for scholarships for the project and allowing me to undertake a PhD thesis.

I would like to extend huge warm thanks to my family. I must thank my parents for their moral support throughout many years. Last but not least, I would like to pay high regards to my wife, HyunJung and my son, Anthony for their sincere encouragement and endless love. I owe everything to them.

Contents

Abstract ... iii

Acknowledgements ... iv

List of figures ... x

List of tables ... xv

Chapter 1 INTRODUCTION

1.1 Motivation and history of the III-nitrides ... 1

1.2 InN bandgap ... 2

1.3 The resurgence of interest in InN ... 3

1.4 Thesis outline ... 4

Chapter 2 Literature Review

2.1 Revisiting physical signatures of GaN ... 6

2.2 Surface accumulation layer ... 8

2.3 Evidence of buried p-type layers in Mg-doped InN ... 10

2.4 Growth problem ... 12

2.5 Photoluminescence of n-InN ... 13

2.6 Current state of art of p-InN ... 14

Chapter 3 Photoluminescence Spectroscopy of InN

3.1 Luminescence and band structure of InN ... 17

3.2 Excitons ... 18

3.3 Free-to-bound and donor-acceptor pair 21

3.4 Auger recombination 22

3.5 Moss-Burstein effect and InN bandgap 23

3.6 Temperature dependent Arrhenius decay..26

3.7 Bose-Einstein and Pässler..28

3.8 Excitation intensity dependent PL 30

3.9 Experimental consideration 33

Chapter 4 Nitrogen-rich Magnesium doped Indium Nitride

4.1 The growth parameters and electrical properties 37

4.2 Optical properties of N-rich InN:Mg/YSZ(111) 41

4.3 Mg forming a deep acceptor..48

4.4 Donor-acceptor pair transition 53

4.5 Brief summary...56

Chapter 5 Indium-rich Magnesium doped Indium Nitride

5.1 The growth parameters and electrical properties 59

5.2 Optical properties of InN:Mg/GaN 66

5.3 Band-to-band transition 71

5.4 Excitonic transition 76

5.5 Brief summary...81

Chapter 6 Potential acceptor dopants

6.1 Zinc doped InN 84

6.1.1 The growth parameters and electrical properties...85

6.1.2 Optical properties of InN:Zn/GaN 87

6.1.3 Brief summary of Zn-doped InN 96

6.2 Manganese doped InN 97

6.2.1 The growth parameters and electrical properties 98

6.2.2 Optical properties of InN:Mn/GaN 101

6.2.3 Brief summary of Mn-doped InN 106

Chapter 7 Conclusion and Future research

7.1 Key results of Mg-doped InN 108

7.2 Key results of Zn-doped InN 111

7.3 Key results of Mn-doped InN 112

Appendix

A. Molecular beam epitaxy growth and characterization techniques 114

B. Film thickness effect 116

C. Ion bombardment and annealing effect of Mg-doped InN 118

Reference

Reference 120

List of Figures

1.1 InN publications per year and reported optical bandgap 3

1.2 The In_xGa_{1-x} bandgap and the standard solar spectrum. 4

2.1 The schematics of (i) substitution, (ii) interstitial, and (iii) complex, doping arrangements. 7

2.2 The schematic of bandgap alignments of alloys with two different bandgaps. 8

2.3 The average formation of neutral hydrogen level. 9

2.4 The alternative formation of conduction band minimum and the Fermi energy level correspond to In_xGa_{1-x} alloy composition...10

2.5 Reported PL intensities of InN:Mg as a function of Mg concentration..............15

3.1 A simplified band structure of InN. 18

3.2 The bonding diagram of InN with an extra electron and the schematic of exciton...20

3.3 The schematics of the Auger recombination mechanisms. 23

3.4 Reported PL and absorption bandgap data as a function of carrier concentration for InN...24

3.5 The calculated Fermi energy level corresponds to the background electron concentration. 25

3.6 The schematics of thermal Arrhenius decay and the activation energy for (a) a neutral donor bound state and (b) a neutral acceptor bound state. 26

3.7 The plot of activation energies of neutral bound states. 27

3.8 The summary of described recombination processes in schematic.....................31

3.9 A schematic diagram of the experimental setup used for photoluminescence 34

3.10 The blackbody radiation curve for InSb and InGaAs detectors. 35

4.1 SIMS Mg concentration of a N-rich InN:Mg/YSZ series as a function of Mg deposition source temperature....................38

4.2 SFH electrical properties of a N-rich InN:Mg series as a function of Mg concentration....................39

4.3 SEM images from the InN:Mg/YSZ(111) films....................40

4.4 4 K PL spectra of N-rich InN:Mg....................42

4.5 PL peak positions of InN:Mg/YSZ as a function of carrier concentration..........43

4.6 FWHM of N-rich InN:Mg/YSZ as a function of Mg concentration....................44

4.7 The energies of a free-to-bound and DAP transition in various polarity of InN:Mg/YSZ as a function of Mg concentration....................45

4.8 Variation of the PL intensity of N-rich InN:Mg/YSZ with different Mg content.46

4.9 The decay of the photogenerated carrier density according to TRDT................47

4.10 PL spectra of sample 590-InN:Mg/YSZ as a function of temperature................49

4.11 The Arrhenius plot of the absolute peak intensities for I_{fb} and I_{mh} (sample 590-InN/YSZ) 50

4.12 A low temperature PL and room temperature photo-reflectivity spectra (sample 590-InN:Mg/YSZ)....................51

4.13 The PL spectra of sample 590-InN:Mg/YSZ as a function of excitation power. Inset) the log slope of two different components by using a power law equation52

4.14 PL spectra of sample 555-InN:Mg/YSZ as a function of temperature................54

4.15 The Arrhenius plots of the absolute peak intensities for I_{DAP}. Inset) the Pässler and Bose-Einstein plots of the variation of I_{DAP} emission centres as a function of temperature....................55

4.16 The PL spectra of sample 555-InN:Mg/YSZ as a function of excitation power. Inset) the log slope of main component by using power law equation...............56

4.17 The optical properties from a series of InN:Mg/YSZ films from temperature and power dependent PL analyses as a function of Mg concentration................57

5.1 FWHM (PL) of trial growth InN/GaN films....................60

5.2 SEM images of InN:Mg/GaN thin films..60

5.3 SIMS Mg concentration of a InN:Mg/GaN series as a function of Mg deposition source temperature..61

5.4 SFH electrical properties of a N- and In-rich InN:Mg/GaN series as a function of Mg concentration..62

5.5 Valence band edge XPS data for InN:Mg/GaN films with respect to the surface Fermi level as a function of Mg content..64

5.6 Concentration of electron and hole carriers as extracted by VFH measurements as a function of Mg cell temperature. Inset) the QMSA spectrum of an In-rich InN:Mg/GaN film grown with a Mg cell temperature of 280 °C........................65

5.7 4 K PL spectra of N- and In-rich InN:Mg/GaN. 67

5.8 PL peak positions of InN:Mg/GaN as a function of carrier concentration. 69

5.9 Summary of the relative quantum efficiency of InN:Mg thin films in this study as a function of the SIMS Mg concentration 70

5.10 Extracted FWHM of PL spectra corresponds to Mg cell temperature 72

5.11 Excitation power dependent PL for the In-rich 714-InN:Mg/GaN film grown with a Mg cell temperature of 280 °C. Inset) the least square fit of power law corresponding to the determined components..73

5.12 Temperature dependent PL for the In-rich 714-InN:Mg/GaN film grown with a Mg cell temperature of 280 °C. 74

5.13 The Arrhenius plots of the absolute peak intensities for I_{fb}. Inset) the Pässler and Bose-Einstein plots of the variation of I_{bb} emission centres as a function of temperature. (In-rich 714-InN:Mg/GaN)..75

5.14 4 K PL spectra of sample In-rich 714-InN:Mg/GaN as a function of excitation wavelength. 76

5.15 Excitation power dependent PL for the In-rich 713-InN:Mg/GaN film grown with a Mg cell temperature of 267 °C. Inset) the log slope of main component by using power law equation 77

5.16 Temperature dependent PL for the In-rich 713-InN:Mg/GaN film grown with a Mg cell temperature of 267 °C..78

5.17 The Arrhenius plots of the absolute peak intensities for A°X. Inset) the Pässler and Bose-Einstein plots of the variation of A°X emission centres as a function

of temperature. (In-rich 713-InN:Mg/GaN) 79

5.18 The Bose-Einstein plots of the PL line-width (FWHM) for A°X (In-rich 713-InN:Mg/GaN) 80

5.19 The fitted experimental data of In-rich 713-InN:Mg/GaN and the fit to the power law as a function of laser power for several representative temperatures. 81

5.20 The compressive details of optical properties for In-rich InN:Mg/GaN as a function of Mg cell temperature. 82

6.1 SEM images of N- and In-rich InN:Zn/GaN films. 85

6.2 SFH electrical properties of an InN:Zn/GaN series as a function of Zn cell temperature 86

6.3 4 K PL of N- and In-rich InN:Zn/GaN.. 88

6.4 Variation of the PL intensity of InN:Zn/GaN with different Zn content. Inset) the photogenerated carrier density according to TRDT 89

6.5 Excitation power dependent PL the In-rich 655-InN:Zn/GaN film grown with a Zn cell temperature of 248°C. 90

6.6 The fit of power law corresponds to determined components from the In-rich 655-InN:Zn/GaN sample. 91

6.7 Temperature dependent PL of the In-rich 655-InN:Zn/GaN film grown with a Zn cell temperature of 248 °C. 92

6.8 The Arrhenius plots of the absolute peak intensities for $I_{DAP,}$ $I_{sa,}$ and I_{mh} (In-rich 655-InN:Zn/GaN). 93

6.9 The absolute PL intensity of DAP, free-to-shallow, and Mahan exciton transitions as a function of Zn cell temperature. 94

6.10 4 K PL spectra of In-rich InN:Zn/GaN. 95

6.11 Extracted Curie temperatures for a wide range of III-V semiconductors............98

6.12 SIMS Mn concentration of an InN:Mn/GaN series as a function of Mn deposition source temperature. Inset) SEM images of the In- and N-rich InN:Mn/GaN films 99

6.13 SFH electrical properties of a N- and In-rich InN:Mn/GaN series as a function of Mn cell temperature...100

6.14 A) QMSA spectrum of InN:Mn/GaN film grown with a Mn cell temperature of 563 °C under N-rich condition. B) Valence band edge XPS data for N-rich InN:Mn/GaN films with respect to the surface Fermi level as a function of Mn concentration 101

6.15 4 K PL spectra of N- and In-rich InN:Mn/GaN. 102

6.16 Power dependent PL of the N-rich 724-InN:Mn/GaN film grown with a Mn cell temperature of 563 °C. Inset) the log slope of three different components by using a power law equation. 103

6.17 Temperature dependent PL of N-rich 724-InN:Mn/GaN with a Mn cell temperature of 563 °C. Inset) The Arrhenius plot of the absolute peak intensities for I_{DAP} and I_{fb}. 105

6.18 The PL and PC signals from N-rich 724-InN:Mn/GaN at 4K and 20K, respectively. 106

A. A simple schematic diagram of the nitride MBE system. 115

B. PL spectra of InN/YSZ with a wide range of film thicknesses 117

C. PL spectra of GS1810 as grown, irradiated fluence of 2×10^{15} cm^{-2}, and various annealing temperatures. 119

List of Tables

3.1 Bose-Einstein and Pässler parameters of InN. 29

4.1 A summary of growth conditions and Hall effect measurements of Mg doped InN/YSZ films. 40

4.2 The polarity inversions and PL energy shifts (InN:Mg/YSZ) 43

4.3 The list of transition detail and extracted PL parameters (InN:Mg/YSZ)...............58

5.1 A summary of growth conditions and Hall effect measurements (SFH) of Mg doped InN/GaN...66

5.2 The list of transition detail and extracted PL parameters (In-rich InN:Mg/GaN) ...83

6.1 A summary of growth conditions and Hall effect measurements of Zn-doped InN/GaN films 87

6.2 A summary of growth conditions and Hall effect measurements of Mn doped InN/GaN films 101

B.1A summary of growth condition (thickness) and Hall effect measurements of InN/YSZ films. 116

Chapter 1

Introduction

"It's as if nature designed this material on purpose to match the solar spectrum."

Wladek Walukiewicz

An epoch-making discovery of light emitting devices has modified the face of the world and yet a great deal of potential for the future of these goods is ongoing. The rigorous search for novel materials continues and naturally seeks potential lighting devices that can be more efficient. Perhaps the key to this endeavor is the somewhat overlooked semiconductor, indium nitride (InN). This thesis reports some understanding of the optical property of p-InN, which is of interest in the future optoelectronics.

1.1 Motivation and history of the III-nitrides; Keying into the next generation

As a part of the evolution of our daily lives, semiconductor applications have advanced by leaps and bounds. Till date, the most common type of electronic application is silicon-based (Si) as the material being abundant and inexpensive[1]. Si also takes the initiative in research perspective which provides the fruitful fundamental roadmap for other new semiconductors. Despite all of this, Si has a few weaknesses including its indirect bandgap and an insufficient light conversion, which restrict the use in advanced opto-electronics application. Thus, this situation has naturally prompted new research routes towards more efficient semiconductors in solar cells, III-nitrides[2-4,8,15]. (Al,Ga,In)N is expected to be the next generation of semiconductors which can satisfy many desired requirements for both photovoltaic

applications and LEDs. Chief among them GaN has received considerable attention as a candidate. The optical properties of GaN are well known as this semiconductor forms the basis of "blue" LEDs through its bandgap of 3.4 eV[5-7]. In the 1990s, Nakamura *et al.*[9-13] first reported high-brightness Ga-rich $In_xGa_{1-x}N$ light emitting diodes (LEDs). After this breakthrough, the III-nitride lighting sector has found commercial success (*ie*. street lighting and displays) and GaN has become the most important semiconductor since Si. InN is also active affiliation with $In_xGa_{1-x}N$ LEDs but much less effort has been devoted to InN or In-rich $In_xGa_{1-x}N$.

The optical bandgap value of InN is traced to the early 1980s. The first distinctive optical absorption edge at about 1.9 eV was determined by Tansley and Foley[18] and this value was specified as an official bandgap[19-21,39]. Early prognosis for InN as the red binary point of $In_xGa_{1-x}N$ devices was rather unenthusiastic and has been complicated by many hurdles. The major challenge of InN is an inherent difficulty in growing a device standard quality due to 1) the low decomposition temperature of In, and 2) a high spatial impurity concentration (*ie*. an oxygen contamination). These persistent issues led to a lack of fundamental knowledge about InN and have remained drawbacks to device fabrication.

1.2 InN bandgap; A subject prolific with controversy

An unexpected discovery makes something out of nothing. The recent III-nitride growth by advanced techniques such as molecular beam epitaxy (MBE) has introduced 'a new era of InN'. After a long silence in the literature, Davydov *et al.*[14] triggered the research interests of InN in 2001. A plasma-assisted MBE grown InN thin film exhibited a strong absorption peaking below 1 eV. This observation suggested that the initial bandgap of 1.9 eV for InN was incorrect. Re-evaluation of InN was conducted and progressively lower optical band gaps in the range of 0.65 - 0.80 eV were confirmed[22,24-25]. Other crucial parameters were naturally re-written. MBE grown InN epilayers with much reduced background electron concentrations were produced. Moreover, the small electron effective mass in a range of 0.04 - 0.14 m_o (m_o is the free electron mass)[35] with a high electron mobility of 3200 cm^2/Vs identified InN as a promising candidate for high electron mobility transistors (HEMTs)[17]. The publication rate concerning the material increased dramatically as depicted in figure 1.1.

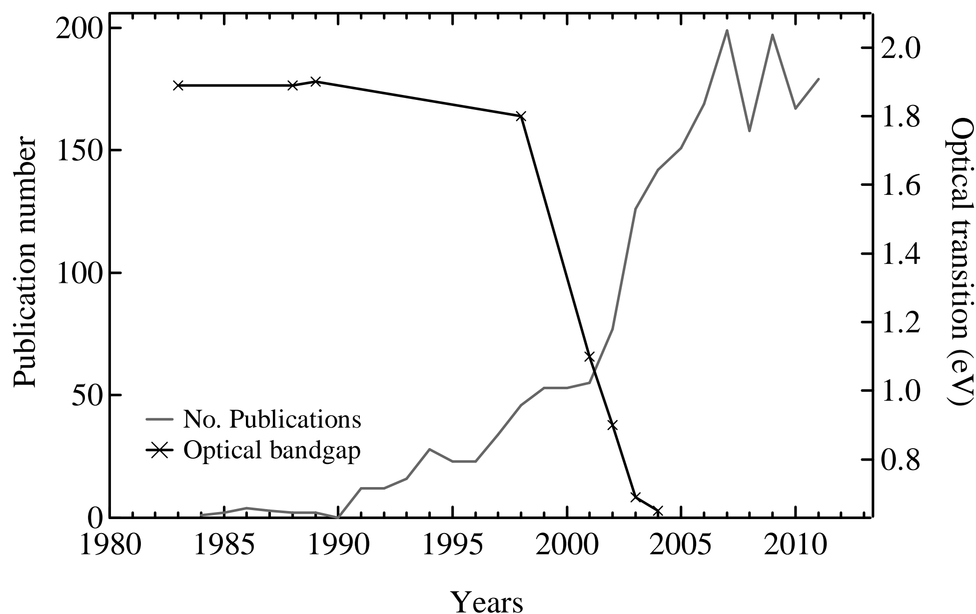

Figure 1.1 InN publications per year [based on the 'Web of Science'] and reported optical bandgaps[14,18-28].

An agreement of the infrared bandgap value of InN has emerged[22,30-33] and the present best estimate reports 0.67 eV[24]. Many literatures highlighted the consequence of a higher energy absorption onset in previous reports. The chief reason is an oxygen induced background electron concentration that results in occupied states well above the conduction band minimum (CBM). This phenomenon is called the Moss-Burstein effect[29] and absorption transitions to empty conduction band states occur at energies higher than the bandgap value. Theoretical simulation has predicted that the Moss-Burstein occupation can extend the absorption energy as much as 2 eV for InN[32]. Anyhow, the fact that the new value being located in the infrared region was more than enough to fascinate the semiconductor industry.

1.3 The resurgence of interest in InN

The potential spectral range of III-nitrides now fully covers the solar spectrum with the new establishment of the infrared bandgap nature of InN. This means that a new high-efficiency solar cell can be tuned across the UV to IR regions via the full visible solar spectrum, using only a single system of $In_xGa_{1-x}N$ alloys as shown in figure 1.2. This prospect not only enhanced the potential performance of future optoelectronics[34] but also offered a wide range of available applications including terahertz emitters and high-speed transistors[17].

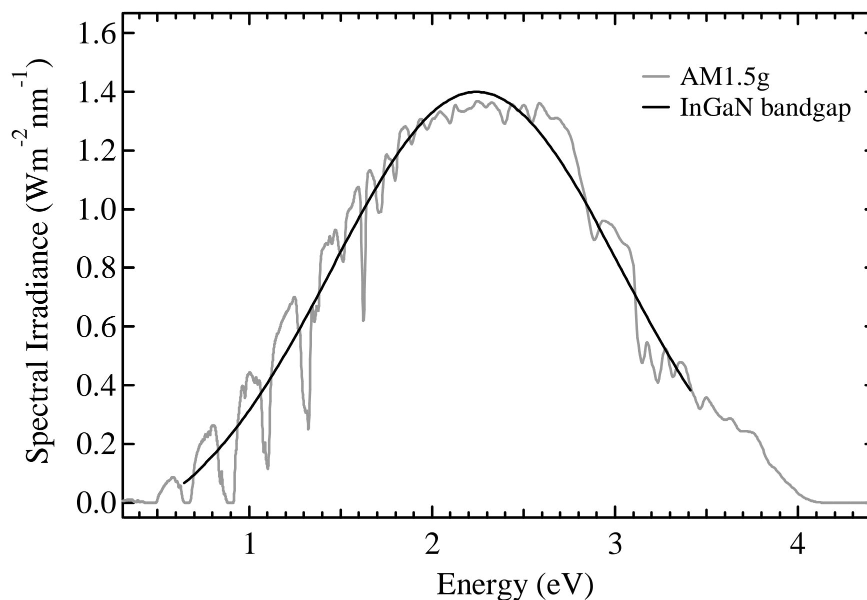

Figure 1.2 The $In_xGa_{1-x}N$ bandgap and the standard solar spectrum (AM1.5g)[34].

The reality of the current situation however, is rather compromised as many basic properties of the material remain vague. Not only is the fundamental bandgap of InN yet to be directly seen but to get In-rich $In_xGa_{1-x}N$ based devices commercialized, the realization of p-InN is a weighty issue to be solved. Despite this, less attention has been paid on the central properties of p-InN. Although a large number of InN studies now show the better control of defect frequency, the morphology of p-InN is yet at a pioneer stage. The purpose of this thesis is to discuss the current state of the art of p-InN, and provide a fruitful path to understand the central properties of the material.

1.4. Thesis outline ; A promise to keep and place to go

The somewhat unique characteristics of InN contribute to the current poor understanding of p-type InN. Nevertheless, the foregoing discussions postulate InN as the 'key' to the next generation of semiconductor electronics and the maturity of InN is expected to be hard won in the foreseeable future. This thesis presents an investigation of InN with trace amount of dopants. A significant component will be the photoluminescence (PL) study relevant to the current problems that p-InN is facing and proposes an explanation that will move toward developing device applications.

The past physical signature of both InN and GaN is reviewed Chapter Two. This delivers an insight into current central properties and challenges of InN. In Chapter Three, the band structure of InN is introduced followed by discussions of luminescence properties. This also links to the description of the experiment and the interrelated theories of the PL spectroscopy. The fourth and fifth chapters are the optimizations of Mg-doped InN series. The growth morphology of InN:Mg is mentioned and then discussions of comprehensive PL studies follow. Time-resolve differential transmission (TRDT), variable magnetic field Hall effect (VFH), secondary ion-mass spectroscopy (SIMS) and scanning electron microscope (SEM) have contributed to the interpretation. This thesis considers all of these practices in parallel to PL. The sixth chapter involves the investigation of p-InN with a number of potential acceptor candidates including Zn and Mn. There is interest in determining whether alternative acceptors might give a device quality p-type InN. In the final chapter, the conclusion is drawn based on a wealth of gathered information throughout the research.

Chapter 2

Literature Review

The noteworthy establishment of a near infra-red bandgap for InN provided a significant motivation for the next generation of nitride based research. In the past decade, a rigorous effort has been devoted to grow high quality InN thin films. Moreover, recent research interests have now been shifted from understanding fundamental properties of intrinsic InN to focusing on the realization of p-type InN using Mg, given its success with GaN[69]. However, a limited number of studies have been conducted to understand the basis of p-type InN. In this chapter, the past physical signatures of (In,Ga)N are revisited and furthermore provides an insight into a current central property of InN. Results regarding challenges in InN:Mg are also comprehensively discussed.

2.1 Revisiting physical signatures of GaN; How's and why's of Mg doping

Doping is the appealing technique that makes semiconductors part of meaningful technology, which not only enables the modification of both the electrical and optical properties of semiconductors but also it is immensely important in terms of applications (*ie*. a pn junction base). This issue cuts across the critical realization of p-type InN and the first question naturally followed of 'what material should be chosen as a suitable dopant and how?'

According to the periodic table, the cations are a group III element (nitrogen is a group V) for the (In,Ga,Al)N. The potential acceptor candidates therefore belong to the group II elements and can substitute for In, Ga, and Al. Of the candidate acceptors, Mg is expected to be the

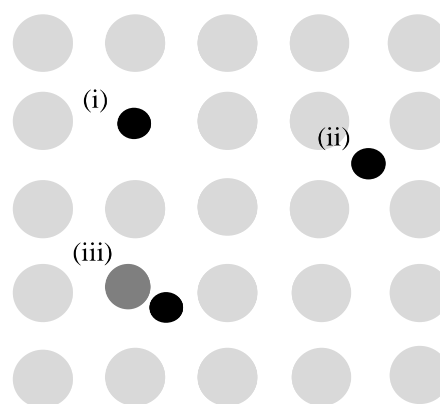

Figure 2.1 The schematics of (i) substitution, (ii) interstitial, and (iii) complex doping arrangements. The dark and grey circles represent impurities and lattices, respectively.

most suitable candidate for p-type and incorporation with GaN gives the small binding energy of 120 meV (note: Zn is 340 meV)[69,248]. It is well known that an acceptor with a smaller binding energy is a very useful as it allows a higher free hole concentration (a wider p-type window) and returns a less resistivity[248,249]. The ‘choice’ and ‘adequacy’ of dopants for a given material is generally dictated by three arrangement types of incorporation into the atomic lattice, which are schematically drawn in figure 2.1. These alternatives certainly have showed different doping aspects in GaN:Mg[131,133,230-236]. Through trial and error, the doping morphology of GaN:Mg had paved the way for InN to follow.

Substitution has the impurity atom taking over the host lattice site such as In, Ga, and Al. In such an arrangement, the Mg formed an acceptor state deep inside the bandgap and the observation of p-type conductivity was feasible for GaN [69,249]. Interstitial means the impurity is situated in between the host lattices sites. The electrical signatures of GaN:Mg have reported an interstitial gallium (Ga_i) acting as either a shallow or deep donor[128,231-233]. Hence this occupation increases the background electron concentration. Complexes are formed when multiple defects are introduced and connected in some fashion by the host lattice. Such organization induces the Mg to pair with residual impurities such as hydrogen (Mg-H). Hydrogen often acts as a shallow donor in III-nitrides (exclusively as a donor for InN) and the reported activation energy (*ie* a shallow donor’s binding energy) for Mg-H is in a range of 4 - 12 meV for (In,Ga)N[133,230,235,236].

It was likely to first consider Mg as the most suitable acceptor dopant for InN. In 1999, Blant *et al.*[131] determined the incorporation of Mg on the crystal lattice. An extended x-ray absorption fine structure spectroscopy (EXAFS) study proved that Mg can be incorporated on the In sites (Mg_{In}) and this discovery initially suggested Mg as an adequate acceptor dopant for InN. Mamutin *et al.*[159] examined heavily doped InN:Mg films with a Mg concentration range of 10^{19} - 3×10^{20} cm^{-3}, although it was later discovered that such a concentration range

was rather overwhelming and somewhat degraded the crystal quality. Commonly observed was that the standard Hall effect measurement thwarted a measure of p-type conductivity. A few years later, the presence of a surface electron accumulation layer postulated InN as a 'complicated material' [31,62-67].

2.2 Surface accumulation layer

The evidence of a surface electron accumulation layer in InN was first noticed in a 2000 synchrotron radiation photoemission spectroscopy (SRPES) study by Schaff *et al.*[62]. This study recognized a somewhat high value of electron density approximately 10^{20} cm^{-3} at the surface of metal/InN interfaces and was attributed to an electron accumulation. A 2004 specular high-resolution electron-energy-loss spectroscopy (HREEL) study by Mahboob *et al.*[67] confirmed that such an intrinsic surface layer is still present at 'as grown' InN thin film surfaces. This literature also highlighted the importance of the charge neutrality level (CNL), which is the key aspect for the surface states nature and the role of native point defects[71]. The CNL has alternative names of the branch point energy (E_B) and the Fermi stabilization energy (E_{FS}) and is discussed in the following paragraphs.

The concept of the CNL is the average energy of native point defects, examples of which are In_{int} and N_{vac} for InN. A 1984 study by Tersoff[256] discussed the potential 'midgap' state, which is originated from a hetero-structured band discontinuity. This band offset is attributed to a bandgap misfit of an alloyed semiconductor. A threading dislocation from a metallic interface or a lattice mismatch between the substrate and a single semiconductor also can be a primary cause. Wavefunctions from the band states extend into the nearby 'empty space' and produce the midgap states[256]. This mechanism is drawn schematically in figure 2.2. The midgap state is positively (negatively) charged if such an electronic level is close to the conduction band (the valence band) and the CNL points to the equilibrium formation.

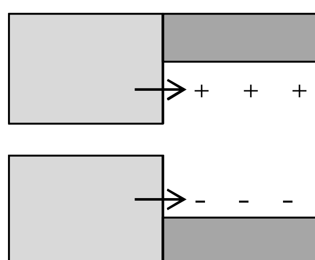

Figure 2.2 The schematic of electronic energy band alignments of semiconductor. The shaded boxes indicate occupied gaps. The arrows represent the wavefunctions and the charged states are located nearby the conduction (top) and valence (bottom) bands[256].

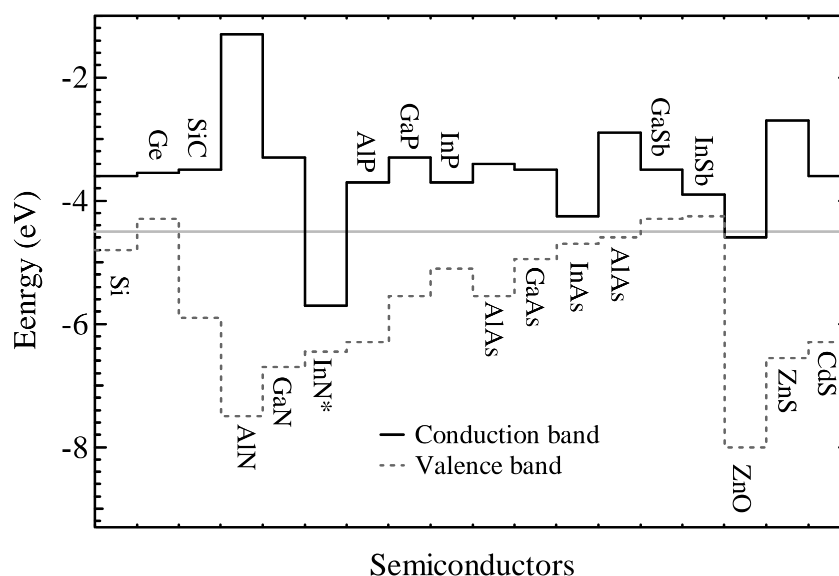

Figure 2.3 The average formation of neutral hydrogen level (the horizontal grey line). The solid and dotted lines represent the positions of the conduction band minimum, and valence band maximum, respectively for selected semiconductors[254].

It is very difficult to accurately verify the CNL by using a simple model. In fact, the CNL by its own is not sufficient to determine the surface state (charged) type and must be compared to its relative position to the Fermi level (E_F). If the E_F is located below (above) the CNL, the native point defects are donors (acceptors). A good example of this tendency is the neutral formation of hydrogen (H°). This is the crossover point for hydrogen whether it acts as a donor, H^+ (E_F < H°) or an acceptor, H^- (E_F > H°) as a function of the E_F[254]. A simple theoretical approach can pinpoint the neutral formation of hydrogen and its average value (from a wide range of semiconductors) is well specified as presented in figure 2.3[254].

Similar to the neutral formation of hydrogen in the figure above, the CNL of InN is located deep inside the conduction band. The intrinsic (or typical) E_F position of InN should be below this CNL and the native defects are therefore exclusively donors[68]. As has been reported, the surface state of InN is located above the E_F[67,68]. This circumstance makes the surface state donors positively charged (unoccupied)[67] and the E_F pins to the conduction band minimum (CBM) at the Γ-point. Also discussed was that the donors at surface states must be ionized (to be positively charged), forming an electron accumulation layer[31,62-67,71]. Such a surface layer makes contacting a p-type layer problematic as standard electrical measurements such as Hall become strongly influenced by the high density electrons.

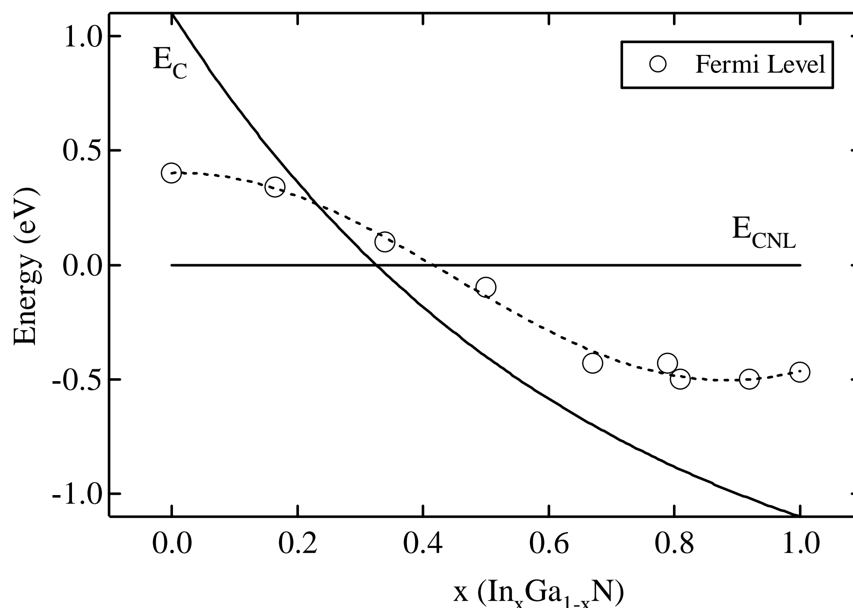

Figure 2.4 The alternative formation of conduction band minimum (E_C) and the Fermi energy level (empty circle) correspond to $In_xGa_{1-x}N$ alloy composition[73]. The CNL is also drawn (the horizontal solid line).

Interestingly, a $In_xGa_{1-x}N$ ternary system contains two discernible surface morphologies[72-74]. GaN has the opposite tendency to InN of having a slight depletion layer at the surface. As displayed in figure 2.4, both the E_F and CNL of GaN sit within the bandgap. The E_F is located above the CNL (an acceptor native defect) in the Ga-rich zone, therefore a careful control of compositions or background electron concentration enables both n- and p-type conductivity[69]. Complexity arises at In_x=0.46 onwards, where the CNL is located above the conduction band minima (CBM), configuring an accumulation layer as discussed in the previous paragraph. Under this circumstance, a p-type surface layer, which is the key requirement for applications, is somewhat suppressed. As a consequence, there are as yet no reports of direct electrical contact to a p-type layer on the surface of InN layer. However, an embedded p-type layer has been indirectly examined either by electrochemical capacitance-voltage (CV)[60] or variable magnetic field Hall effect (VFH)[61].

2.3 Evidence of buried p-type layers in Mg-doped InN

The first discovery of an embedded p-type layer was reported by Anderson *et al.*[61], in 2006. A series of PAMBE grown Mg-doped epilayers were examined by using a combination of various characterizations. VFH studies revealed distinctive evidence of buried p-type states

beneath a surface electron accumulation layer and correspondingly, a prominent Mg-related luminescence feature was clearly resolved at 0.56 eV with the activation energy of 110 meV. The Mg activation energy in InN:Mg is expected to be smaller than those from GaN:Mg since the binding strength of Mg as a deep acceptor in III-nitrides is proportional to the effective hole mass and the bandgap[250]; more details are given in section 3.6. Jones *et al.*[132] also examined a quantitative bulk property in Mg doped InN by using electrochemical capacitance-voltage (ECV) and successfully observed the embedded hole layers below the accumulated surface region. PL has not been a critical part of initial the experiments in Mg-doping as emission from such film was heavily quenched (*ie.* either a weak PL emission or none).

The evidence of a buried p-type layer encouraged more InN:Mg research. Wang *et al.*[134,135] published two papers in the following year and have actively participated in the development of p-InN. A systematic analysis by transmission electron microscopy (TEM) determined that initial N-polar thin films flipped to In-polar as the Mg content reached the critical value of 10^{19} cm^{-3}, where the accumulated Mg defects was recognized on the InN surface[134]. Meanwhile, it was also discovered that the Mg sticking coefficient had no dramatic change upon the polarity type[135]. The observation is in sharp contrast to a surface polarity dependent study of Mg doped GaN[174]. Ga-polar GaN thin films yielded relatively higher Mg sticking coefficients than those from N-polar faces, indicating more plentiful Mg incorporation.

The interrelationship between electrical and optical results of InN:Mg was also analyzed. In a 2007 study by Wang *et al.*[133], PL decreased markedly with increasing Mg content and was observed only from samples with a low Mg cell temperature range of 150 to 175 °C. At the highest Mg cell temperature of 320 °C, a restoration of PL intensity was noted but was rather structureless. This PL restoration was attributed to the complexes introduced by overdoping. PL measurements (taken from a low range of Mg cell temperature) revealed a number of midgap energy peaks near 0.61 eV and similar to what has been observed elsewhere[61], the features were likely correlated to a deep Mg acceptor with an activation energy of 61 meV[133]. Meanwhile, the electrical properties of InN:Mg samples taken from single magnetic field Hall effect measurements (SFH) exhibited a general n-type trend of decreasing mobility but increasing electron carrier concentration as a function of Mg content[133].

Khan *et al.*[92] examined an usual characteristic of PL from Metal-Organic Chemical Vapour Deposition (MOCVD) grown InN:Mg in the same year. The PL emission line was at a relatively high energy position of approximately 0.76 eV for the sample grown using Mg flow rate of 15ml/min (corresponds to the Mg concentration approximately 1.8×10^{20} cm^{-3}). A typical Arrhenius decay behaviour was seen from a temperature dependent PL study and the activation energy yielded 54 meV for a Mg related emission, being in close agreement with the range of activation energies reported by Anderson *et al.*[61] and Wang *et al.*[133]. It is worth noting that this PL of samples taken from MOCVD grown InN:Mg exhibited the high energy features as much as 0.82 eV. This may be attributed to the tendency of InN to pair with hydrogen during the growth and its exclusive donor nature[254] contributes to the onset of the Moss-Burstein effect in InN[29,238]; more details are given in section 3.5. In fact, the common carrier gas in MOCVD is hydrogen (and NH_3)[122]. This issue is one of the key challenges for InN growth and is the subject of the next section.

2.4 Growth problem; Searching for a perfect fit

The low dissociation temperature of InN is problematic and somewhat limits the use of various growth techniques. Owing to a weak In-N bond, the growth temperature of InN is limited to 600 °C[123,124,129,130,137]. Thereby, it faces difficulties in MOCVD growth since such a restriction weakens the strength to decompose the residual impurities such as hydrogen and oxygen. For instance, the p-type doping using Mg can be established by an annealing process in the case of the complex doping arrangement (Mg-H) in GaN:Mg, whereas this is rather problematic for InN[129,130]. Perhaps, the best solution is offered by the ultra high vacuum (UHV) Plasma-Assisted Molecular Beam Epitaxy (PAMBE) growth technique, which can significantly prevent this event and makes any post growth annealing process unnecessary. Therefore it has always been the first choice for the growth of (In,Ga)N:Mg, among arrays of growth mechanisms such as MOCVD and Pulsed Laser Deposition (PLD)[137].

Another growth problem is the lack of lattice matched substrates. A high spatial defect frequency caused by a mismatch make it difficult to achieve device quality material[125]. The mismatches to common substrates of sapphire (Al_2O_3)[23] and Si[126] are 26% and 8%, respectively. Alternatively, Anderson *et al.*[127] obtained encouraging carrier concentration and

Hall mobility values of 2×10^{18} cm^{-3} and of 200 cm^2/Vs, respectively using a Yttria-stabilized zirconia (YSZ) substrate, where the mismatch is only 2% with InN. The findings are much better InN films with Al_2O_3 and Si substrates[126], although they were still inferior to that of the sample deposited on a GaN template.

To date, the best InN (or InN:Mg) films grown use GaN buffer layers on top of sapphire substrates[145,146]. Direct growth on GaN/Al_2O_3 allows the film thickness more than 1μm, which can minimize the threading dislocation[155]. Another benefit is that a GaN buffer can be grown at low temperatures, which can 'relax' the atomic space and significantly reduce the lattice mismatch to 10%[23]. This growth progress has enabled more detailed studies that provide a better understanding of intentionally or unintentionally doped InN.

2.5 Photoluminescence of n-InN

Investigations of PL in undoped InN also have provided a fruitful path for development of InN:Mg. A 2004 study by Arnaudov *et al.*[91] showed that a presence of an acceptor state in n-InN can be intrinsically introduced. In InN with high background electron concentration, potential acceptor states are formed by the "potential fluctuation" [222-224]; more details are given in section 3.3. This report considered two different potential acceptor states: 1) decreasing density of states in the tail of the valence band (the so called Urbach tails)[151] treated as the shallow acceptor centres and 2) the randomly distributed impurities dispersed inside the bandgap and acted as the residual deep acceptors. The activation energies of the given states yielded 18 and 85 meV. The former and latter values are calculated by using the hydrogenic acceptor and the free-electron recombination models, respectively. In a 2005 detailed PL study in undoped InN by Klochikhin *et al.*[90], again two observed PL peaks at 0.67 and 0.6 eV were characterized by the activation energies of 5 and 50 meV, respectively. The higher energy peak was attributed to a recombination of degenerate electrons to the Urbach tail induced shallow acceptor states, while the lower energy peak was related to a residual deep acceptor.

In a 2008 study by Yao *et al.*[117], the effect on PL of the In/N ratio was determined. The spectral assessment examined important PL aspects of the line shape broadening and relative

energy position. As the N flux increased, the PL emission broadened considerably and blueshifted by 30 meV, indicating 'degenerate InN' (more details are given in section 3.5) with a high defect frequency. Correspondingly, an approximately order of magnitude higher SFH n-type carrier concentration was extracted from N-rich samples.

In the same year, Feneberg *et al.*[100] reported a detailed study of PL in unintentionally doped InN. The distinctive appearance of multiple PL features indicated plentiful radiative pathways. Four overlapping PL components were observed over a wide range of spectra between 0.6 and 0.72 eV. The line-shape analysis as a function of temperature qualitatively assigned two different residual hole localized states (a deep and shallow) which contributed to the total PL. Somewhat interestingly, the 'S-shaped' temperature induced shifts were stated as evidence for both acceptor states. As the name suggests, temperature dependence of PL peak centres show a combination of blue- and red-shifts (S-shape) and this phenomenon had already observed in $(In,Al)_1Ga_{1-x}N$[240,241]. The 'S-shaped' temperature induced shift can be interpreted as the thermal escape of carriers being transferred to different localized states above the CBM (likely case for InN with a strong onset of the Moss-Burstein effect), the so called resonant localized donor state (RDS)[40]. The highest feature near 0.72 eV introduced a concept of the Mahan exciton, which is the recombination between electrons from Fermi sea level (an electron energy state) and the localized holes in the acceptor states within a large spread in momentum k space[118]; more details of this are given in section 4.3. This interpretation was convincingly supported by the reflectivity measurement, where the spectra directly pointed to the Fermi edge and was in the vicinity of a Mahan feature.

2.6 Current state of art of p-InN; a new challenge beckons

It is worth noting that residual deep acceptor states from unintentionally doped InN[90,91,100] differ significantly to Mg-doped InN[61,92,133], where a Mg-related deep acceptor produces a prominent p-type layer as evidenced from the variable magnetic Hall effect (VFH) or electrochemical capacitance-voltage (ECV) measurements. For this to be feasible an appropriate Mg concentration range needed to be adequately addressed which can efficiently compensate the background electron concentration. Miller *et al.*[75] thereby reviewed the effect of Mg incorporation in InN in 2010. Mg concentrations in a "window" from 3×10^{17} to 1×10^{19}

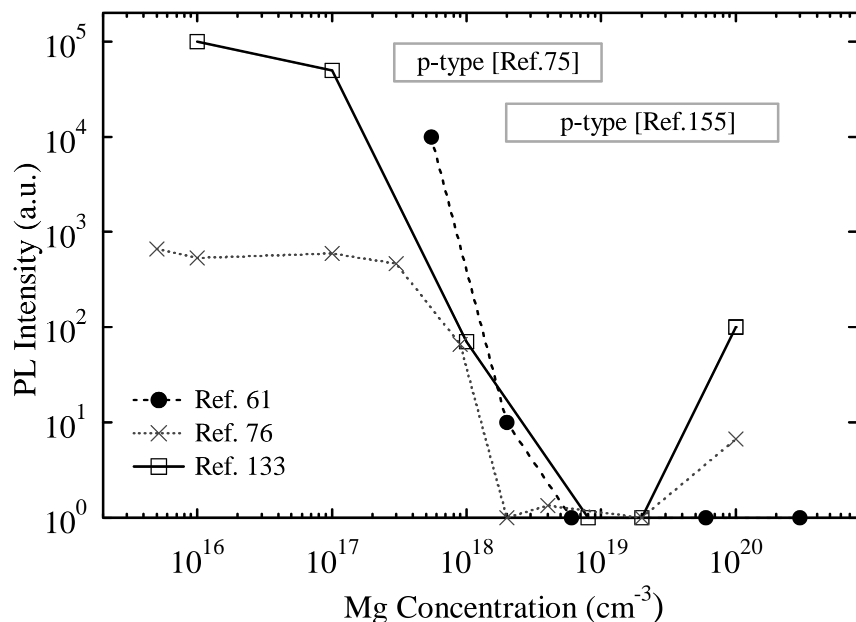

Figure 2.5 Reported PL intensities of InN:Mg as a function of Mg concentration. No indication of luminescence line at the potential p-type region[61,76,133]. The grey boxes represent the potential "p-type window" [75,155].

cm^{-3} produced hole-conducting, p-type films as shown by a positive Seebeck coefficient (p-type) as extracted from the thermopower measurements. However, outside from this critical range, Mg doping led to a negative Seebeck coefficient (n-type).

This result has a discernible difference to an ECV profiling report by Yoshikawa *et al.*[155], where the "p-type window" was within a Mg concentration range of 2.2×10^{18} to 2.4×10^{20} cm^{-3}. Similar to what is reported by Miller *et al.*[75], an overdoping of Mg resulted in compensating donor (introduction of native donor point defects) and n-type was re-established. It is of course worth noting that PL was effectively quenched with increased Mg content, consistent with previous reports of Anderson *et al.*[61], Jones *et al.*[132], and Wang *et al.*[133]. This matter has left much to be desired for the detailed optical studies in InN:Mg and many aspects of luminescence mechanisms inside the potential p-type region are unknown.

Last but not least, a fundamental hurdle to cross for p-type InN is the unexpected PL quenching. As has been reported by a number of groups, the luminescence of Mg-doped InN commonly exhibited a strongly drop of intensity upon increasing the Mg content[61,76,92,133]. Figure 2.5 shows a significant reduction in the PL intensity somewhat disrupts the detailed optical study inside the "p-type window". A significant interpretation regarding this

observation is yet remaining vague[76,133]. Potential reasoning discussed in the literature included a carrier delocalization in the In-rich region[70,77-79], a larger minority carrier diffusion length in p-InN[76], and the onset of Auger recombination[80,83,84]. The controversy over the physical origin of unexpected PL quenching is far from over and as of yet there has been no convincing conclusion. The investigation of hole conductivity and PL in Mg doped InN is ongoing and also continues in this thesis.

Chapter 3

Photoluminescence Spectroscopy of InN

Today, photoluminescence (PL) is a very common analysis technique as it requires a simple excitation source, usually a laser, and is non-contact meaning that any post-growth processing is unnecessary. The PL features can return the optical property of given material since they are "blackbody-free" radiation. The observed PL emission helps identify a material's own characteristics and purity from both the radiative and non-radiative processes. PL spectroscopy is the main theme of this thesis and used as a diagnostic tool to draw an interpretation of p-InN.

3.1 Luminescence and band structure of InN; Fundamental roadmap

The 'narrow direct bandgap' of InN means that the non-parabolic conduction band minimum (CBM)[32] and the valence band maxima (VBM) directly line up within the same crystal momentum at k=0. This allows photo-excited electrons or holes to recombine without the need for phonon interaction. As is the case for all semiconductors, the conduction band of InN is originated from the outer part of the electron orbital of the atomic structure, giving a *s*-orbital-like In configuration (spherical shape)[38]. Meanwhile the valence band of InN is a *p*-orbital of N ('dumbbell' shape) which can fit into three different quantum vectors. The valence bands can split into states with different angular components as labeled Γ_H (heavy hole), Γ_L (light hole), and Γ_{SO} (split off)[36-38,114]. These bands have the different quantum states (with l=1): the magnetic quantum numbers (m) and spin quantum numbers (j). The spin orbit coupling wave functions $|m, j\rangle$ of the valence band at the Γ-points can be described by

$$\left|\frac{3}{2}, \pm\frac{3}{2}\right\rangle = \frac{1}{\sqrt{2}}|(X + iY)\uparrow\downarrow\rangle, \quad \Gamma_H \tag{3.1}$$

$$\left|\frac{3}{2}, \pm\frac{1}{2}\right\rangle = \frac{1}{\sqrt{6}}|(X + iY)\downarrow\uparrow + 2Z\uparrow\downarrow\rangle, \quad \Gamma_L \tag{3.2}$$

$$\left|\frac{1}{2}, \pm\frac{1}{2}\right\rangle = \frac{1}{\sqrt{3}}|(X + iY)\downarrow\uparrow + Z\uparrow\downarrow\rangle, \quad \Gamma_{SO} \tag{3.3}$$

where, $|X,Y,Z\rangle$ are the orbital wavefunctions of the VBM. ↑ and ↓ denote angular momentum projection quantum numbers of 1/2 (up) and -1/2 (down), respectively. The absorption strength of $e \rightarrow \Gamma_{H,L,SO}$ refers to the component X and Y by assuming the incoming excitation source propagates normal to the film. This means that the emission originating from Γ_H is much intense than that of the Γ_L at the Γ-point and thus $e \rightarrow \Gamma_H$ likely dominates the total absorption spectra (or PL spectra) for InN.

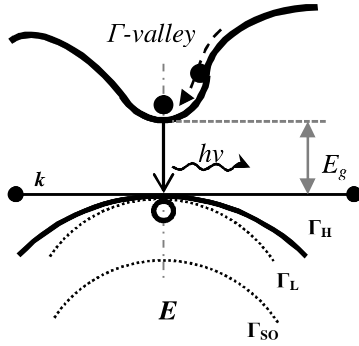

Figure 3.1 A simplified band structure of InN. *hv* is the bandgap (E_g) photon emission energy at the Γ-point. Three different valence bands are labeled as Γ_H (heavy hole), Γ_L (light hole), and Γ_{SO} (split off)

In momentum space $k \neq 0$, the photo-excited electron (and hole) can transit through the quantized levels within the conduction (valence) band by releasing its energy by emitting phonons. This mechanism is known as the intraband transition. At the Γ-point, where the crystal momentum space $k=0$, the electron-hole pair can radiatively recombine across the bandgap with a photon emission, the so called bandgap transition (or band-to--band transition). A simplified schematic of the band structure and a corresponding recombination process at Γ for InN is shown in figure 3.1. There are also several other transitions which lead to the observable PL spectral lines in this research and are the subject of the next few sections.

3.2 Excitons; Shedding more light

Incoming radiation greater than or equal to the bandgap allows electrons and holes to move freely within the respective bands according to dynamics requirements such as mobility, relaxation time and effective mass[41-43]. The uncorrelated electron and hole form an excited

state at the bandgap E_g, but there is also a slightly lower energy excited configuration which is known as an exciton.

Excitons can be formed by photon absorption any place in the Brillioun zone at the same k value. The group velocities of the electron and hole are equal and generate a paired quasi-particle (electron and hole or e-h). The electrostatic Coulomb interaction between e-h pair holds them tightly together like a single orbit[42]. The first discovery of excitons was reported by Frenkel[41] in 1931, and these were associated with excited atoms in insulator lattices.

The energy of an exciton is

$$E_{ex} = E_g - R + \frac{\hbar^2 K^2}{2M} \tag{3.4}$$

where E_g is the bandgap of the given material, R is the excitonic Rydberg constant, K is the wavevector of the exciton, and M is the reduced mass of electron (m_e) and hole (m_h). The first two terms represent the energy difference between the bandgap and the exciton ground state. The second term is closely related to the energy required to break off the e-h pair into free space, the so called binding energy (E_b). The physics behind calculating the binding energy is referred to the hydrogenic atom model (R_H):

$$R_H = \frac{m_o q^4}{32\pi^2 \varepsilon_o^2 \hbar^2} \tag{3.5}$$

where m_o is the free electron mass, q is the electron charge, and ε_o is the dielectric constant (the vacuum). Considering the potential electric field inside the solid, ε_o should be replaced by 'semiconductor dielectric constant' ε_s, and m_o also depends on the effective electron (m_e) mass of given material.

R_H also extends to a size of effective Bohr radius[44] (of exciton atom), which is closely linked to the strength of binding energy. InN has an excitonic radius of approximately 5 nm, which is the largest among III-nitrides[45]. The larger radius is a consequence of the weak Coulomb interaction between the e-h pair (less tightly bound) and a free exciton calculation gives the binding energy of 15.2 meV[45]. One of the key advantages GaN has over InN is the relatively high free exciton binding energy of 25 meV[45].

The aforementioned exciton can be labeled “free” because this system is able to move through the lattice for a short period of time before e-h recombination and is only observed for very pure material[81]. The reality of many semiconductors however, contains many impurities inside the bandgap (imperfections). Before the recombination takes place there is a high probability that the excitons are trapped by defects and consequently lose a slight energy of E_{Loc}, which represents the localized strength to the lattice. This complex is the so called bound exciton and the schematic of figure 3.2 distinguishes the foregoing discussions for the clarity.

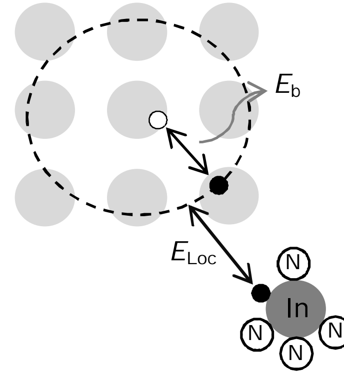

Figure 3.2 The bonding diagram of InN with an extra electron and the schematic of exciton with the binding energy of E_b. The definition of the localization energy is labeled as E_{Loc}.

The exciton can connect with residual impurities such as ionized (D^+) and neutral donors ($D°$) or acceptors ($A°$) and forms the “three body complexes”[253]. For instance, the excitonic emission from a neutral donor bound exciton ($D°X$) consists of two electrons and a hole (2e1h), while a neutral acceptor bound exciton ($A°X$) has two holes and an electron (1e2h). The energies of these complexes can be summarized by

$$E(D^{o}X) = FX - E_{\text{Loc}}(D^{\circ}) \quad (3.6)$$

$$E(A^{o}X) = FX - E_{\text{Loc}}(A^{\circ}) \quad (3.7)$$

The Hayne’s rule implies that E_{Loc} is determined by the effective mass and is in proportion to each other[251]. The photon emission spectrum from $A°X$ therefore appears at lower energy than $D°X$ since the hole effective mass is greater than the electron effective mass[46,47,106].

One major parameter that can ionize the excitonic pair (e-h) into a free particle is the surrounding temperature (k_BT). If the thermal energy of k_BT exceeds the binding energy of E_b, electrons and holes (from e-h pair) can be transferred to their respective bands via phonon interaction. Meanwhile, extra carriers (residual e or h) from the “three-body complex”, which should have a strong binding strength to the crystal lattice, can be formed into a ‘pure’ defect transition of a free-to-bound and is discussed in the following section.

3.3 Free-to-bound and Donor-acceptor pair

InN is ‘heavy’ n-type material; *ie*. it is not a manifestation of a ‘flawless’ semiconductor bulk crystal. As a result, to date there are no reported intrinsic luminescence features such as a band-to-band or excitonic features in the literature. Instead, emission processes involving electrons (holes) trapped to form neutral bound donors ($D°$) (acceptors ($A°$)) practically dominates the low temperature PL, the so called ‘free-to-bound’ transition. The energies of these transitions are

$$E(\hbar\omega) = E_g - E_i \quad (3.8)$$

where E_i is the donor or acceptor energy level. These localized defects generally act as traps and generates a strong non-radiative recombination centre; more details are given in the following section. Boltzmann statistics addresses that the surrounding temperature of $k_B T$ should be less than E_i, allowing the carriers ‘stick’ to the lattice and become optically active:

$$N_i \approx \exp(-\frac{E_i}{k_B T}) \quad (3.9)$$

where N_i is the total concentration of donors or acceptors, k_B is the Boltzmann constant and T is the surrounding temperature.

Donors and acceptors can be present simultaneously. At sufficiently high neutral donors and acceptors are close enough that these sites can form a donor-acceptor pair (DAP) and emit light. These impurities compensate or attract each other by the Coulomb force and thus expect to have large localization energies (a low probability of being ionized). The photon energy of DAP radiation is[44]

$$\hbar\omega_{DAP} = E_g - E_D - E_A + \frac{e^2}{4\pi\varepsilon_o\varepsilon_r R} \quad (3.10)$$

where E_D and E_A are the donor and acceptor ionization energy, e is the charge of the electron, ε_o is the dielectric constant, ε_r is the low frequency relative dielectric constant and R is the distance between electron and hole. The last term represents the Coulomb attraction between donor and acceptor. The direct evidence of DAP transition in PL is a pronounced blueshift as

a function of excitation intensity since a greater number of photo-excited carriers returns the smaller value of R (a shorter distance between e and h).

The formation probabilities of donor and acceptor states can be controlled by the doping concentration, the so called “potential fluctuation” [222-224]. The potential fluctuation is the change in the formation of neutral bound state. In the case of heavy n- (p-) type doping, the wavefunctions of donors (acceptors) significantly overlaps. This gives a fall (rise) to electronic states (or energy) towards the midgap and tightens the distance between donor and acceptor sites due to the strong electric field. The electronic states at deep level possess the most effective non radiative recombination centres, due to a high probability of capturing carriers[82]. Non-radiative recombination via a deep trap is called the Shockley-Read-Hall (SRH) process[257]. SRH is very closely related to Auger recombination, which is the subject of the next section.

3.4 Auger recombination; Luminescence quenching effect

Auger recombination is not a typical electron-hole recombination, which emits a photon across the bandgap. As displayed in figure 3.3, Auger is ‘non-radiative’ recombination involving a third particle (electron or hole; depends on the material type), which ‘absorbs’ the energy given off by the return to equilibrium process and also emits a phonon[83,84]. The genuine physical origin of the Auger is still mystery but its process can be tentatively described. The non-radiative recombination is strongly correlated to SRH and Auger recombination processes. The non-radiative lifetime (τ_{NR}) approximation in semiconductors is given by[88]

$$\frac{1}{\tau_{\mathrm{NR}}} = \frac{1}{\tau_{\mathrm{SRH}}} + C_{\mathrm{p}} n^2 \tag{3.11}$$

where τ_{SRH} is the carrier recombination lifetime of SRH, C_{p} is the Auger coefficient and n is the density of electrons or holes. Auger process can occur inside either the conduction (two electron, n-type)[85,86] or valence bands (two holes, p-type)[87-89]. The schematics of Auger dynamics in crystal momentum space k, are depicted in the figure 3.4.As indicated in the last term of equation 3.11, the strength of the Auger rate strongly depends on the carrier concentration and the surrounding temperature should be of less concern[85-89].

In practice the onset of Auger recombination can readily be recognized from time resolved differential transmission (TRDT) measurements. As has been reported, a single-exponential decaying carrier life time is observed for a n-InN (or undoped InN) sample, which is based (only) on a typical of SRH recombination[16]. But if $C_p n^2$ is activated by external factors such as a doping, Auger processes should trigger a clear concentration dependent carrier lifetime into a bi-exponential decay curve. Arguably, this factor may dictate the luminescence quenching effect in Mg-doped InN studies[61,133].

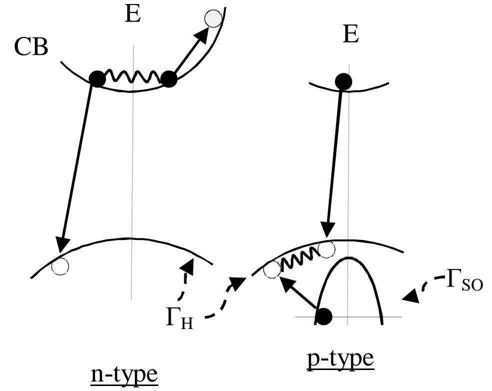

Figure 3.3 The schematics of the Auger (n- and p-type) recombination mechanisms.

3.5 Moss-Burstein effect and InN bandgap

Another interesting luminescence aspect showing a carrier concentration dependence is the Moss-Burstein effect[29,162]. This band filling effect enhances the background electron concentration. This simultaneously increases the Fermi level (E_F) as states in the conduction band become filled and occupied by degenerate electrons.

The theoretical treatment of Kane's two-band perturbation model can verify the Moss-Burstein induced optical transition[51], which strongly correlates to the position of Fermi level (or vector). This approximates the CBM energy as a function of the carrier concentration[51].

$$E_C(n) = E_g + \frac{\hbar^2(3\pi^2 n)^{2/3}}{2m_e} + \frac{1}{2}\left(\sqrt{E_g^2 + 4E_P\frac{\hbar^2(3\pi^2 n)^{2/3}}{2m_e}} - E_g\right) \qquad (3.12)$$

E_C is the CBM energy, E_g is the bandgap energy, m_e is the electron effective mass, n is the carrier concentration, and E_p is the conduction band energy related matrix parameter. The second term describes the position of the Fermi level inside the conduction band as a function of background electron concentration. The bandgap of 0.67 eV[24], the conduction band energy matrix of 10 eV (E_p varies between 7.5 and 15 eV for III-Nitrides)[52], and the electron

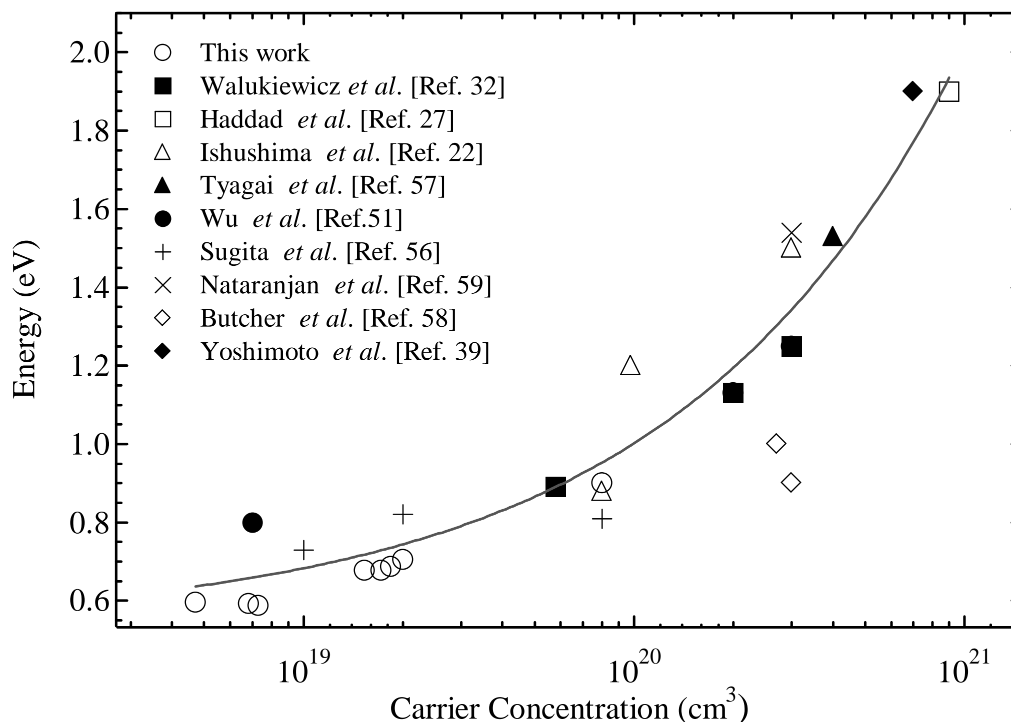

Figure 3.4 Reported PL and absorption bandgap data as a function of carrier concentration for InN (or InN:Mg) thin films. Kane's two-band perturbation model is plotted and describes the Moss-Burstein effect.

effective mass of 0.07[53] are used in this fitting. This calculation considers that InN has a strong *k* vector at the Γ-point, which is often the case for semiconductors with a small bandgap[49,50,162]. This effect significantly narrows the 'vertex' of the conduction band profile and reduces the effective electron mass[32]; more details are given in section 3.6.

Figure 3.4 illustrates a wide range of reported bandgap data with the correspondent background electron concentration and the Moss-Burstein shift is calculated from equation 3.12. Worth noting is that the Moss-Burstein induced electrons in the conduction band should be highly degenerate[91,92,154]. This statement assumes that the Fermi level of InN is approximately located 1.6 eV above the VMB as reported elsewhere[67,68]. In order for InN (or electrons in the conduction band) to be non degenerate, the background electron concentration should be significantly lowered and sits at least 75 meV ($3kT$) away (below) from the CBM[229].

Perhaps, the Kane's two band model is not suitable to determine the Fermi level inside the bandgap since this approximation considers the CBM as the threshold point that the Fermi level can be reached (lowered). The simple distribution function can estimate a wide range of

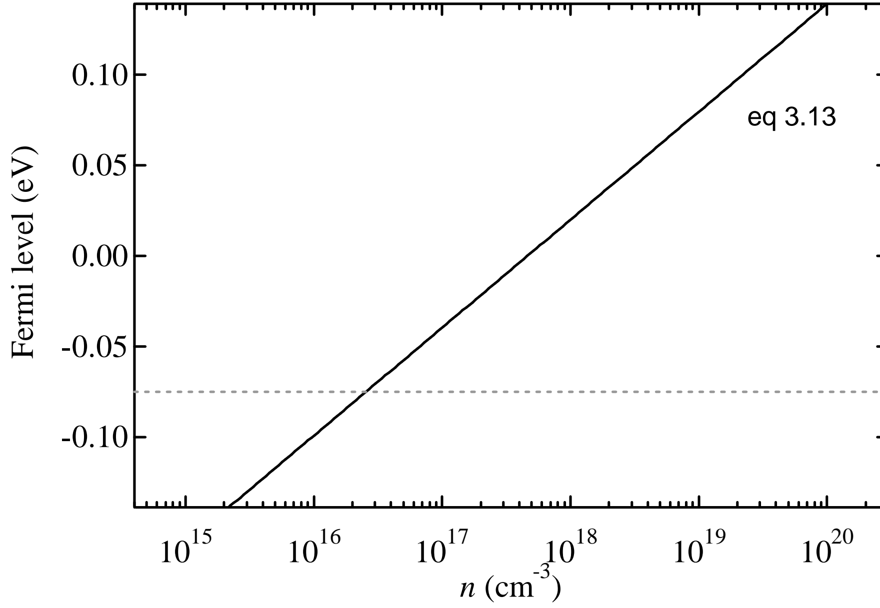

Figure 3.5 The calculated Fermi energy level corresponds to the background electron concentration (m_e: 0.07, and E_g:0.67 at 300K). The conduction band minimum lies at 0eV. The dotted line ($3kT$ away from the CBM) represents the transition between degenerate (above) and non-degenerate (below) level for InN.

the Fermi level position (E_F) with respect to the carrier density (n) of given material[228].

$$n \cong \int_{E_C}^{\infty} \frac{8\pi\sqrt{2}}{h^3} m_e^{3/2} \sqrt{E_g - E_C} e^{\frac{E_F - E_g}{kT}} dE_g = N_C e^{\frac{E_F - E_C}{kT}} \tag{3.13}$$

with

$$N_C = 2\left[\frac{2\pi m_e kT}{h^2}\right]^{3/2} \tag{3.14}$$

where E_C is the energy of the CBM and N_C is the effective density of states in the conduction band. For the consistency, the same values of parameter (from eq. 3.12) were used in this analysis. The theoretical treatment using equation 3.13 is shown as the solid line in figure 3.5. Accordingly, the transition involving non-degenerate electrons in InN should have the background electron concentration equal or less than 3×10^{16} cm^{-3}. This estimation seems to be realistic and coincides well with a reported non-degenerate carrier concentration of 6×10^{16} cm^{-3} for n-InN as calculated from the free-electron recombination model (FERB) model elsewhere[91].

3.6 Temperature dependent Arrhenius decay

A single PL spectrum on its own is not adequate to address the observed transitions. In order to identify the physical origins precisely, further analysis is required. The technique that can lead to a solid analysis is temperature dependent PL. The PL intensity as a function of temperature typically decreases due to many reasons including an enhanced electron-phonon interaction, a greater amplitude of scattering effect, and a thermal decay of e-h pairs (excitons). These temperature evolutions of PL intensities generally follow the thermal Arrhenius-type decay and are dictated by the activation energy, which can deliver a convincing understanding of the observed transitions.

Boltzmann statistics describes the luminescence intensity of a transition varying with the temperature (T) as

$$I(T) = \frac{I_o}{1+A\exp\left(\frac{-E_a}{k_B T}\right)} \tag{3.15}$$

where I_o is the intensity at absolute zero temperature, A is a prefactor describing the efficiency of the nonradiative channel, E_a is an activation energy of given transition, and k_B is Boltzmann's constant. The typical use of this model is to verify the types of luminescence by matching the extracted activation energies to the accepted values. Perhaps an appropriate usage in InN is to describe the formation of impurity levels. The evaluation of activation energy identifies the depth of embedded states, which corresponds to the non-radiative channel. The description of the activation process is schematically shown in figure 3.6.

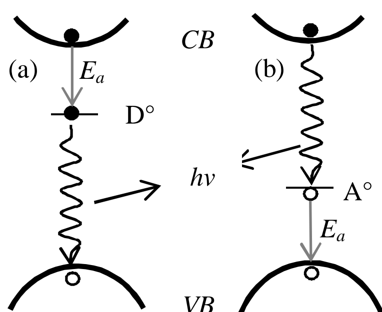

Figure 3.6 The schematics of thermal Arrhenius decay and the activation energy (E_a) for (a) a neutral donor bound state and (b) a neutral acceptor bound state. Wavy and straight lines indicate photon and phonon emissions, respectively.

In reality, the experiment is conducted over a wide range of temperatures. As such a single non-radiative path may not be ideal. An unfortunate problem with InN is a tendency of multi-non-radiative processes and analyses based on equation 3.15 often show a limitation in plot fitting. The notion is that the principal mechanism of 'luminescence quenching' describes two different processes: 1) thermal release of 'bound' carriers, and 2) capture in a

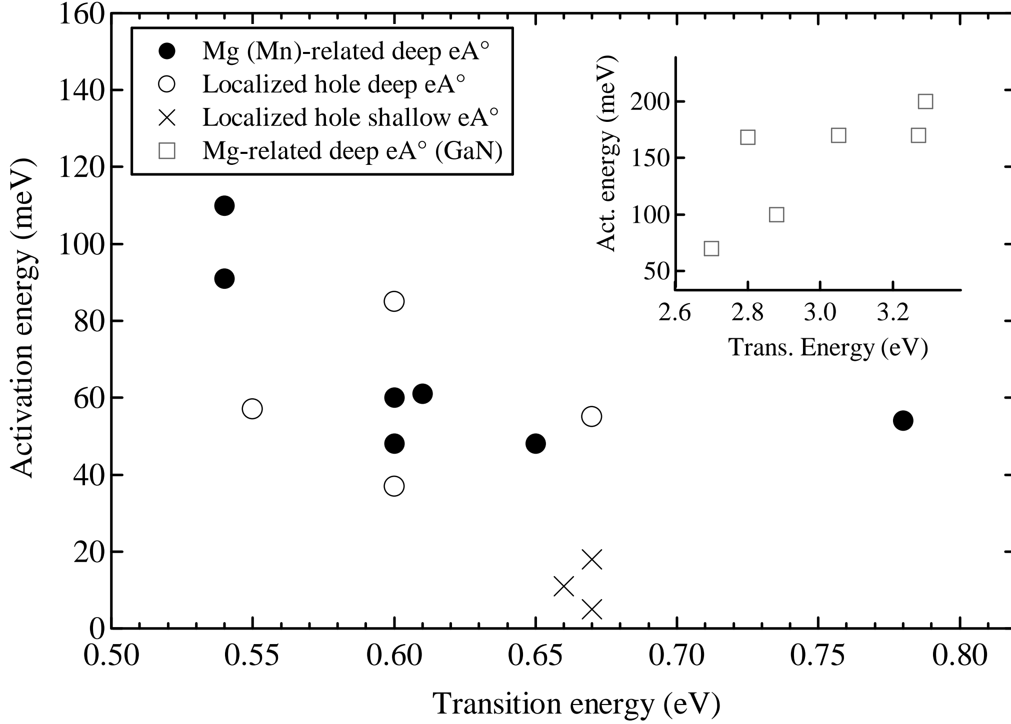

Figure 3.7 The plot of activation energies of Mg-related deep acceptor[61,92,75,133,this work], localized residual deep acceptor[90,91,this work], and localized residual shallow acceptor[90,91,this work] states found in literatures (InN). The inset shows the reported Mg activation energies in GaN[93,217,219].

non-radiative recombination channel. Both processes should significantly contribute to the temperature induced quenching process and therefore, two non-radiative decay paths can be considered[93,242,246].

$$I(T) = \frac{I_0}{1+A\exp\left(\frac{-E_a}{k_B T}\right)+B\exp\left(\frac{-E_b}{k_B T}\right)} \quad (3.16)$$

E_a represents the localization energy of a given transition in the high temperature region, involving the formation of a non-radiative channel with respect to either the CBM or VBM. E_b represents the activation energy of a second non-radiative decaying process, which is the energy requires to thermally release trapped carriers in the low temperature region. A and B describe the strength of the quenching process for given channel. This interpretation assumes that the observed transition is a free-to-bound.

In n-InN, the activation energies of the residual free-to-shallow acceptors and free-to-deep acceptors are 5-15 meV and 50-60 meV, respectively[90,91]. The deep acceptors associated with Mg in (In,Ga)N are characterized by the activation energies of 48-110 meV[61,69,75,133], and 120-200 meV[93,216-219], respectively (figure 3.7). The behavior of Mg as an acceptor in III-

nitride is closely linked to the hole effective mass, which is strictly the wavevector dependent. This configuration can be referred to the standard definition of

$$m^* = \hbar^2 \cdot \left[\frac{d^2\varepsilon}{dk^2}\right]^{-1} \tag{3.17}$$

where m^* represents the effective mass of either electron or hole and ε is the energy as a function of wavevector k. A smaller value of k draws a "broader" band profile, which returns a larger effect mass. By following the Hayne's rule, this circumstance promotes a greater localization strength (or activation energy) on the lattice site. As shown in the inset of figure 3.7, GaN[54,55] has a larger Mg activation energy than those from InN. As discussed in the previous section, InN has a comparably strong value of k at the Γ-point, dictating small effective masses.

3.7 Bose-Einstein and Pässler; The bandgap shrinkage

Another luminescence aspect related to the temperature dependent PL is the energy shift. PL peak positions generally follow the "bandgap shrinkage effect" and give a decrease of energy (redshift) as a function temperature[94]. This is mainly due to a combination of 1) the greater amplitude of atomic (or lattice) vibration[94,95] and 2) the increase of electron-phonon interaction[94,110] with increasing temperature. Phenomenologically, the temperature-induced bandgap shrinkage effect generally well fits into the Einstein approximation of Pässler formula[95], which can be expressed by

$$E(T) = E_g(0) - \frac{\alpha\Theta}{2}\left[\sqrt[p]{1 + \left(\frac{2T}{\Theta}\right)^p} - 1\right] \tag{3.18}$$

Here, E_g is the bandgap at an absolute temperature T, α is the electron-phonon interaction, and the coefficients Θ and p are related to the Debye temperature of a given material and the electron-phonon spectra functions, respectively[92]. The key weakness of this relation is that the model contains a large number of adjustable parameters and fitting into a wide range of practical data is often appeared be rather cumbersome.

A better and simple semi-empirical model by Viña *et al.*[110] is very useful Bose-Einstein version

$$E_g(T) = E_g(0) - \frac{\alpha\theta}{\exp(\theta/T)-1} \quad (3.19)$$

where α is the electron-phonon interaction and θ is the effective phonon temperature. This equation puts more weight on the electron and phonon interaction being the main reason for the bandgap shrinkage [96,109]. Perhaps a more rigorous approach for InN is to consider the sum of the bandgap value (E_g), the Moss-Burstein effect ($E_g+\Delta_{MB}$), and the probability formation of an acceptor state ($E_g+\Delta_{MB}-E_a$) in order to detail ΔE_g value.

Table 3.1 Bose-Einstein and Pässler parameters of InN

Bose-E. (eq. 3.20)	$Eg(0)$ (eV)	α (meV/K)	θ (K)	-
this work., #555	0.59	0.15	681	-
this work., #714	0.67	0.37	681	-
this work., #713	0.68	0.31	681	-
Ref. 100	0.65	0.4	681	-
Ref. 101*	3.5	55	309	-
Pässler (eq. 3.19)			Θ (K)	p
this work., #555	0.59	0.3	576	1.8
this work., #714	0.67	0.6	576	2.1
this work., #713	0.68	0.2	576	1.7
Ref. 112	0.68	0.55	576	2.2
Ref. 98*	3.5	0.53	400	2.6

represents the sample number in this study (an uncertainty of α is less than 1%).

*Fitting results for n-GaN

The parameters using Viña and Pässler models are listed in table 3.1. The effective phonon temperature of 681 K and the Debye temperature of 576 K are used in the fittings[112]. The other parameters from the fits are consistent with the reported values elsewhere[100,112]. An influence of a thermal lattice vibration and an electron-phonon interaction on the bandgap is relatively weaker than GaN[55,116]. As reported elsewhere, the bandgap shrinkage of InN is limited to 65 meV[32,90] from a 4 K to 300 K, whereas GaN can shift as much as 72 meV[55,116]. Potential reasons include the difference in 1) specific transition types, 2) the strength of

electron-phonon interaction [247], 3) the bandgap energy, and 4) a presence of surface electron accumulation layer[119].

3.8 Excitation intensity dependent PL

Excitation intensity PL dependence is also a strong analytical treatment to discover the true origin of observed transitions. The PL components generally exhibit their own response to photo-excitation and the interpretation regarding this 'criteria' is significantly addressed in a number of publications[113, 169-171,255]. Commonly described was that the PL emission intensity can be characterized by a power law $I \sim L^k$, where I is the PL intensity , L is the laser power, and k is the parameter describing the recombination process (a slope of log-log plot). The genesis of coefficient k can be traced to the Shockley-Read Hall (SRH) recombination[257] involving an exponential decay rate term with respect to time.

$$R = \frac{dn^{\mathrm{e,h}}}{dt} = N_{\mathrm{C,V}} \cdot \exp\left(-\frac{E_F^{\mathrm{e}} - E_F^{\mathrm{h}}}{kT}\right) \tag{3.20}$$

Here $n^{\mathrm{e,h}}$ is the carrier density of electron or hole, $N_{\mathrm{C,V}}$ is the effective density of states in the conduction or valence bands, and E_F is the Fermi energies. The notion is that the e-h recombination probability should be dictated by both electron and hole concentrations. In the simplest form, the band-to-band transition should return two emitting photons from a single excitation as anticipated from having both types of carriers, whereas other recombination processes involving some impurity states, where the recombination process likely is biased towards one particular dominant carrier, and gives a less amount of photons than those from the band-to-band.

A 1992 excitation power dependence study by Schmidt *et al.*[133] rigorously approached the excitation dependent PL calculation and comprehensively described the near-band-edge luminescence with a complicated rate equation of

$$\frac{dn}{dt} = iL - an^2 - gn(N_D - N_{D^0}) - enN_{A^0} \tag{3.23}$$

where n (p) is the electron (hole) concentration, and the coefficients a to i are transition rates of the designated recombination processes as depicted in figure 3.8, L is the excitation power, and N_D, N_{D°, and N_{A° are the donor, neutral donor, and neutral acceptor concentrations, respectively. Figure 3.8 describes the summary of PL transitions, which have been thoroughly covered in a last few sections. The radiative and non-radiative processes are depicted in wavy and straight lines, respectively, and the arrows point to the direction of transition rates (or recombination processes).

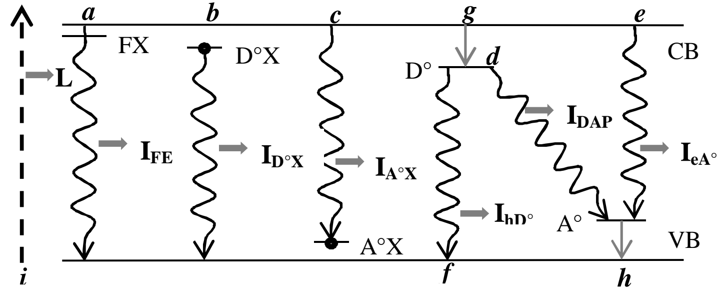

Figure 3.8 The summary of described recombination processes in schematic[133].

This analysis accounts for all possible recombination processes inside the bandgap. The first term expresses the excitation rate from the laser, the second term gives the recombination rate for the free exciton, and the last two terms represent a combination of the return to equilibrium rates involving the non-radiative (former), and radiative (latter) centres, respectively for free-to-bound transitions. For the simplicity, this analysis assumed n=p (n^2) and used the constant values of concentrations for neutral bound states. More detailed rate equations for free, donor and acceptor bound excitons were further specified in this literature.

$$\frac{dn_{FE}}{dt} = an^2 - \left[\frac{1}{\tau_{FE}} + \frac{1}{\tau_{FE}^{nr}}\right] n_{FE} - bn_{FE}N_{D^0} - cn_{FE}N_{A^0} \tag{3.24}$$

$$\frac{dn_{DX}}{dt} = bn_{FE}N_{D^0} - \left[\frac{1}{\tau_{DX}} + \frac{1}{\tau_{DX}^{nr}}\right] n_{DX} \tag{3.25}$$

$$\frac{dn_{AX}}{dt} = cn_{FE}N_{A^0} - \left[\frac{1}{\tau_{AX}} + \frac{1}{\tau_{AX}^{nr}}\right] n_{AX} \tag{3.26}$$

Here τ and τ^{nr} represents the radiative and non-radiative lifetimes for the designated transitions. Similar to Fouquet and Siegman, the photon emission rates (in the steady state) of given transitions can be simplified to

$$I_{FE} = \frac{n_{FE}}{\tau_{FE}} = \frac{\beta}{\tau_{FE}} n^2 \tag{3.27}$$

$$I_{DX} = \frac{n_{DX}}{\tau_{DX}} = \frac{bN_{D^0}\beta}{1+\frac{\tau_{DX}}{\tau_{DX}^{nr}}} n^2 \tag{3.28}$$

$$I_{AX} = \frac{n_{AX}}{\tau_{AX}} = \frac{cN_{A^0}\beta}{1+\frac{\tau_{AX}}{\tau_{AX}^{nr}}} n^2 \tag{3.29}$$

where β is the a factor that can be defined from the terms in equation 3.24 under steady state conditions.

This study proposed two different cases, where the majority of luminescence is dominated by 1) the excitonic or 2) the defect-related transitions. The former assumes return to equilibrium is dictated by e-h pair recombination (of free exciton) through the coefficient *a* and its dominance ignores the trap-assisted recombination (the last two terms of eq. 3.23). When applied this excitonic case simplifies equation 3.23 into a $n\sim L^{0.5}$ relation and consequently through equation 3.27 the intensities $I\sim L$.

The second case is vice versa, which neglects the free exciton (e-h pair) recombination process of coefficient *a*. This indicates the photons mainly being emitted through SRH recombination and the equation 3.23 gives $n\sim L$.

By substituting the two above cases for *n* (from eq. 3.23) into equations 3.27-3.29, these yield

$$I_{FE} = \frac{\beta}{\tau_{FE}} \frac{i^{1,[2]}}{\left[eN_{A^0}+g(N_D-N_{D^0})\right]^2} L^{1,[2]} \tag{3.30}$$

$$I_{D^0X} = \frac{bN_{D^0}\beta}{1+\frac{\tau_{DX}}{\tau_{DX}^{nr}}} + \frac{i^{1,[2]}}{\left[eN_{A^0}+g(N_D-N_{D^0})\right]} L^{1,[2]} \tag{3.31}$$

$$I_{A^0X} = \frac{cN_{A^0}\beta}{1+\frac{\tau_{AX}}{\tau_{AX}^{nr}}} + \frac{i^{1,[2]}}{\left[eN_{A^0}+g(N_D-N_{D^0})\right]} L^{1,[2]} \tag{3.32}$$

The square parentheses designate the second case. A combination of the two different cases returns the PL intensity (*I*) in a range of quadratic to linear relations as a function of excitation intensity (*L*). In practice, the power dependent PL intensity of a free exciton transition is closer to a quadratic form (similar to a band-to-band) than of bound excitons, which typically gives a linear characteristic (*ie.* $n\neq p$) [169-171].

Excitation power dependent of a free-to-bound transition is not comprehensively covered by either Fouquet and Siegman[225] or Schmidt *et al.*[133], although the latter literature stated the number of photons produced by the excitation of a such transition should be proportional to a impurity-involved transition rate. As expected, this type of return to equilibrium process is

actually ‘not so equilibrium’, having the carrier density (or a portion) biased towards one particular type (*ie*. $n>>p$ for eq. 3.23 and therefore gives $I_{hD^\circ} \sim nN_{D^\circ}$). By applying the same assumptions of case 1) and 2), the photon emission rate of a free-to-bound can be expressed by

$$I_{hD^0(eA^0)} \sim N_{D^0(A^0)} + \frac{i^{1/2,[1]}}{\left[eN_{A^0}+g(N_D-N_{D^0})\right]^{1/2}} L^{1/2,[1]} \tag{3.33}$$

This gives the sub-linear relation of power dependent PL intensity. This dynamic is logically understandable considering there are a significant number of phonons from typical free-to-bound transitions and thus on average much less than one photon is returned from a single injected excitation.

In summary, coupled rate equations from both literatures[133,225] suggest that the power-law coefficient k signifies ‘k=2’, ‘2>k>1’, and ‘1>k’ for the band-to-band, excitonic, and impurity-related transitions, respectively.

3.9 Experimental consideration; The design and implementation

A variety of experimental tools are employed in this PL study. A schematic diagram of the experimental set up used for the PL spectroscopy measurements is depicted in figure 3.9. The first step of the experiment is to attach the InN thin films to a copper sample holder using a silver past and place them inside an Oxford microstat. This microstat is connected to a helium storage dewar with a transfer tube, which brings the helium gas into the system. A nitrogen cold trap assisted vacuum pump allows a continuous evacuation with a pressure of 10^{-3} torr even at the liquid helium temperature of 4 K.

Various wavelengths of the excitation sources were also employed. A 488nm line of a Spectra-Physics model 2080 argon laser with an available power range of 100 mW – 1 W, a 150mW photodiode module operating at 650 nm, and a 808 nm line of a diode laser with output of 200 mW were used as excitation sources. The diffusion of light emission from a material strongly depends on the penetration depth of the excitation photons. The intensity of

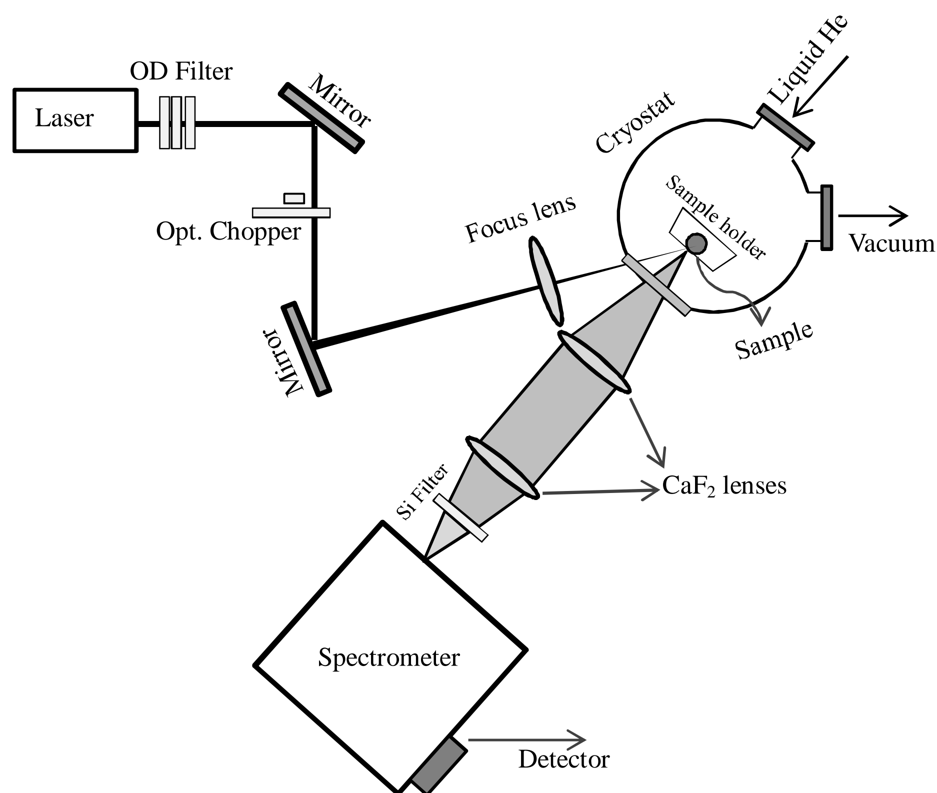

Figure 3.9 A schematic diagram of the experimental setup used for photoluminescence.

light can be referred to the Beer-Lambert law[115].

$$I(z) = I_o e^{-\alpha z} \tag{3.34}$$

with

$$\alpha(E) = \alpha_o \sqrt{\frac{E-E_g}{E_g}} \tag{3.35}$$

where I_o is the intensity of the light before it penetrates the given material, I is the light intensity as a function of thickness z, and $\alpha_o = 1.5\times10^5$ cm^{-1} is the absorption coefficient of InN at room temperature[252].

This approximation is originated from the 'Fermi golden rule', where the transition rate from an initial to final quantum state is proportional to the photon energy-induced density of states (DOS). The inverse of the absorption coefficient α^{-1} is wavelength dependent (of the specific laser employed) and describes a penetration depth of the photon transmission through a thin film. The average depth that a photon reaches for a 488 nm Argon, a 650 nm ,and a 808 nm laser module using above theoretical calculation yields 39, 48, and 57 nm, respectively.

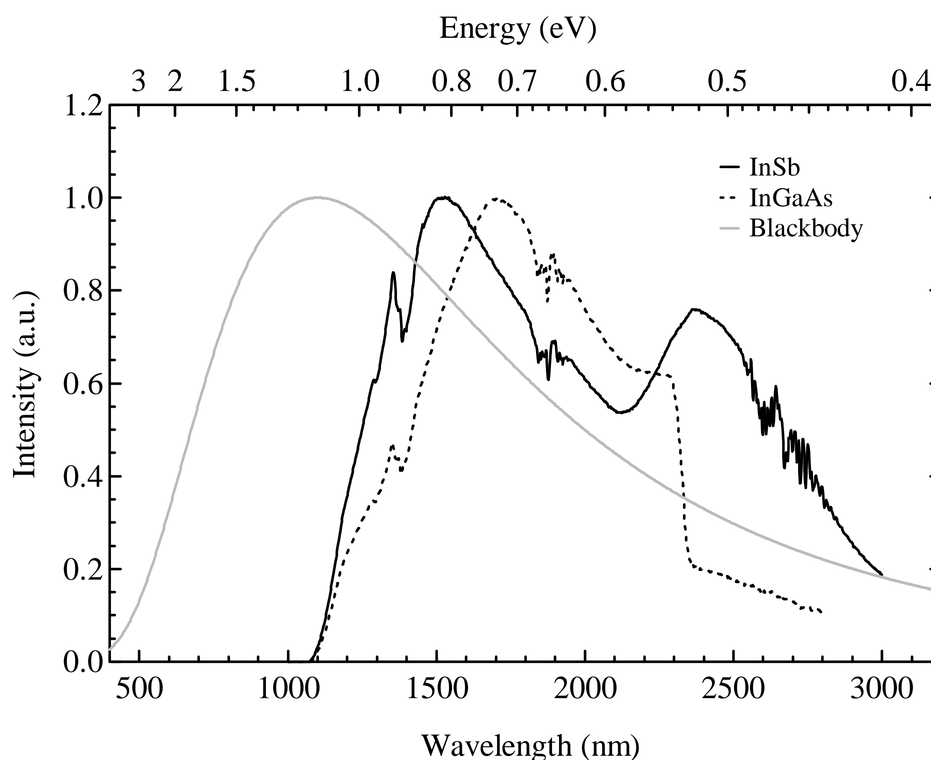

Figure 3.10 The blackbody radiation curves for InSb and InGaAs detectors.

The sample holder is connected to a temperature sensor via a resistive heater wire. This sensor communicates with an Oxford PID (proportional-integral-differential) temperature controller, allowing a wide range of temperature. Optical density (OD) filters are used for an excitation intensity dependent PL study.

PL is measured in a back-scattering geometry. The angle of the laser beam is directed by two adjustable mirrors. An excited emission is collected, collimated and focused into a 0.15 m imaging dual grating Acton spectrometer by using two CaF_2 lenses. A Si filter is employed to block the laser scatter. A 300 lines per mm diffraction grating with a blaze angle of 2 μm is used for the light dispersion and a HeNe laser served as the calibration source. Liquid nitrogen cooled InSb or InGaAs detectors are attached to the spectrometer which results in observable PL spectra from all samples.

Figure 3.10 shows the normalized detector response in terms of blackbody radiation. A tungsten coiled quartz iodine lamp was the blackbody source. As seen in the figure, the disadvantage of the InGaAs detector is the short wavelength coverage. Its performance at 2300 nm creates a steep fall off, where the luminescence from InN is expected to be present.

Thus, the available detecting range between 1 - 3.3 μm of InSb is the priority in the experiments. Notwithstanding, the greater efficiency of the InGaAs detector renders it useful for the films with a weak luminescence.

The noticeable dips in the measured spectra are due to OH vibration. This atmospheric water molecule somewhat perturb optical measurement. During this research, there were attempts to minimize the water absorption. A Perspex box was constructed to isolate the entire PL system from the atmosphere by purging with a flow of N_2. Despite the intensive effort, the prominent effect was far from eliminated.

Finally, the data is acquired by detectors in the alternating current mode. In order to convert the signal from the direct to alternating, the laser beam routed through a rotating blade chopper. The frequency of rotation is adjustable but no dramatic effect upon its value was found. The collected PL signal from the detector is conveyed to the Lock-in amplifier where the data acquisition is digitized and recorded by the software controlling the spectrometer scan.

Chapter 4

Nitrogen-rich Magnesium doped Indium Nitride

A number of research groups have made great contributions to the fundamental development of p-InN. The recent availability of high quality InN thin films has provided a plentiful understanding of both optical and electrical properties of p-InN. Still, many problems in interpreting the luminescence spectra of p-InN are yet to be resolved. Particularly, a lack of luminescence from a quenching effect with an acceptor dopant is the main drawback. Consequently, a detailed analysis of the optical study remains vague. Herein, a series of Mg doped InN on YSZ substrates was prepared to obtain a clearer picture of luminescence dynamics in InN:Mg.

4.1 The growth parameters and electrical properties.

Growth, SEM, and SFH by Dr. Chito Kendrick at University of Canterbury

SIMS by Dr. Richard Morris at University of Warwick

The growth criteria for all the films in this study followed the description in Appendix A. Twelve Mg doped InN epilayers were grown in a cryo and ion pumped Perkin Elmer 430 plasma-assisted MBE system on YSZ (111) substrates. Conventional Knudsen effusion cells were used to deposit both In and Mg under N-rich growth conditions. The Knudsen equation[138] distinguished the flux requirement for N-rich conditions and the threshold was below an In flux of 3.1×10^{14} atoms $cm^{-2}s^{-1}$. In order to evenly distribute doping density in a range of samples, the Mg cell temperature was varied from 170 to 370 °C.

The growth rate of the films was approximately 150 $nmhr^{-1}$ which returned approximately 450 nm thickness. Based on the thickness dependent study in Appendix B, even 0.5μm thick

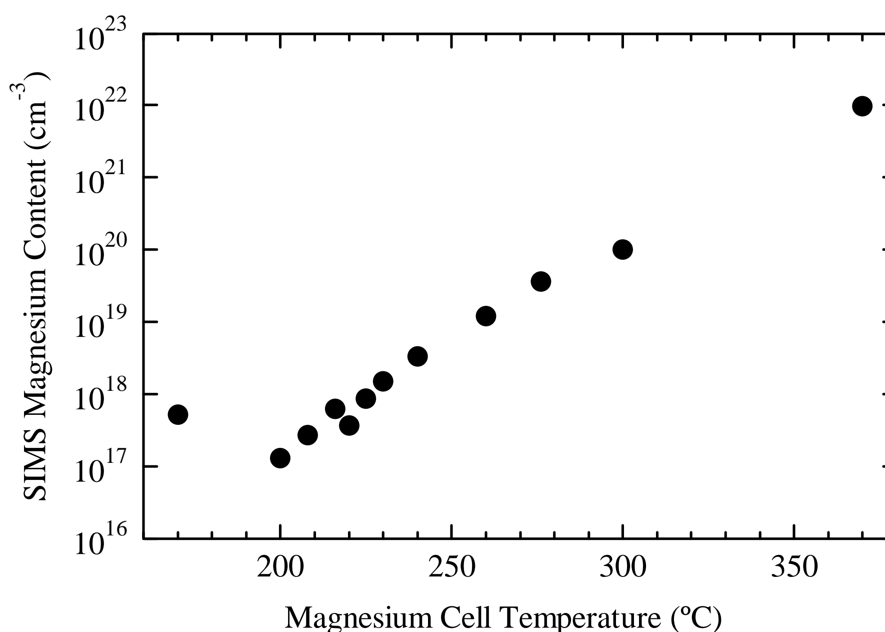

Figure 4.1 SIMS Mg concentration of a N-rich InN:Mg/YSZ series as a function of Mg deposition source temperature.

InN films can give an encouraging electron concentration range. In hindsight, the thickness of an InN epilayer should not be less than 1μm due to the threading dislocations of heteroexpitaxy growth of InN[176]. Subsequent to growth, the Mg concentration was determined based on SIMS analysis [Appendix A]. As shown in figure 4.1, the Mg concentration value was found to be within a range of 3×10^{17} to 1×10^{20} cm^{-3}, although the Mg distribution through the depth is questionable. Worth noting is a linear relationship between SIMS Mg concentrations and Mg growth temperatures. This linear profile implies a fixed fraction sticking of Mg on InN/YSZ, although this may depend on substrate temperature.

The physical alignment of atoms, the so called ‘polarity’ is also an important parameter to consider. In a study by Li *et al.*[174], the surface polarity was found to be the key factor to achieve p-type GaN:Mg, where the direct p-type surface contact was feasible for the sample grown on a Ga-face ,whereas a N-polar face was switched to n-type (was in fact semi-insulating). In order to evaluate the polarity of the films, analyses of wet etching using a KOH solution was examined. The determination of the polarity by wet etching is based on the observation of the surface morphology: In polar films have a smooth surface, whereas N-polar films should show increased roughening of the surface. In this series, the polarity of N-rich InN:Mg/YSZ readily fluctuates as a function of Mg concentration; more details are given

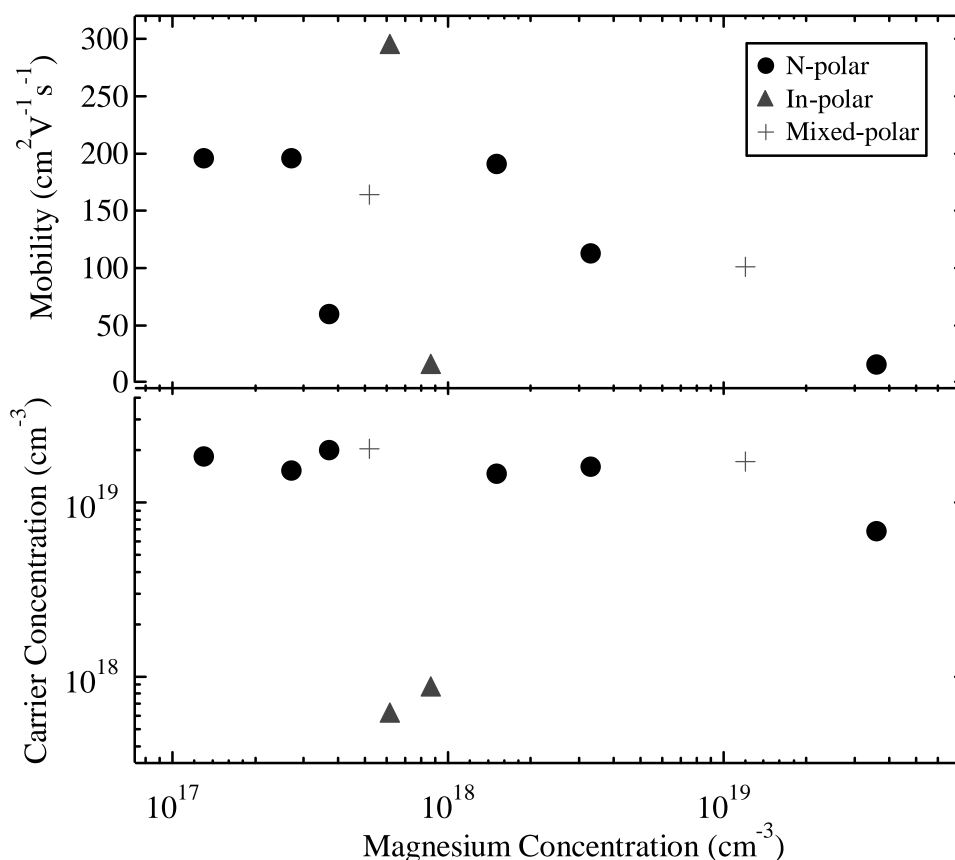

Figure 4.2 SFH electrical properties of a N-rich InN:Mg/YSZ series as a function of Mg concentration.

in the following section. This phenomenon is in contrast to recent polarity dependent studies of N-rich GaN:Mg[144] and InN:Mg[155], where the polarity inversion was unseen in the both cases. A direct consequence of this event is still unknown.

Single magnetic field Hall effect (SFH) measurements revealed the electrical property of InN:Mg [Appendix A]. As displayed in figure 4.2, the SFH carrier concentration of N-rich InN:Mg/YSZ is rather insensitive to Mg and scattered in the range of 2×10^{19} to 5×10^{18} cm^{-3}. The surface electron accumulation layer renders Hall effect measurement very inaccurate and provides the high value of the carrier concentration and returned n-type carriers[31,67,68,71]. The carrier concentration as extracted from In-polar surface are approximately an order of magnitude less than those films with N-faces, notwithstanding that the Mg content is within a similar range. This result infers that the distribution of electrons in a N-polar surface may be greater than in a In-polar InN[135]. However, electron mobilities determined from this type of measurement are not consistent with such an understanding and show a general trend of

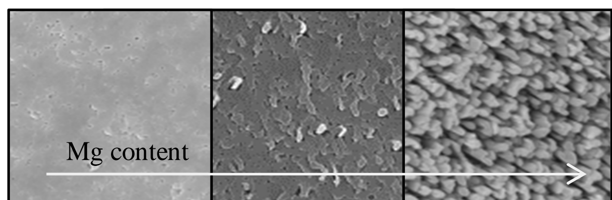

Figure 4.3 SEM images of the InN:Mg/YSZ films grown with SIMS Mg concentrations of; left) 1.3×10^{17} cm^{-3} , middle) 3.7×10^{17} cm^{-3}, and right) 9.5×10^{21} cm^{-3}.

decreasing mobility as a function of Mg concentration. This phenomenon is likely associated with increased roughening of the surface as was seen in heavily Si doped GaN (n-type), where the surface roughness significantly lowers the electron mobility [239]. The summary of electrical properties is listed in table 4.1 (the samples of this work).

The surface morphology of N-rich InN:Mg was examined by scanning electron microscopy (SEM) [Appendix A] and the image shows a strong correlation to the Mg concentration as presented in figure 4.3. As the Mg concentration is increased, the roughening of the surface becomes more apparent. As expected from N-rich growth, indium droplets are not present. For the highest doping level, the surface breaks and migrates to 'nano-rod-like' structure.

Table 4.1 A summary of growth conditions and Hall effect measurements of Mg doped InN/YSZ films.

Film #	Polarity	T_{Mg} (°C)	Mg_{conc} (cm^{-3})	μ ($cm^2V^{-1}s^{-1}$)	n cm^{-3}
579-InN:Mg	Mix	170	5.2×10^{17}	164	2.03×10^{19}
577-InN:Mg	N	200	1.3×10^{17}	196	1.84×10^{19}
601-InN:Mg	N	208	2.7×10^{17}	196	1.53×10^{19}
585-InN:Mg	In	216	6.2×10^{17}	295	4.71×10^{18}
590-InN:Mg	N	220	3.7×10^{17}	59.8	2×10^{19}
555-InN:Mg	In	225	8.7×10^{17}	16.3	7.31×10^{18}
594-InN:Mg	N	230	1.5×10^{18}	191	1.46×10^{19}
580-InN:Mg	N	240	3.3×10^{18}	113	1.6×10^{19}
584-InN:Mg	Mix	260	1.2×10^{19}	101	1.72×10^{19}
583-InN:Mg	N	276	3.6×10^{19}	16.3	6.82×10^{18}
557-InN:Mg	In	300	1.0×10^{20}	4.93	1.86×10^{19}
554-InN:Mg	-	370	9.5×10^{21}	-	-

Note: N → N-polar, In → In-polar, μ → Mobility, n → Carrier concentration

4.2 Optical properties of N-rich InN:Mg/YSZ(111)

TRDT by Dr. Maurice Cheung at The State University of New York

Photoluminescence (PL) measurement has been a critical part of this research determining the optical properties of Mg-doped InN. PL was measured by using a 650 nm line of diode module laser (a 200 mW excitation power) and an InSb detector. Figure 4.4 shows the PL spectra of InN:Mg thin films at liquid helium temperature. Worth noting is that for the first time in this material a complete set of optical characterization is successfully displayed throughout a wide range of Mg concentration, which may cover both the potential n-and p-type windows. A number of samples show multiple overlapping PL components which form an asymmetric broad emission. This configuration differs from other reports, where two narrow emissions discriminate the 0.67 and 0.60 eV peaks[75,133]. The difference may be due to the fact that the background electron concentration of these measured samples in this study is relatively high, and increases the efficiency of electron-electron scattering[168]. This implies the radiative recombination process is presumably away from Brillouin zone centre (the Moss-Burstein-induced) and increases the magnitude of the FWHM[100].

Not all doped samples exhibit multiple luminescence features, but similar to what is often observed with n-InN[76,91], the many measured PL spectra in this study consist of a broad single peak. As the Mg concentration is increased, a sudden shift of the emission energy can be seen and may be connected to some fashion by either the polarity inversions or the carrier concentration (or Mg concentration: by assuming the Mg causes the introduction of the native defects and compensating donors). PL suggests that the critical value of Mg concentrations for polarity inversions in this series are 3.7×10^{17}, 8.7×10^{17}, and 3.6×10^{19} cm^{-3}, where a KOH wet etching identifies the polarity ‘flips’. At given Mg concentrations, the dominant PL transition shifts either to the red or blue more than 50 meV. The summary of the foregoing discussions are present in table 4.2

To give a quantitative comparison, a Mg doped InN film (GS1810) well characterized by a number of groups, was employed[145,146]. GS1810 was grown by Prof. William Schaff at Cornell University. The Mg concentration of GS1810 is 7×10^{18} cm^{-3} and the crystal polarity is In-face. The PL of GS1810, while previously unreported, exhibits a symmetrical low

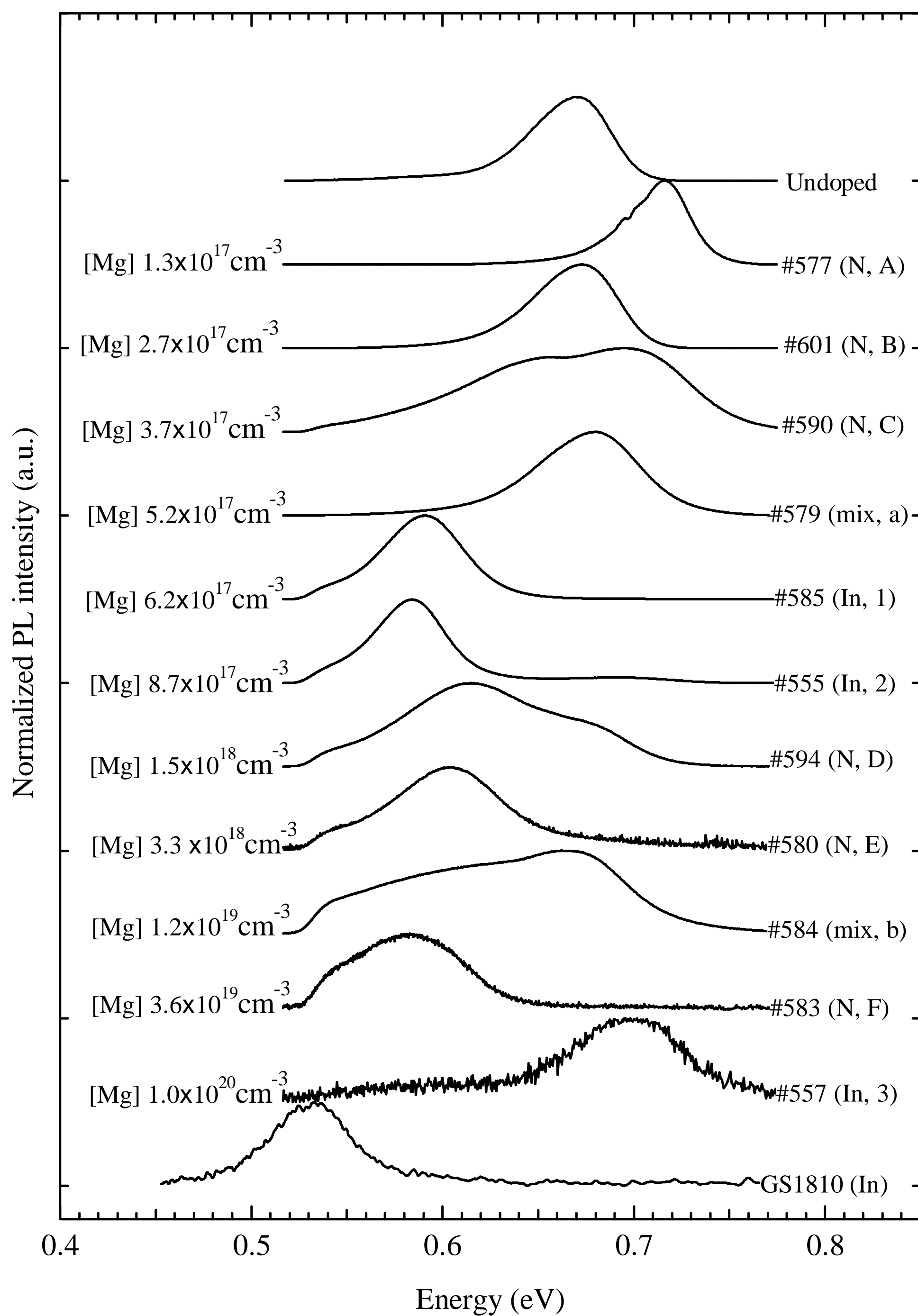

Figure 4.4 4 K PL spectra of N-rich InN:Mg/YSZ. For a reliable comparison GS1810 (Mg doped InN) and undoped InN are included. Parentheses indicate the polarity types and designated labels that identify samples on later figures.

Table 4.2 The polarity inversions and PL energy shifts.

Sample #	Mg Conc. (cm^{-3})	Polarity inversion	Energy shift
#590 → #585	$3.7\times10^{17} \rightarrow 6.2\times10^{17}$	N → In	0.72 eV → 0.59 eV
#555 → #594	$8.7\times10^{17} \rightarrow 1.5\times10^{18}$	In → N	0.58 eV → 0.63 eV
#583 → #557	$3.6\times10^{19} \rightarrow 1.0\times10^{20}$	N → In	0.59 eV → 0.70 eV

energy peak. This feature is likely associated with Mg forming an acceptor, as the thermopower measurement returns a positive Seebeck coefficient and postulates a p-type bulk layer[146].

Before proceeding with a quantitative analysis of the data shown in the following figures, these samples have been designated by alphabetical or numerical labels (for clarity). The PL peak position for each sample was extracted from the spectrum and is displayed in figure 4.5 as a function of the SFH carrier concentration. As the carrier concentration is increased, the emission centre considerably shifts to higher energy, following the Moss-Burstein[29,51] relation in equation 3.12.

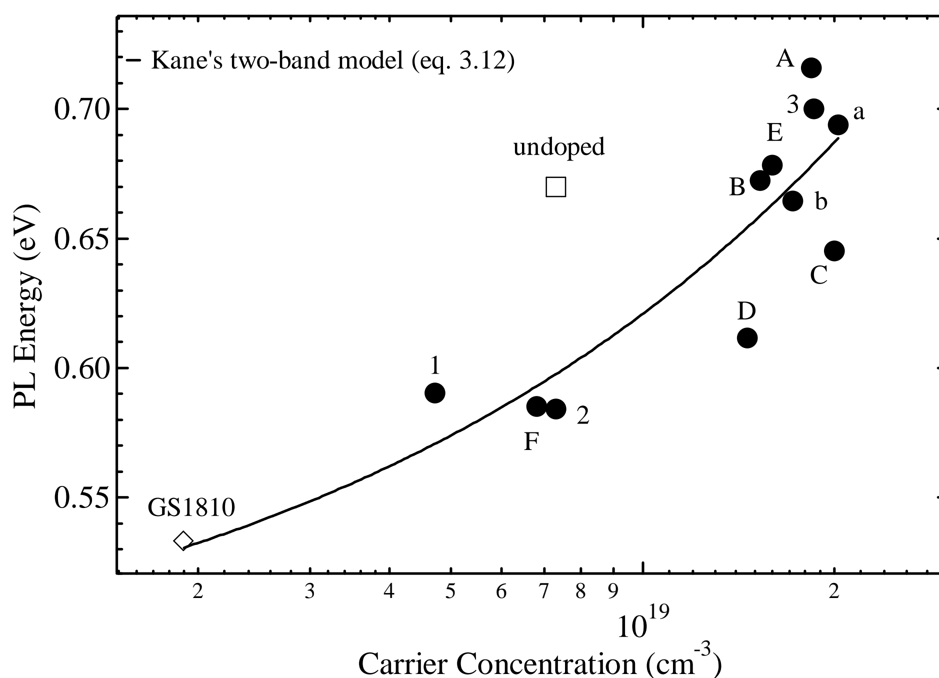

Figure 4.5 PL peak positions of N-rich InN:Mg/YSZ as a function of carrier concentration. The solid line represents the Kane's two band model (eq. 3.12)

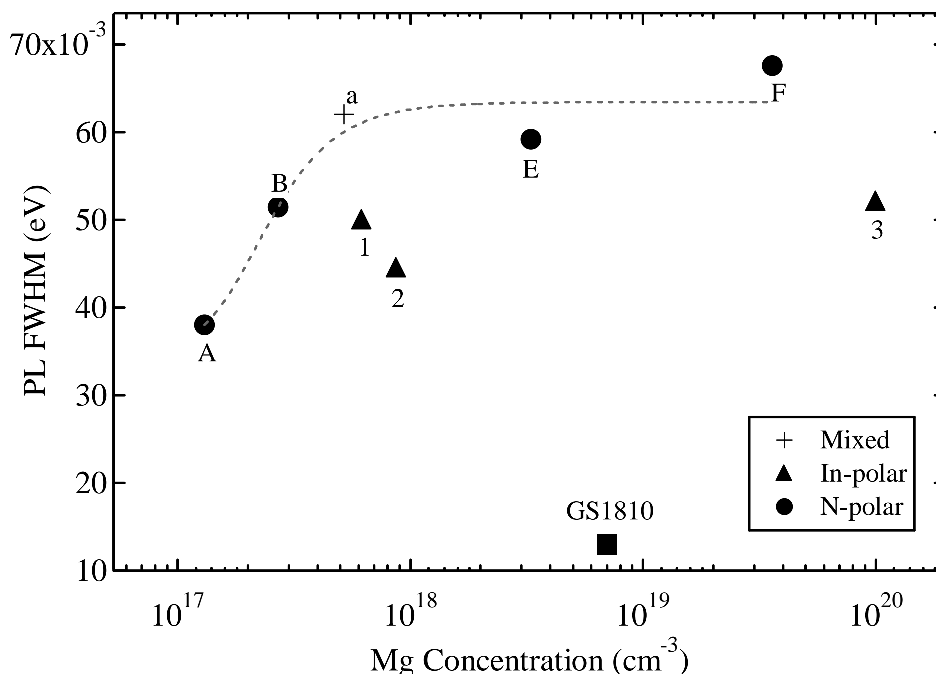

Figure 4.6 FWHM of N-rich InN:Mg/YSZ as a function of Mg concentration. The dotted line is for guidance of the eye for the characterisation of N-polar films.

Also observed was that, PL of samples with both N- and In polarities exhibit a strong variation in FWHM with Mg content as shown in figure 4.6. The PL line shape of both N- and In-polar films broadens with increased Mg doping level (the FWHM of the multiple overlapping components has not been considered in this analysis). Particularly, this trend is readily recognized for N-polar films. This broadening effect indicates the specific doping arrangement with the Mg concentration in some extent. For instance, the interstitial In or the complex induced incorporation (in heavily doped films) can give a rise to the background electron concentration, generating a greater amplitude of many particle interactions (scattering effect) and thus the PL line broadens[168].

Extracted FWHMs from the In polarities are narrower than those from N-rich owing to the smaller values of carrier concentration. One possible interpretation is that the influence of a surface electron accumulation layer in InN may be changed by the polarity type. The FWHM of GS1810 is considerably lower than a series of N-rich InN:Mg/YSZ. This further confirms that the Mg concentration of GS1810 has successfully compensated the background electron concentration and promotes p-type.

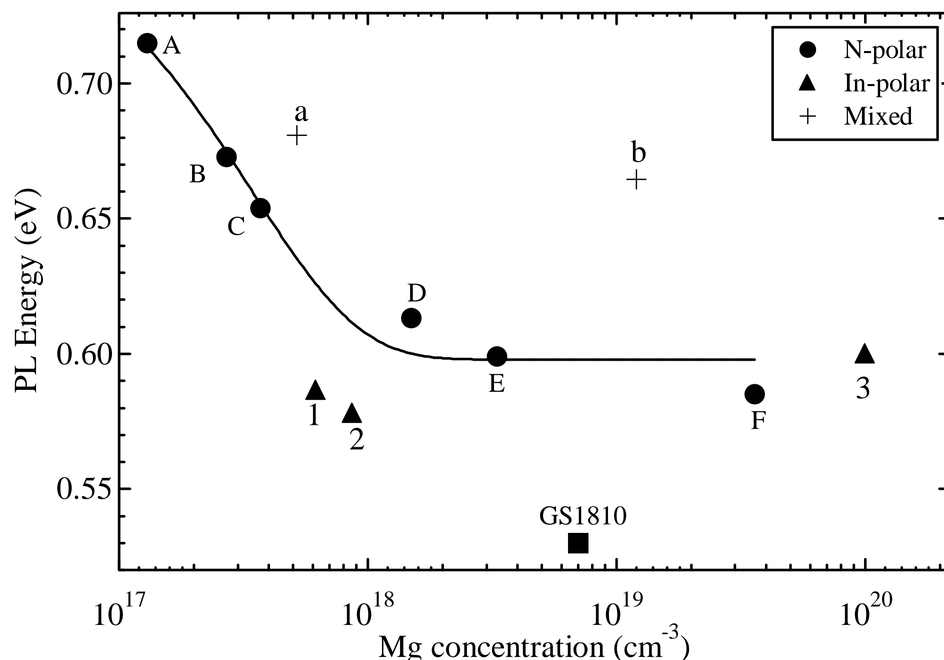

Figure 4.7 The energies of a free-to-bound (or a DAP) transition in various polarity of InN:Mg/YSZ as a function of Mg concentration. The solid line is for guidance of the eye for the characterisation of N-polar films.

The PL peak position for each sample was extracted from the spectrum and is shown in figure 4.7 as a function of the Mg concentration as determined from SIMS. Mg doping of InN results in a gradual redshift in the peak energy until a threshold Mg concentration is reached. This behaviour, while newly discovered in InN:Mg, was already observed in Ga-V semiconductors with 'heavy' p-type doping concentration[223,224]. This phenomenon can result from two possible mechanisms.

First is the shrinkage of the effective bandgap due to the bandgap renormalization (BGR)[100-103,153]. BGR is a result of the Coulomb interaction between an increased number of defects due to the overdoping which decreases the gap between the CBM and VMB[100,102,103]. For this to be feasible, the given material's bandgap must be narrow[103,162]. Second is the alternative formation of neutral bound states[222-224]. By increasing the doping concentration, the amplitude of the potential fluctuations of electrons and holes increase and shift neutral bound states towards a deeper level as discussed in section 3.3. This mechanism is often observed with a donor-acceptor pair transition. A mixture of the BGR and the alternative formation of states is also a possible interpretation.

Figure 4.8 summarizes the influence of Mg acceptors on the integrated PL intensity. As is commonly reported elsewhere[75,133], the PL quantum efficiency is markedly quenched as the

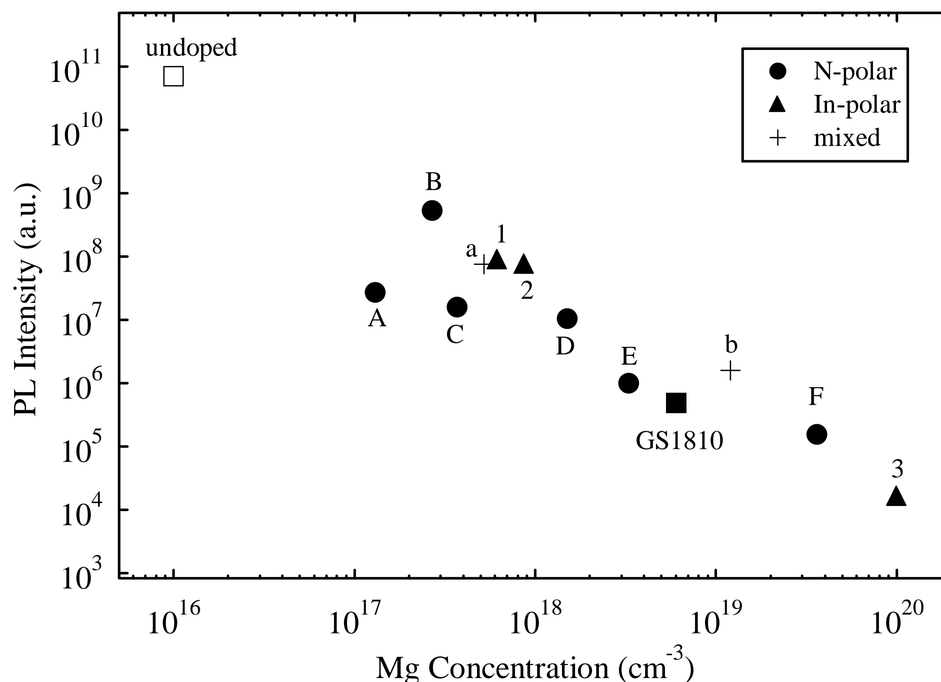

Figure 4.8 Variation of the PL intensity of N-rich InN:Mg/YSZ with different Mg content.

doping concentration is increased. Also reported was the restoration of PL intensity from the completely quenched signal at the highest doping level. This re-appearance to the PL intensity is attributed to Mg overdoping, introducing the donor complexes. A number of studies have been conducted on irradiation with 2 MeV He^+ ions in order to compensate hole acceptors in p-InN:Mg (initially no PL) and restores the PL signal[132,150] [Appendix C]

Meanwhile, the continuous reduction of intensity through the entire Mg concentration range in this series is observed. Our results also conclude that the polarity type has a negligible effect on quantum efficiency. Instead, the observation of a step between the film 'E' and 'b' at the Mg concentration range of 3.3×10^{18} to 1.2×10^{19} cm^{-3} may be explained by a change in the conductivity from n- to p-type, where the PL intensity of GS1810 intimately matches the series. In fact, the potential "p-type window" discussed in the literature is in agreement with a given Mg concentration range[75,76,136].

As highlighted in section 3.3, midgap states possess the most effective non-radiative recombination centres, the so called Shockley-Read-Hall (SRH). SRH is closely linked to the Auger process, which is the likely reason for an insufficient PL intensity inside the heavily

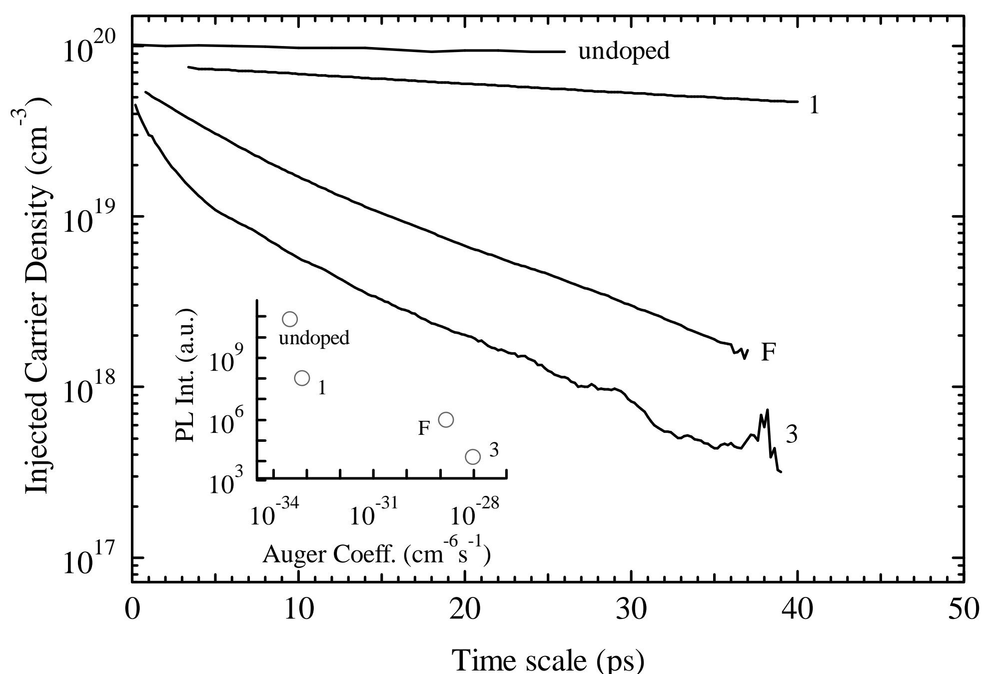

Figure 4.9 The decay of the photogenerated carrier density according to TRDT measurement of selected samples at an injection density of 7.5×10^{19} cm^{-3} per pulse. The inset shows the relationship between the internal quantum efficiency and the Auger coefficient.

doped region. Lifetime measurements are considered to resolve the physical origin of the quenching effect. This type of measurement not only provides the clear view regarding the recombination dynamic but it also returns the useful parameters like Auger and SRH coefficients.

To get a qualitative understanding of the PL quenching, the decay of photogenerated carrier density was undertaken by time-resolved differential transmission (TRDT) and is displayed in figure 4.9. This was performed at room temperature using a pump-probe technique on three separate samples with doping densities of 6.2×10^{17} cm^{-3} (1), 3.6×10^{19} cm^{-3} (F) and 1.0×10^{20} cm^{-3} (3). Undoped InN film has also been included as a reference. For a film with moderate doping level (1), the decay shows a single exponential characteristic, as a usual case for a single SRH recombination and an extracted Auger coefficient of 7.33×10^{-34} $cm^{-6}s^{-1}$ coincides well a reported n-type InN value elsewhere[16]. Meanwhile, both samples F and 3 were characterized by a bi-exponential characteristic with much faster decay rate and is attributed to the onset of Auger recombination, for which two simultaneous processes including the SRH and Auger recombination are valid[147].

The inset of figure 4.9 summarizes the relationship between the internal quantum efficiency and the Auger coefficient. The reduction of PL intensity with increase in acceptor doping density is strongly correlated to the Auger processes. There is a steady enhancement in the Auger coefficient as the doping concentration is increased. By assuming that the "p-type window" is presumably formed in a Mg content level of $10^{19}cm^{-3}$, the origin of Auger process can readily change its type to Auger-7 (p-type)[87]. However, the consistent drop of quantum efficiency throughout both n- and p-type regimes without any dramatic disorder as a function of Auger coefficient suggests that only a single type of Auger-1 (n-type) likely governs the luminescence quenching. This, coupled with a gradual redshift in the peak energy (alternative formation of neutral bound state) with increasing Mg content, indicates that the observed quenching mechanism is in fact associated with trap-assisted Auger[147]. Our results conclude that Mg doping can strongly affect the recombination process and the Auger process dictates the luminescence quenching effect in Mg-doped InN studies.

4.3 Mg forming a deep acceptor; A buried p-type layer?

For further analysis, the PL spectrum of 590-InN:Mg ('C'., N-polar) with 3.7×10^{17} cm^{-3} Mg concentration was recorded with constant excitation power as a function of temperature, as displayed in figure 4.10. Multiple overlapping components can be seen to contribute to the total PL. Broad peak features between 0.65 and 0.70 eV are labeled as I_{fb} and I_{mh}, respectively.

The I_{fb} peak appears to have a 'C-shaped' temperature dependence of PL peak positions. This unusual trend of the I_{fb} peak presumably involves the thermally excited free electrons transferring to the Moss-Burstein-induced inhomogeneous localized states (the resonant donor states) with increasing temperature[40]. This abnormal behavior was also seen in both n-InN[100] and its alloys[240,241]. Another possible interpretation is the existence of a weaker third emission approximately 20 meV below I_{fb} and overlapping it, which was raised during the multi-peak fitting analyses. A forcibly added Gaussian peak, certainly improves the Chi square value by a margin but is very difficult to establish the existence of a third feature, since the analyses deal with such a broad component. If the hidden feature is truly present, it most likely explains the peak shift in terms of temperature. Meanwhile, the I_{mh} peak centre

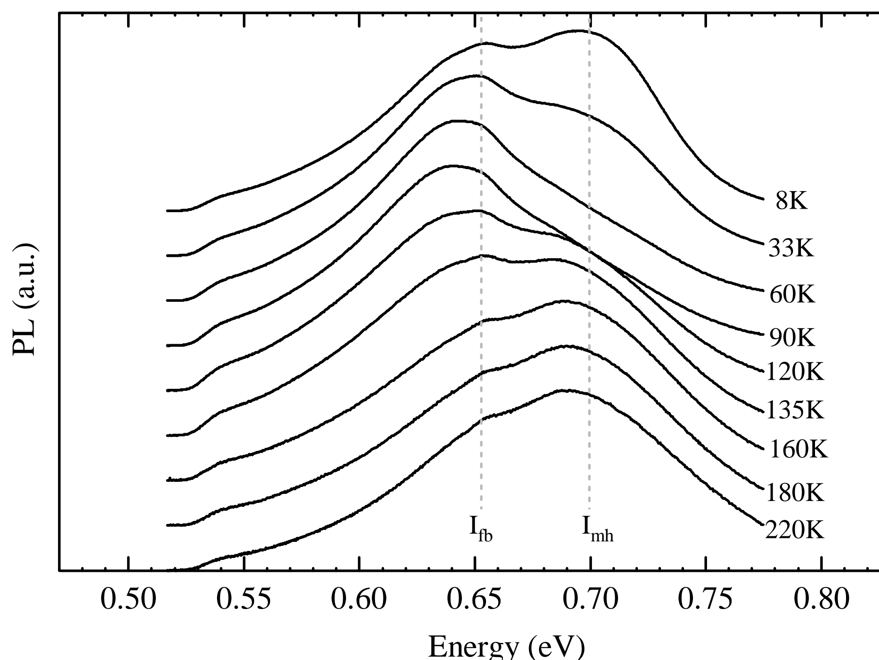

Figure 4.10 PL spectra of sample 590-InN:Mg/YSZ (Mg_{conc}: 3.7×10^{17} cm^{-3}) as a function of temperature (The features are normalized and offset vertically for clarity).

from 8 K to room temperature also redshifts, although a small amount. This suggests that the originating state for PL may not be correlated with the CBM but possibly with some type of localized states above the bandgap such as the Fermi level which possess a large spread in the momentum space $k\neq0$ [214].

The change in PL intensity with increasing temperature follows an Arrhenius type decay curve. However, the experimental results fit rather poorly with one activation energy only. Thus, a better approach is to modify with an additional non-radiative channel in the process, concerning the thermal dissociation of trapped carriers. This also can cause the small intensity drop at the low temperature region[242] as discussed in section 3.6. These activation energies of E_a and E_b represent the non-radiative recombination channel of acceptor state and the thermal hole delocalization energy, respectively. The latter process likely demonstrates the very low activation energy as it requires less energy[93, 242].

The empty square data fit in figure 4.11 describes the decaying process for I_{fb} near 0.65 eV. This transition is governed by activation energies of 48 and 5 meV for E_a and E_b, respectively. The deduced activation energy E_a coincides well with the activation energies reported for Mg in InN involving the Mg_{In} (substitutional Mg on In sites)[75,92,133,216]. This activation energy

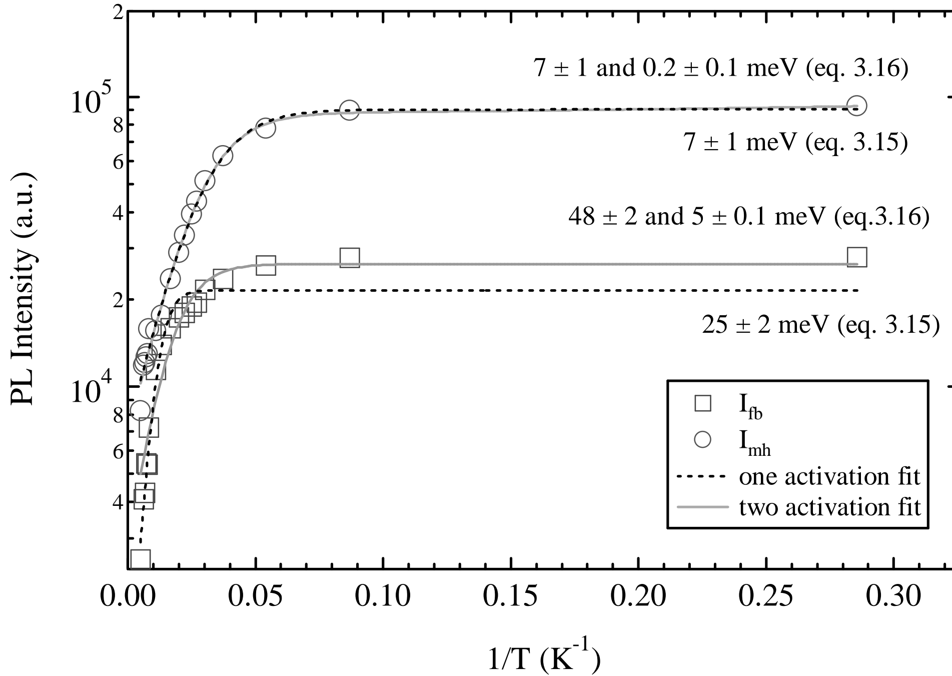

Figure 4.11 The Arrhenius plots of the absolute peak intensities for I_{fb} and I_{mh} (offset for clarity).

concludes that a potential Mg acceptor level is located 48 meV above the VBM, although the energy separation of this acceptor level from the VBM as evidenced from PL is only in a range of 10 and 20 meV. This result suggests a strong onset of the Moss-Burstein effect[29].

Typical Arrhenius behaviour of I_{mh} is also shown in figure 4.11. Despite the absence of a second parameter, the empirical relation shows good agreement with the data and yields an activation energy of 7 meV. This value coincides well with the reported shallow acceptor level in n-InN[90,91]. There was no discernible improvement in neither the Chi square nor the activation energy values when a second activation energy was added to the fit. Perhaps, the non-radiative recombination channel is close enough to the VBM that a thermal dissociation rate is minimal. The difference between the activation energies of I_{fb} and I_{mh} is 41 meV, which accurately describes the energy separation extracted from PL. Worth noting is that I_{fb} and I_{mh} features have comparable intensity at 19 and 135 K. The rapid decrease in the I_{mh} peak with temperature suggests a large distribution of carriers from the shallow acceptor states (of I_{mh}) thermally excited to the deep acceptor states (of I_{fb})[90].

The origin of high energy emission above the bandgap has always been the subject of controversy. A possible explanation of I_{mh} is that the 0.7 eV peak arises from transitions of free electrons at the Fermi level (the Fermi edge) above CBM to a shallow bound state, the so

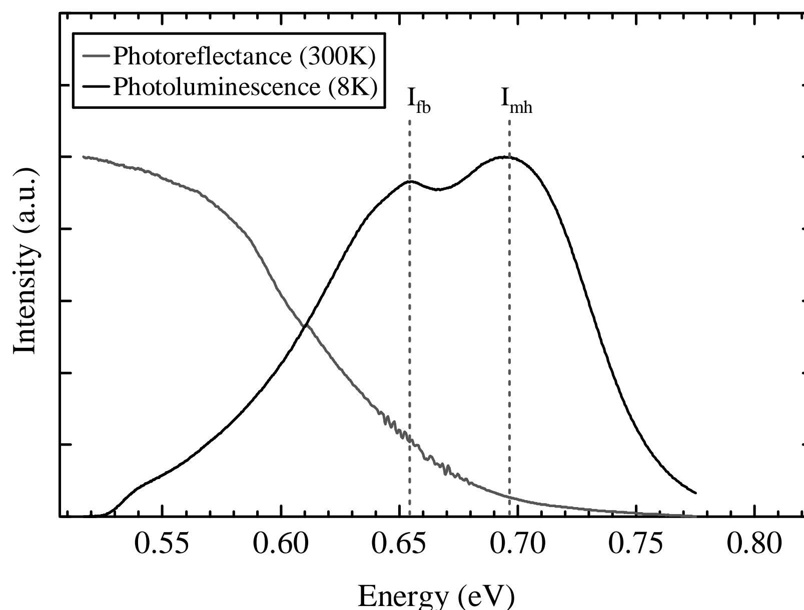

Figure 4.12 A low temperature (8K) PL and room temperature photo-reflectivity spectra.

called Mahan exciton[118]. This view is additionally supported by 1) the observed transition far above the bandgap of 0.67 eV, and 2) the noticeable line broadening effect with temperature in figure 4.10. The electron-hole scattering rate as a function of temperature is very effective at the Fermi edge, which causes a strong FWHM variation upon the temperature[100]. The Fermi energy is determined by the photo-reflectivity (PR) spectra, where its onset should directly point to the Fermi level. The excitation source was a tungsten coiled quartz iodine lamp and the angle of the incident light was approximately 45° from normal. As shown in figure 4.12, the PR onset is in vicinity of the I_{mh}, but has a slight offset because of the difference in surrounding temperatures of two measurements. The spacing of 41 meV between I_{fb} and I_{mh} is also consistent with a report elsewhere[100].

In order to more solidly identify the origin of the observed peaks, the detailed PL spectrum of 590-InN:Mg was recorded in figure 4.13 as a function of excitation intensity. As discussed in section 3.8, the PL emission intensity can be characterized by a power law $I \sim L^k$. The extracted exponent k (a slope of log-log plot) dictates to a recombination process and the physics behind has been thoroughly explained elsewhere[113,255]. Theoretical treatment reveals $k = 2$ (quadratic; a single injected excitation returns two emitting photons) for a band-to-band transition, $1 < k < 2$ (super-linear; at least a photon is emitted as a result of the 'returned to equilibrium' process) for an excitonic transition, and $k < 1$ (sub-linear; the effective trap centres induce a combined emission involving both a photon and phonon) for a defect related

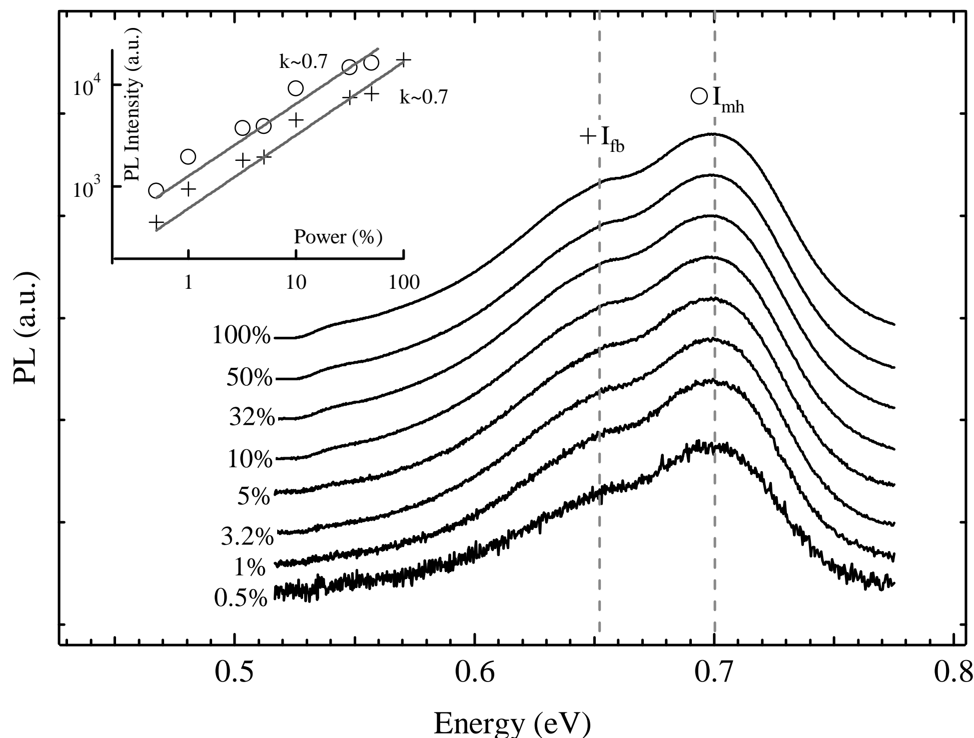

Figure 4.13 PL spectra of sample 590-InN:Mg/YSZ (Mg_{conc}: 3.7×10^{17} cm^{-3}) as a function of excitation power (The features are normalized and offset vertically for clarity). The inset shows the log slope of two different components by using a power law equation.

transition.

Both the I_{fb} and I_{mh} follow an $I \sim L^k$ relationship. The sub-linear power dependence from both I_{fb} and I_{mh} can be regarded as impurity related transitions[113]. In sharp contrast to the temperature dependent PL analyses, the intensity depletion rates of the two components are equivalent throughout the various excitation ranges. Arnaudov *et al.*[91] quoted that if the number of photons created by the excitation (intensity) is higher than the background electron concentration (or the density of occupied states above the CBM), a significant band filling is expected and thus peak shifts to higher energy can be observed. Both the I_{fb} and I_{mh} peaks however, do not show such shifts. Since the SFH carrier concentration of this film is very high, the expected blueshift of I_{fb} and I_{mh} peaks are likely swamped by a highly distributed degenerate electron population above the CBM. Further work is required to clarify the precise physical origin of Mg participating in the observed deep acceptor transition. Without determining quantitative bulk properties such as by variable magnetic field Hall effect (VFH), it is not possible to ascertain whether any compensation due to Mg acting as an acceptor is occurring.

4.4 Donor-acceptor pair transition; The metamorphosis of a Mg state

Figure 4.14 shows the temperature dependent PL of 555-InN:Mg (‘2’., In-polar) with 8.7×10^{17} cm^{-3} Mg concentration. Although, the doping density of this film is just a step above the 590-InN:Mg (‘C’., N-polar), the PL characteristic is somewhat different. A single asymmetric emission is centred at 0.6 eV, and a shadowy component is located 70 meV below. The lower energy feature is only apparent in the low temperature regime. This emission is shifted toward lower energy by the LO-phonon energy of 72 meV and it is a result of the electron (carrier)-phonon interaction (a phonon-replica of dominant peak)[90,91].

The efficiency of luminescence and the value of the activation energy have been determined by the Arrhenius plot in figure 4.15. This assignment is based on a single activation fit. The high temperature data is weighted with the reciprocal of the intensity for the initial fit to accurately determine the activation energy and can yield reasonable fits to the data. The variation of absolute PL intensity as a function of temperature gives an activation energy of 37 meV, which disagrees with the reported activation energies for Mg or for residual acceptors in InN[75,92,133,216] as discussed in section 3.7. This ambiguous activation energy value naturally points to a different type of transition such as a donor-acceptor pair transition (DAP)[152]. This explanation is preferred over other possibilities due to its low PL energy just below 0.6 eV.

In order to draw a clearer picture, the empirical Arrhenius formula has been adjusted (from equation 3.16) by taking account of a shallow donor bound state.

$$I(T) = \frac{I(0)}{1+A\exp\left(\frac{-E_{A1}}{k_BT}\right)+B\exp\left(\frac{-E_D}{k_BT}\right)+C\exp\left(\frac{-E_{A2}}{k_BT}\right)} \tag{4.1}$$

Here E_{A1} and E_{A2} represents the activation energies for a neutral acceptor bound state for the high and low temperature regions as discussed in section 3.7. E_D is the localization energy of a shallow donor state involving the formation of a non-radiative channel with respect to the CBM[148]. This equation assumes the activation energy of E_D is larger than E_{A2}.

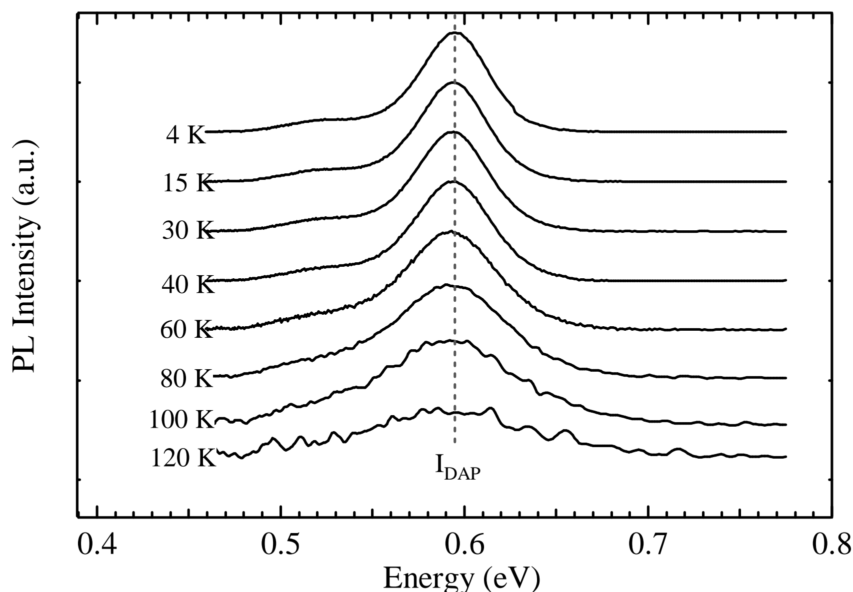

Figure 4.14 PL spectra of sample 555-InN:Mg/YSZ (Mg_{conc}: 8.7×10^{17} cm^{-3}) as a function of temperature (The features are offset vertically for clarity).

A revised least square fit using equation 4.1 has been made and the fitting result of a Chi square (χ^2) value was somewhat improved[111]. The analysis yields activation energies of acceptor states of 37 and 5 meV for E_{A1} and E_{A2} respectively, while the activation energy of a donor state is 10 meV. The I_{DAP} involves a shallow donor level at 10 meV below the CBM, which is in good agreement with the reported hydrogenic donor activation energy of 6 - 12 meV in both InN and GaN[135,230,235,236].

Meanwhile, a deep acceptor state lays 37 meV above the VBM and the rather low value of activation energy draws the conclusion that this acceptor is not correlated with Mg incorporation (48 - 110 meV). This view also strongly suggests that the Mg is not easily incorporating in the desired substitute In sites (Mg_{In}). Comparison between the activation energies of deep acceptor states taken from samples 590-InN:Mg/YSZ (E_A: 48 meV) and 555-InN:Mg/YSZ (E_A: 37 meV) suggests that the Coulomb interaction between a large number of ionized acceptors and holes in the VBM effectively weakens the strength of the non-radiative channel[221]. This results in a reduction of the activation energy of a deep acceptor state for the sample 555-InN:Mg/YSZ, although its PL peak position is lower than the sample 590-InN:Mg/YSZ.

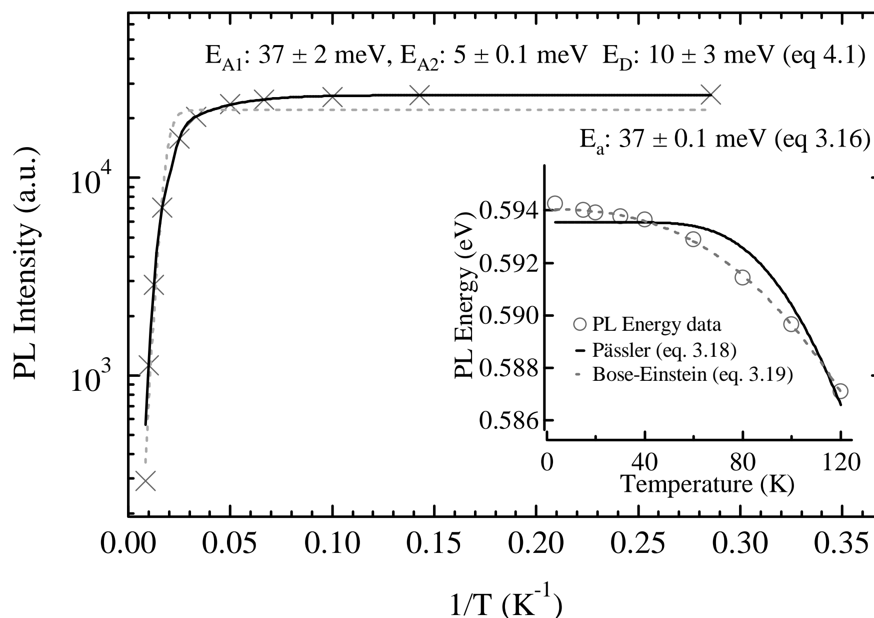

Figure 4.15 The Arrhenius plots of the absolute peak intensities for I_{DAP}. The inset exhibits the Pässler and Bose-Einstein plots of the variation of I_{DAP} emission centres as a function of temperature.

Least square fits of the Bose-Einstein (equation 3.19) and the Pässler (equation 3.18) are shown in the inset of figure 4.15. The 0.60 eV peak redshifts as a function of temperature as it follows the bandgap shrinkage. The theoretical treatment using the Bose-Einstein estimates the bandgap shrinkage between liquid helium and room temperature as roughly 25 meV. This value is not consistent with the reported bandgap shrinkage values of 55-60 meV for the free-to-acceptor levels[90]. This may be attributed to the thermally ionized donor electrons being transferred to the conduction band at the low temperature region (the thermal energy greater than 10 meV). The details of fitted parameters have already been covered in section 3.7.

Figure 4.16 shows the excitation intensity dependent PL of film 555-InN:Mg (2). The 0.60 eV peak exhibits a distinguishable blueshift as a function of excitation intensity owing to the electrostatic Coulomb interaction as discussed section 3.3. This, coupled with a sub-linear power dependent as shown in the inset of figure 4.16 further confirms that the originating states for PL is correlated with the DAP. Our results conclude that either the H^+ forms a shallow neutral donor bound states (Mg-H complex) as is often the case for GaN:Mg[129,130,221] or the occupation of interstitial sites (native point defects) act exclusively as donor. The latter can give an Indium-Frenkel pairs, which can be thought as a DAP[231-233].

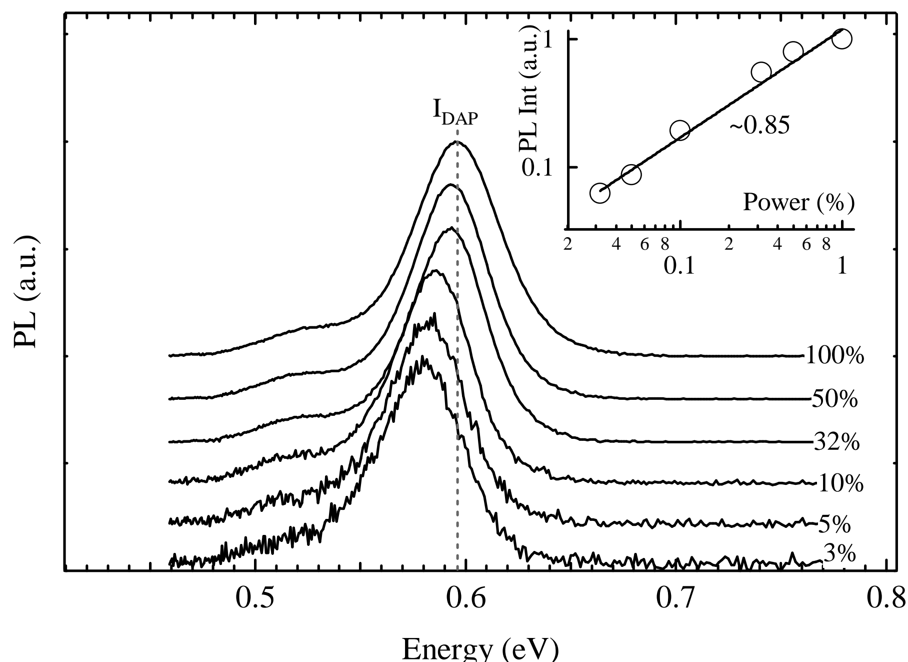

Figure 4.16 PL spectra of sample 555-InN:Mg/YSZ (Mg_{conc}: 8.7×10^{17} cm^{-3}) as a function of excitation power (The features are normalized and offset vertically for clarity). The inset shows the log slope of main component (I_{DAP}) by using power law equation.

4.5 Brief summary

Figure 4.17 illustrates the activation energy and power-law coefficient values of N-rich InN:Mg/YSZ as a function of Mg concentration. A sequence of acceptor formation upon Mg content is the underlying mechanism. In PL, an initial stage of recombination is a degenerate free electron-to-shallow acceptor. As the doping density increases, the shallow bound state moves deeper into the gap from the VBM due to a mixed procedure of the bandgap renormalization (BGR) and the potential fluctuation of localized states. When the Mg concentration reaches 3.7×10^{17} cm^{-3}, a low energy PL feature is 'potentially' correlated to Mg forming a deep acceptor. The extracted activation energy is 48 meV, which matches well with reported Mg activation energies in InN[75,92,133,216].

The dominant PL peak continuously shifts to the red until a threshold Mg concentration is reached, although the formation probability of a deep acceptor is significantly lowered, which corresponds to the extracted activation energy being reduced. Simultaneously, a donor level is

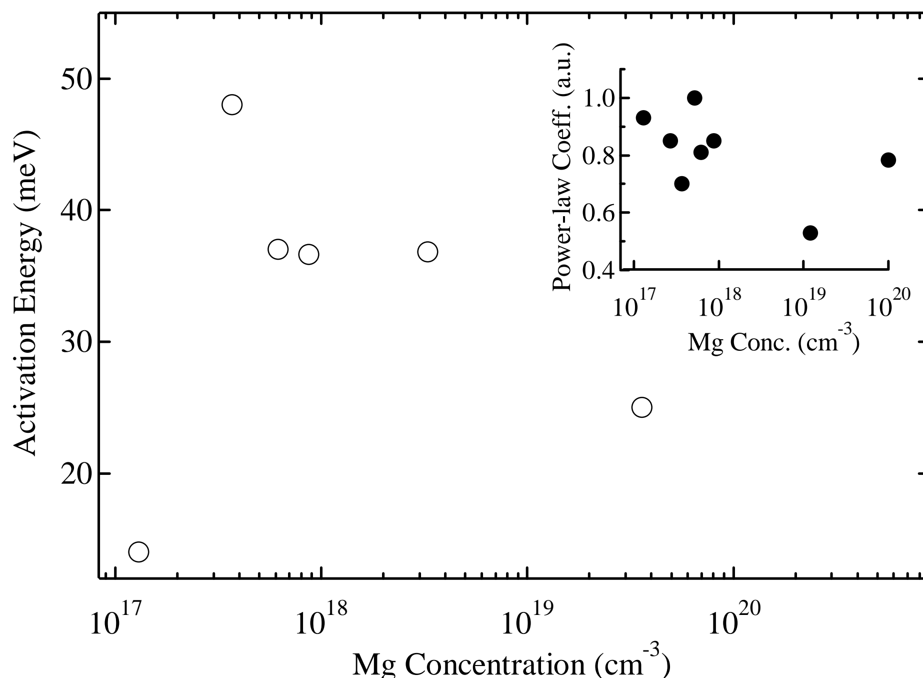

Figure 4.17 The optical properties from a series of InN:Mg/YSZ films from temperature and excitation intensity (inset) dependent PL analyses as a function of Mg concentration.

configured at approximately 10 meV below the CBM and a DAP recombination draws the total PL.

A change in the recombination path from the deep acceptor to DAP transition with increasing Mg content, is also reported in studies of PL in GaN:Mg[221,243]. The physical origin of the donors participating in the observed DAP transition is likely the H^+ (Mg-H complex) or In interstitial as discussed elsewhere[92,133,236]. By increasing the doping, the amplitude of the potential fluctuations of donor and acceptor sites increases, and results in a shift of these bands to lower energy[222-224], although the Coulomb potential between a large number of ionized acceptors and holes in the VBM significantly reduces the formation of neutral acceptor bound states as evidenced from a decreased activation energy value[221]. Worth noting is that all of DAP transitions observed in this series involve the apparent phonon replica below LO-phonon energy of 72 meV, regardless of their polarity.

A pronounced PL blueshift effect is observed from the DAP transition as a function of excitation intensity. This effect is attributed to the Coulomb interaction between donors and acceptors. The expected Moss-Burstein induced blueshift of a deep or shallow acceptor

Table 4.3 The list of transition detail and extracted luminescence parameters.

N-rich Film #	Polarity	T_{Mg} (°C)	Mg_{conc} (cm^{-3})	Trans. Energy	Trans. Type
577-InN:Mg., A	N	200	1.3×10^{17}	0.72 eV	$I_{eA°\,(shallow)}$
601-InN:Mg., B	N	208	2.7×10^{17}	0.67 eV	$I_{eA°\,(shallow)}$
590-InN:Mg., C	N	220	3.7×10^{17}	$\underline{0.65\ \text{eV}}$	$I_{eA°\,(Mg)}$
579-InN:Mg., a	Mix	170	3.3×10^{18}	0.6 eV	$I_{eA°\,(shallow)}$
585-InN:Mg., 1	In	216	3.6×10^{19}	0.58 eV	I_{DAP}^{LO}
555-InN:Mg., 2	In	225	6.2×10^{17}	0.59 eV	I_{DAP}^{LO}
580-InN:Mg., E	N	240	8.7×10^{17}	0.58 eV	I_{DAP}^{LO}
583-InN:Mg., F	N	276	1.0×10^{20}	0.71 eV	I_{DAP}^{LO}
557-InN:Mg., 3	In	300	5.2×10^{17}	0.67 eV	$I_{eA°\,(shallow)}$

Note: 1. An underline signifies a Mg forming a deep acceptor.

2. LO → A LO replica is also observed.

emission is rather swamped by the high carrier concentration of the films[91]. These views were the key evidence to convincingly discriminate the transitions between a free-to-deep acceptor and DAP in this study. As shown in the inset of figure 4.17, the power-law exponent being a sub-linear characteristic also parallels the preliminary peak assignments. The unique linear relation from sample 579-InN:Mg is obtained from the least square fit of the power-law, but its uncertainty is large enough to allow for two distinct relations. Since this film has high electron background concentration, the presence of an excitonic feature is very doubtful. Detail of the observed luminescence transitions of N-rich InN:Mg/YSZ are listed in table 4.3.

Chapter 5

Indium-rich Magnesium doped Indium Nitride

With the maturation of MBE film growth technology, the important role of In/N ratio is also realized and is considered as the key parameter to achieve a good crystal quality of InN[117]. Recent investigations of the In-rich growth regime have triggered a better fundamental understanding of Mg doped InN and have become a preference for p-InN study[75,117,155]. In-rich growth gives an In-face surface polarity, and this condition is known to reduce the effect of the threading dislocation[155]. Also reported was the smooth surface morphology of InN:Mg surface indicating high quality epilayers[134,155,156]. A combination of these circumstances naturally returned a plentiful Mg incorporation comparing to the N-rich growth and also a catalogue of electrical and optical properties was in an advanced form. In fact, the Ga-rich condition is also more functional regarding dopant incorporation in GaN, favouring a substitutional arrangement on the Ga site[157,172,173].

5.1 The growth parameters and electrical properties

Growth, SEM, and SFH by Dr. Jessica Cha, at University of Canterbury

SIMS and XPS by Mr. Wojtek Linhart, at University of Warwick

VFH by Prof. Thomas Myer, at Texas State University

It is worthwhile to explore In-rich Mg doped InN. A series of In-rich InN:Mg epilayers were investigated via systematic studies into the relative performance of different flux conditions and the introduction of a buffer layer. Aforementioned, the best InN (or InN:Mg) films grown to date use GaN buffer layers on top of sapphire substrates[145,146]. This has provided a reliable comparison to the former series of N-rich InN:Mg/YSZ. The growth morphology was carried out in a similar manner to the former series in chapter 4 and more details are given in Appendix A.

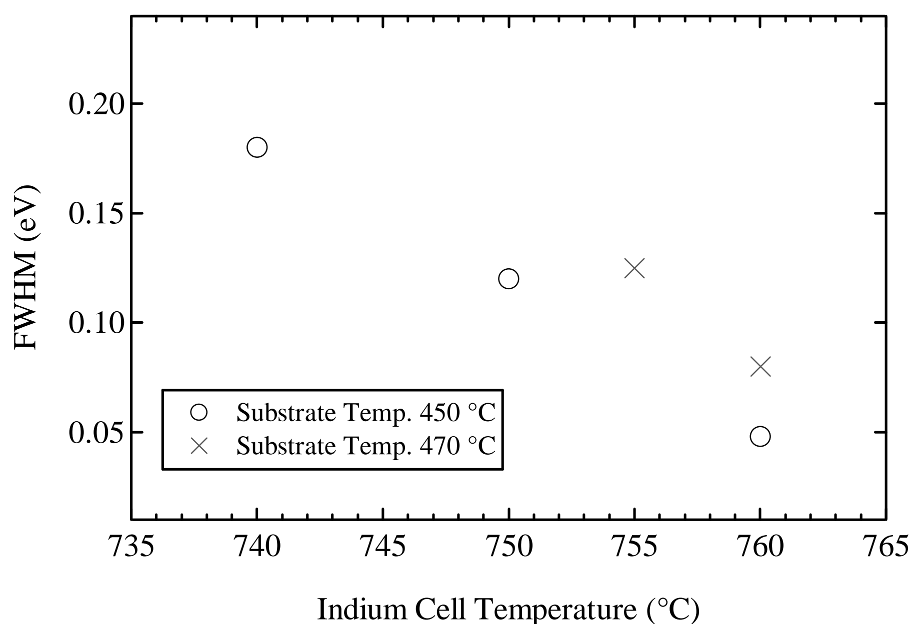

Figure 5.1 FWHM (PL) of trial growth InN/GaN films. The noticeable change of FWHM was observed with different In flux. The lower substrate temperature of 450°C was preferable to produce high quality films.

The standard growth temperature of 450 °C and N_2 plasma conditions were maintained. The single crystal InN thin films were grown in a cryo-pumped Perkin Elmer 430 MBE system on high-resistivity Ga-polar GaN:Fe/Al_2O_3 templates/substrates and a film thickness was 1.2 μm with growth of three hours. As noted previously, InN suffers greatly from threading dislocations below the 'critical' thickness of 1 μm.

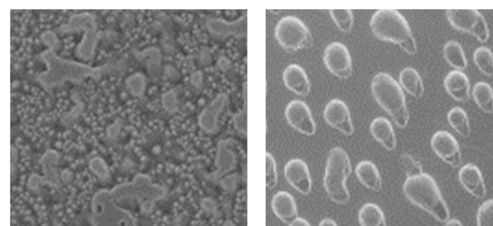

Figure 5.2 SEM images of InN/GaN thin films taken from inner (left., N-rich) and outer part (right., In-rich) of wafer before the chemical etching.

Conventional Knudsen effusion cells were employed to deposit both In and Mg with a chamber pressure at 1×10^{-5} torr. After undergoing some trial runs the choice of In cell and substrate temperatures were set at 760°C and 450°C, respectively. As shown in figure 5.1, a noticeable change of FWHM of PL line was observed with different In flux. The substrate temperature of 450 °C was preferable to produce the high quality InN thin films (*ie*. a low background electron concentration).

Despite the initial purpose of this growth being In-rich InN:Mg, a lateral gradient in the In flux produced an inhomogeneous stoichiometry across the wafers and N-rich zones were

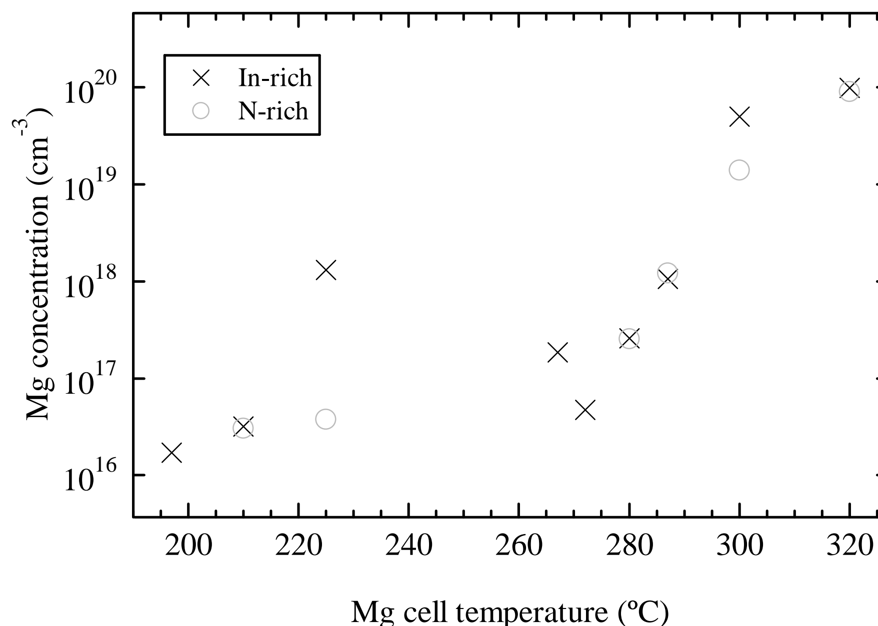

Figure 5.3 SIMS Mg concentration of a InN:Mg/GaN series as a function of Mg deposition source temperature.

partially formed. These unintentional products can be readily recognized by SEM as depicted in figure 5.2. A typical rough surface when N-rich was observed on the inner part of the wafer, whereas the In-rich zone showed a reasonably smooth surface morphology (covered by In droplets). The 2 cc Mg cell temperature (T_{Mg}) was varied from 197 °C to 320 °C. The Mg concentration was determined from SIMS experiments and was found to be within a range of 1.7×10^{16} to 9.81×10^{19} cm^{-3} as shown in figure 5.3. Worth noting is that the determined Mg concentrations were very similar for the both In- and N-rich flux conditions. SIMS Mg concentration taken from the In-rich 712-InN:Mg grown with a Mg cell temperature of 225 °C seems to be overestimated, although the cause of this event is unknown.

SFH measurements extracted the important electrical parameters. As displayed in figure 5.4, both the electron concentration and mobility significantly decrease as a function of Mg cell temperature, regardless of the growth fluxes. The major difference perhaps is that the carrier concentration of samples taken from In-rich initially increases until a threshold Mg cell temperature of 267 °C (corresponding to Mg concentration of 1.84×10^{17} cm^{-3}), although afterwards, there is a steady drop of its value and eventually plateaus at approximately 4×10^{18} cm^{-3}.

If the assumption is that the bulk is successfully compensated at this point, then it is possible that the SFH sees proportionately more of the low mobility surface layer, resulting in a large

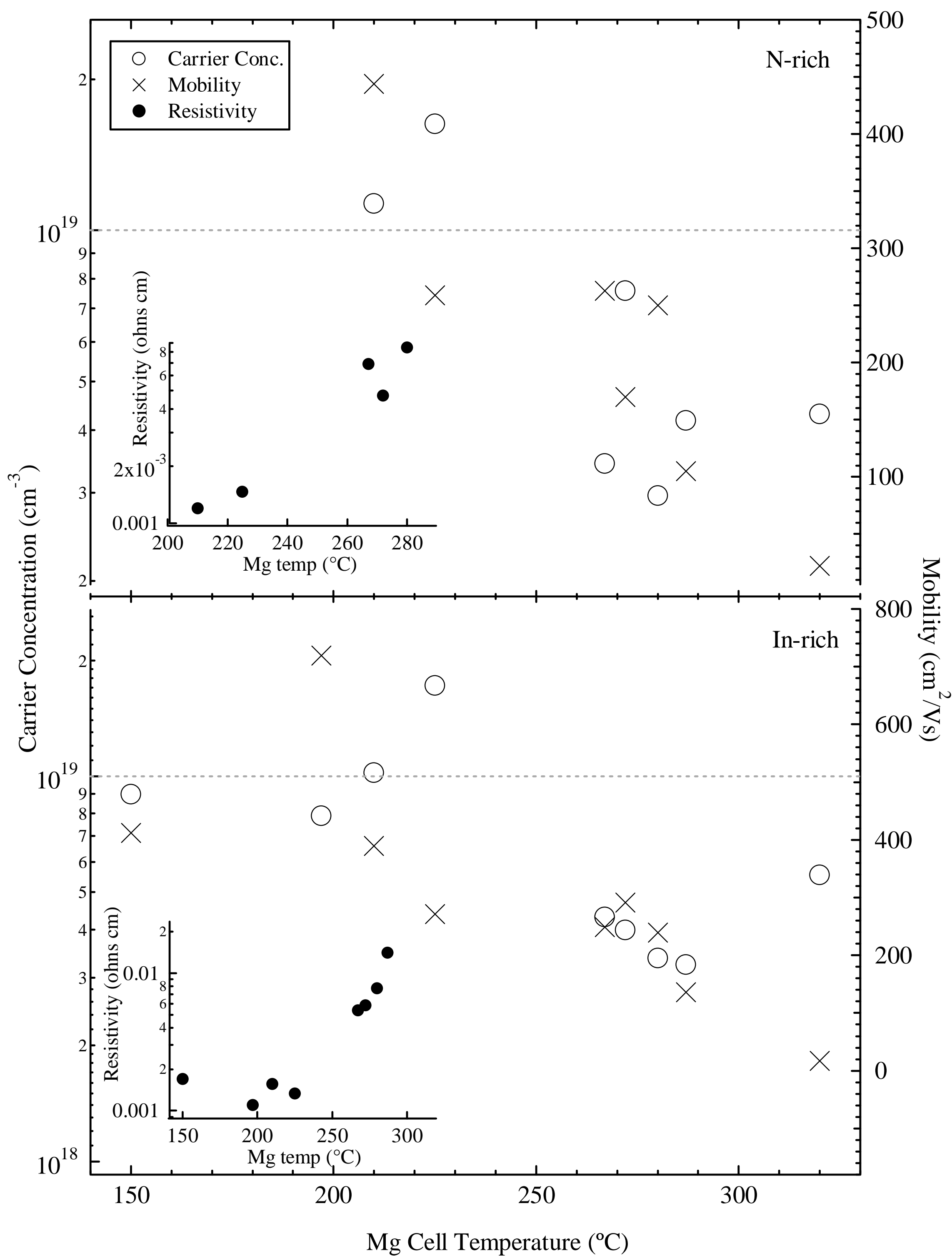

Figure 5.4 SFH electrical properties of a N- and In-rich InN:Mg/GaN series as a function of Mg concentration. The horizontal line indicates the measurements on an undoped InN.

decrease in overall mobility. Correspondingly, the resistivity gradually increases with increasing Mg cell concentration, consistent with the theory of a compensated bulk layer[158,159]. More encouraging SFH results compared to the InN:Mg/YSZ series of chapter 4 appear to be linked to the film thickness (and the use of GaN template). The improvement of the electrical properties is proportional to the film thickness since the surface electron accumulation layer becomes a less concern[142]. More details of this is discussed in Appendix B.

X-ray photoelectron spectroscopy (XPS) measurements revealed the polarity of the InN:Mg/GaN films. XPS measurements were performed at room temperature on a Scienta ESCA300 spectrometer. In prior observations of polarity inversion of In-rich InN:Mg, only a single incident of a polarity flip effect (In- → N-polar) at a high Mg content level of 10^{19} cm^{-3} was reported[134]. The transmission electron microscopy (TEM) image shown in that work captured the accumulated Mg at the surface of InN at the given Mg concentration, although this effect had no influence upon an ever-present electron accumulation layer.

Likewise here, the polarities are thoroughly fixed at In-face until the Mg cell temperature reaches a threshold of 320 °C (corresponding to Mg concentration of 9×10^{19} cm^{-3}), where the polarity flips from In- to N-face. Meanwhile, the polarity of a N-rich InN:Mg/GaN series in this work is permanently fixed at In-face, consistent with a recent study of N-rich InN:Mg[155]. Despite the same N-rich growth, there is a discernible difference in the polarity inversion between the former InN:Mg/YSZ of chapter 4 and this InN:Mg/GaN series. The exact cause of this phenomenon is unknown.

XPS measurements also can serve to extract the estimated Fermi energy (E_F)[245]. As has been a weighty matter for InN, its somewhat unusual position of the E_F has been troublesome for many issues (*ie* degenerate electrons). As displayed in figure 5.5, E_F of lightly doped films (both N-and In-rich) are approximately 1.4 eV above the VBM. When the Mg cell temperature reached 300 °C, the E_F was significantly dragged to a lower energy, although the values of E_F taken from In- and N-rich films have a slight difference. The In-rich condition is determined to have a lower value of the E_F, which is closer to the level of non-degeneracy as discussed in section 3.5. This suggests that those In-rich samples are more efficiently compensating the background electrons, leading towards the realization of p-type and also

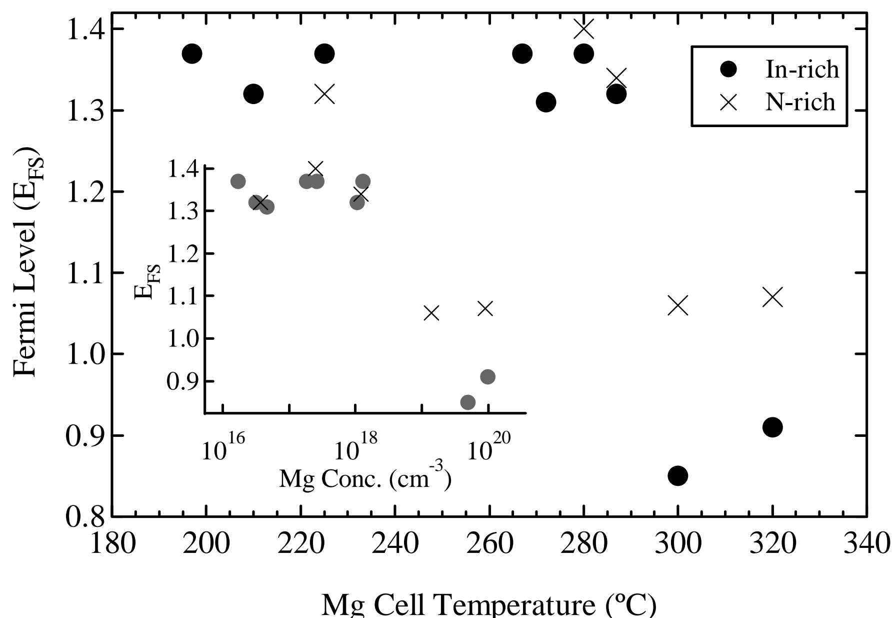

Figure 5.5 Valence band edge XPS data for InN:Mg/GaN films with respect to the surface Fermi level as a function of Mg cell temperature and Mg concentration (inset).

readily proves Mg as an acceptor. It is worth noting that XPS is a surface dependent study. Therefore the extracted Fermi energy may be slightly overestimated by the electron accumulation layer and may disagree with Hall effect measurements. The detailed use and properties of XPS studies in this series is recently published elsewhere[245].

The existence of the ever-present surface electron accumulation layer of InN is problematic for SFH measurements[67,165]. An alternative method for distinguishing a material's 'pure' electrical property is variable magnetic field Hall effect (VFH) measurements [Appendix A]. This technique precisely determines the bulk carrier populations of InN:Mg via examining multiple conducting paths[142,161,166,167]. More details of the experimental techniques used here are mentioned elsewhere[61,161].

Figure 5.6 presents the carrier concentration as calculated using multicarrier fitting to VFH measurement of In-rich InN:Mg films. The distribution of the electrons and holes are rather randomly formed throughout a wide range of Mg content but similar to the SFH measurement, they mostly decrease with increased doping density. A noteworthy sample of 714-InN:Mg (T_{Mg}: 280 °C) has relatively low carrier concentrations of 10^{17} cm^{-3}, which is very close to the non-degeneracy level of mid 10^{16} cm^{-3}. Another eye catcher is 713-InN:Mg (T_{Mg}: 267 °C).

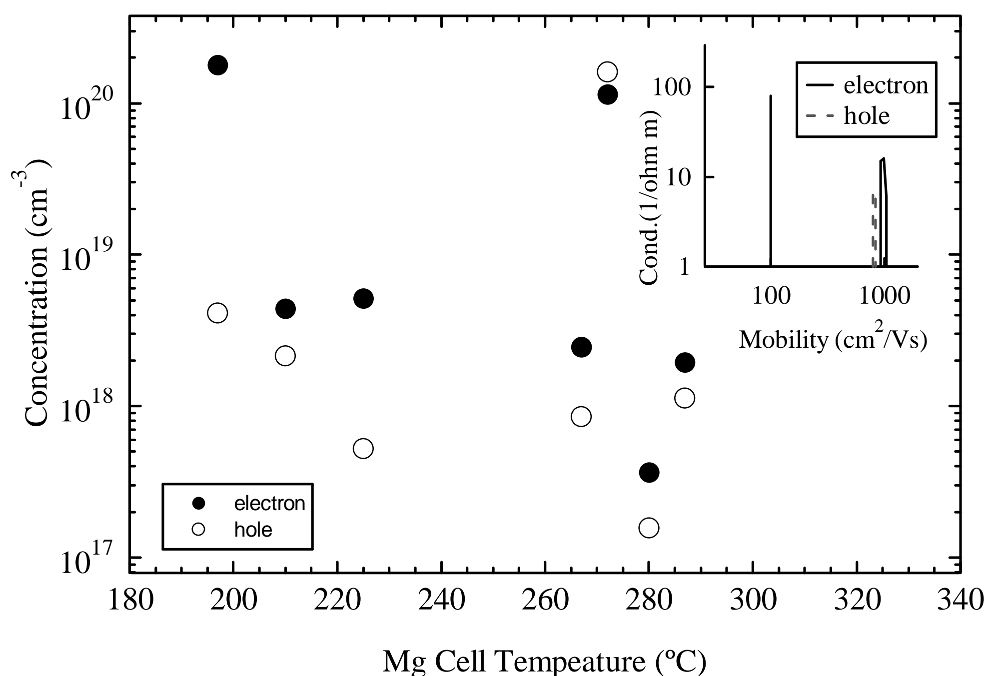

Figure 5.6 Concentration of electron and hole carriers as calculated by VFH measurements as a function of Mg cell temperature. The inset displays QMSA spectrum [Appendix D] of an In-rich InN:Mg/GaN film grown with a Mg cell temperature of 280 °C.

Rarely has the concentration of hole carriers being greater rather than the electron population. Rather large values of both the electron and hole concentrations are also an interesting concept. Their distinctive properties and extraordinary PL observations will be comprehensively discussed in following sections.

Only a limited number of In-rich samples over a Mg cell temperature range of 272 to 287°C yields the direct evidence of a buried p-type layer. In the quantitative mobility spectrum analysis (QMSA) plot in the inset of figure 5.6, the presence of hole populations peaking at 850 cm^2/Vs can be seen. This view strongly implies that Mg has been successfully incorporated in the InN:Mg/GaN film. Meanwhile, the electron population was found in a mobility range of 100 - 1000 cm^2/Vs. The lower value points to the surface electron accumulation layer[142]. Meanwhile, InN:Mg/GaN films grown under N-rich conditions do not show any signs of such an embedded p-type layer, where only electron-mediated features with the bulk layers are measured. This strongly indicates that the growth under N-rich conditions somewhat inhibits the substitutional Mg incorporation (Mg_{In}), which was also the case for a N-rich InN:Mg/YSZ series of chapter 4. Summarized electrical properties are listed in table 5.1.

Table 5.1 A summary of growth conditions and Hall effect measurements (SFH) of Mg doped InN/GaN

In-rich Film #	Polarity	T_{Mg} (°C)	Mg_{conc} (cm^{-3})	μ cm^2/Vs	n (cm^{-3})
706-InN	In	-	-	412	8.99×10^{18}
710-InN:Mg	In	197	1.7×10^{16}	719	7.89×10^{18}
711-InN:Mg	In	210	3.2×10^{16}	389	1.02×10^{19}
712-InN:Mg	In	225	1.31×10^{18}	271	1.72×10^{19}
713-InN:Mg	In	267	1.84×10^{17}	291	3.99×10^{18}
714-InN:Mg	In	280	2.6×10^{17}	239	3.37×10^{18}
715-InN:Mg	In	272	4.7×10^{16}	249	4.31×10^{18}
718-InN:Mg	In	287	1.06×10^{18}	136	3.24×10^{18}
719-InN:Mg	N	320	9.81×10^{19}	17	5.55×10^{18}
722-InN:Mg	-	300	4.99×10^{19}	-	-
N-rich Films #					
711-InN:Mg	In	210	3.0×10^{16}	444	1.13×10^{19}
712-InN:Mg	In	225	3.75×10^{16}	259	1.63×10^{19}
713-InN:Mg	In	272	-	170	7.57×10^{18}
714-InN:Mg	In	280	2.53×10^{17}	250	2.96×10^{18}
715-InN:Mg	In	267	-	263	3.43×10^{18}
718-InN:Mg	In	287	1.22×10^{18}	105	4.18×10^{18}
719-InN:Mg	In	320	9×10^{19}	22	4.3×10^{18}
722-InN:Mg	-	300	1.39×10^{19}	-	-

5.2 Optical properties of InN:Mg/GaN

The PL spectra of both In- and N-rich InN:Mg/GaN thin films were recorded by using a combination of a 650 nm line of a diode laser module and an InSb detector, and is illustrated in figure 5.7. The InGaAs detector was employed to produce PL of the film 719-InN:Mg, where the signal was heavily quenched by the Mg overdoping. Eventually, its PL efficiency has been normalized to other spectra in order to make a reliable comparison.

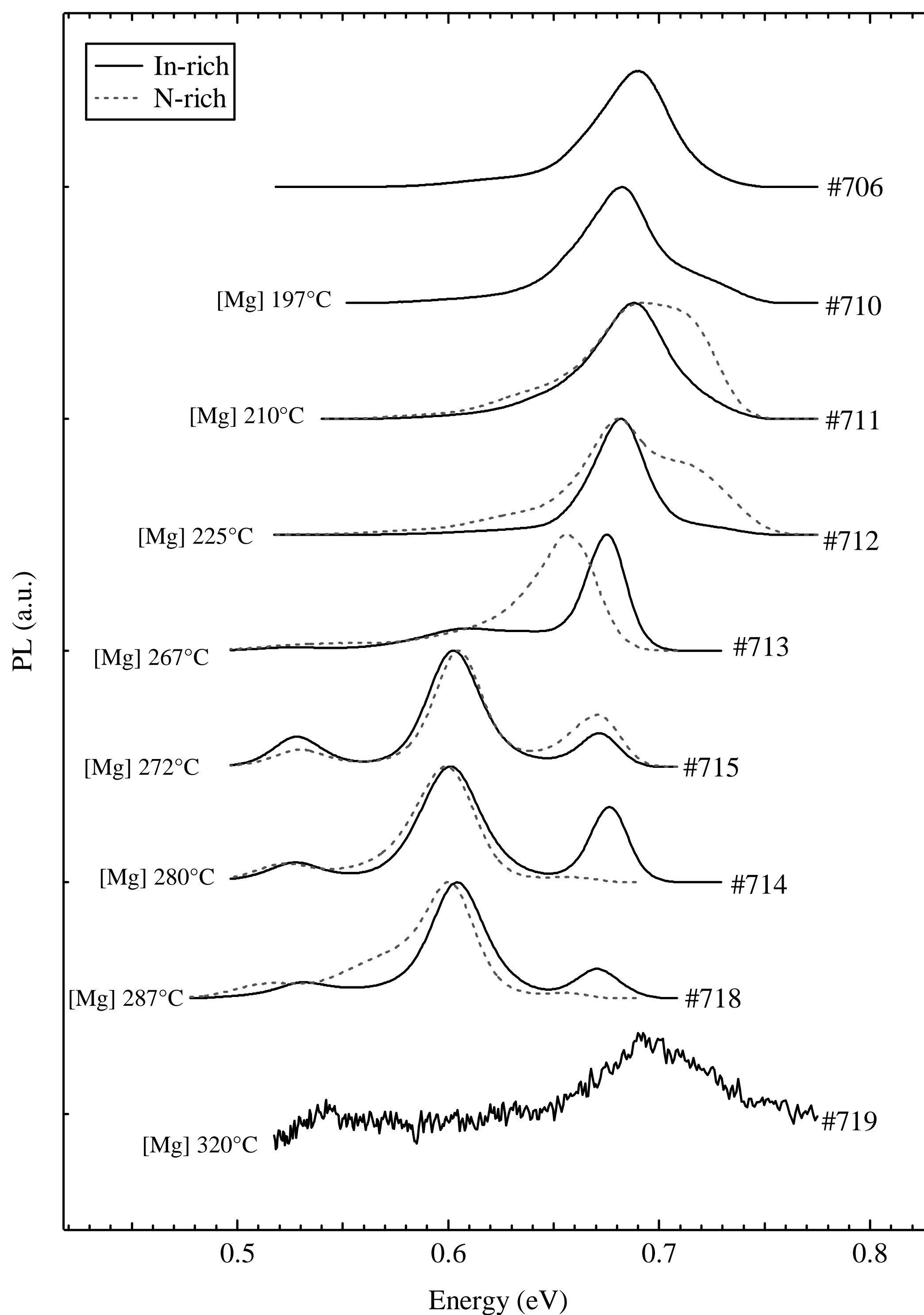

Figure 5.7 4 K PL spectra of N- and In-rich InN:Mg/GaN. The SEM image showed that the N-rich conditions were not in evidence for the two very lightly doped films (# 706 and #710). No PL is obtained from the N-rich 719-InN:Mg/GaN.

PL of samples measured from the N-rich zone generally exhibit n-InN characteristics. The four very lightly doped films show multiple overlapping components, forming an asymmetric broad emission extended over the bandgap, which is typical of N-rich InN:Mg as discussed in section 4.2. Therefore, the higher shoulder feature at approximately 0.72 is assigned to the Mahan exciton[118], where the emission contains a large spread of momentum *k* and induces such a broad feature[100,155,168]. In contrast, samples from the In-rich zone of each film within a similar doping range exhibit significantly different optical characteristics. Much narrowed single spectral energies of approximately 0.67 eV at 4 K were obtained. As the Mg cell temperature is increased, the emission line becomes much narrower (more detailed plot in figure 5.10). This difference may result from more plentiful occupation of Mg substitutional sites for In-rich InN:Mg/GaN, which successfully compensates the background electron as highlighted in the Hall measurements.

The PL for N-rich InN:Mg/GaN films grown using an intermediate Mg cell temperature range of 272 to 287 °C showed a number of low energy features, although they are unlikely linked to Mg. As has been evidenced from the magnetotransport measurement, the effect of Mg doping only resulted a n-type bulk layer in this N-rich series. Thus a low energy feature should be associated with a recombination of degenerate electrons with residual impurities at a deep acceptor state. The spectra also involve the apparent LO phonon replica at energy shift of 72 meV. Also observed is an asymmetric high energy feature just below 0.7 eV, although it is strongly quenched from a Mg cell temperature of 280 °C onwards. No PL emission is detected from the N-rich 719-InN:Mg/GaN sample grown using a Mg cell temperature of 320 °C.

The overall spectral resolution of In-rich InN:Mg/GaN is comparable to what has been previously reported for undoped samples with a low electron background concentration and In-rich InN:Mg grown using a low Mg cell temperature[75,90-92,100,133]. The PL for In-rich InN:Mg/GaN films grown using an intermediate Mg cell temperature range exhibit more structured multi-components over a wide spectrum range of 0.5 to 0.7 eV, where magnetotransport successfully distinguished a p-type layer. This spectral evolution is also strongly in agreement with the SFH measurements where a potential manifestation of bulk compensation (a drop of electron concentration as a function of Mg concentration) beyond the critical Mg cell temperature of 267°C (Mg concentration of 1.84×10^{17} cm^{-3}) is seen.

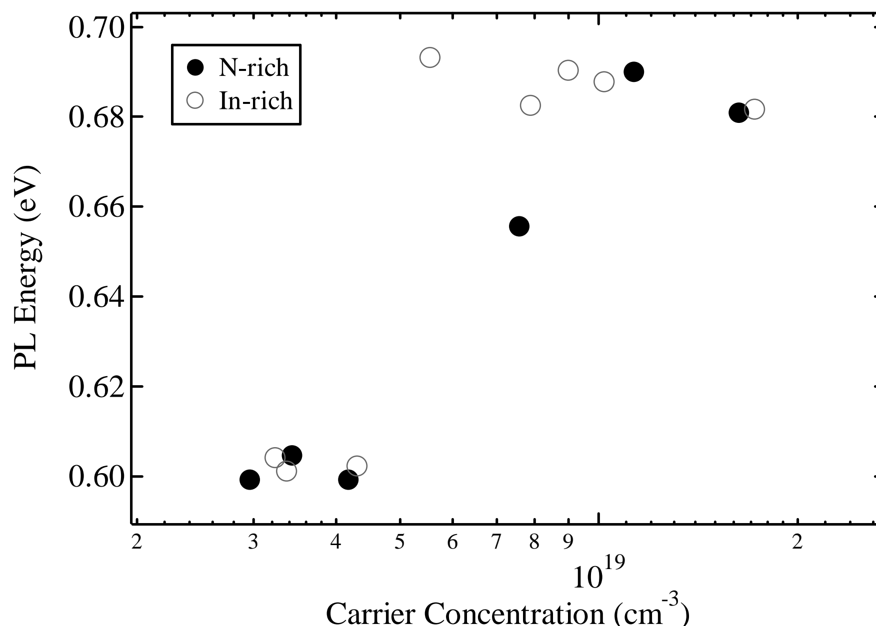

Figure 5.8 PL peak positions (potential neutral bound acceptors) of InN:Mg/GaN as a function of carrier concentration. Considering overestimated values of Mg and carrier concentrations of 712- and 713-InN:Mg/GaN, respectively, such data points have been ruled out in order to clarify the analysis.

Therefore, the presence of a feature at 0.6 eV can be ascribed to the transition from a Mg related deep acceptor state, which returns a bulk p-type. The 72 meV splitting below is the LO-phonon replica. In sharp contrast to PL measured from N-rich InN:Mg, a high energy features just below 0.7 eV remains apparent for a Mg cell temperature range of 280 to 287 °C. These symmetrical components arise and shift independently with the Mg concentration, recognizing some types of novel luminescence. To the authors knowledge there are no reported InN studies discussing the 'perfect' symmetrical PL feature. The polarity has been inversed to N-polar at the highest Mg cell temperature of 320 °C and this effect may provoke a sudden change in the spectral characteristic[134] as discussed in section 4.2.

Mg doping of N-rich InN:Mg/GaN results in a gradual redshift in the dominant peak energy until a threshold Mg content is reached, indicating the potential fluctuation of the localization states[222-224] as discussed in section 3.3. This trend is consistent with the N-rich InN:Mg/YSZ series of chapter 4. This behaviour assumes that the observed lower energy transition at an intermediate Mg cell temperature range, has a DAP character. A careful analysis can recognize the redshift of a high energy feature just below 0.7 eV as a function of the Mg concentration, confirming the originating state for PL is connected in a sense of neutral bound acceptors (*ie*. shallow acceptors).

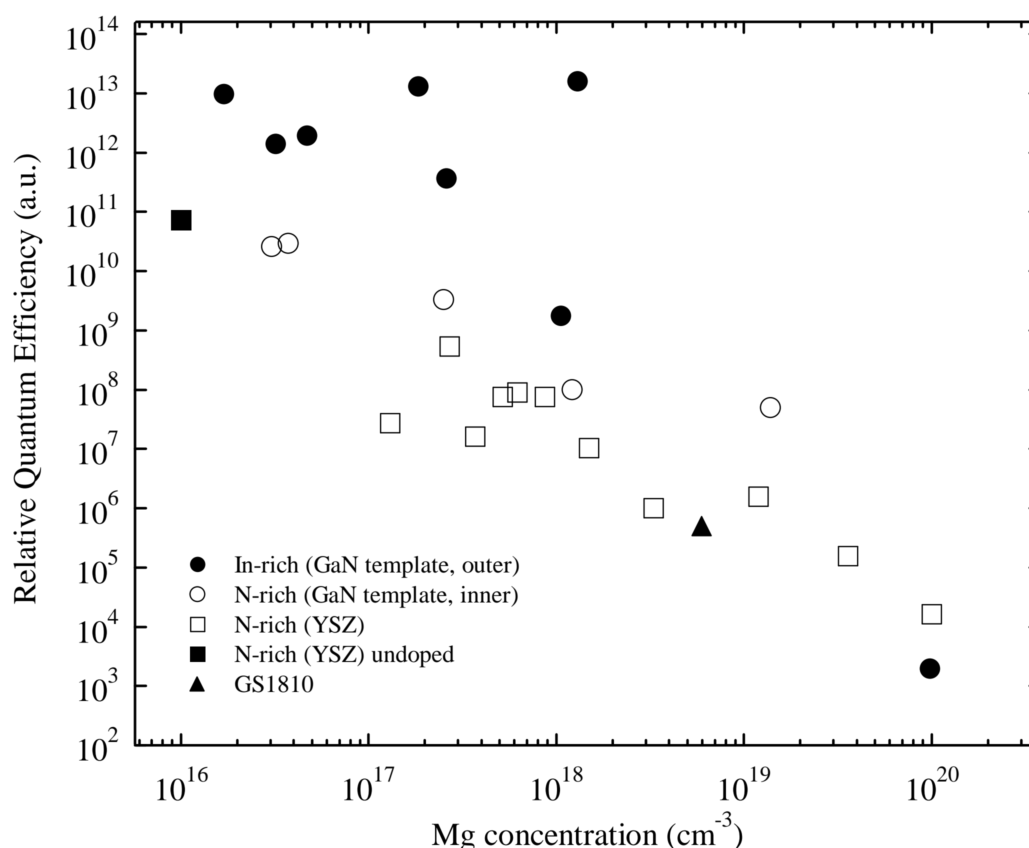

Figure 5.9 Summary of the relative quantum efficiency of InN:Mg thin films in this study as a function of the SIMS Mg concentration.

In sharp contrast, Mg doping of In-rich InN:Mg/GaN has no influence upon a peak shift (figure 5.7). This, coupled with the presence of symmetrical luminescence line at the bandedge proposes that the effective compensation of background electron concentration promotes the non-degenerate electron and hole recombination at 0.67 eV, and the presence of p-type transition at 0.6 eV (note: the potential fluctuation only occurs through the increased spatial defect frequency).

The PL behaviour of N-rich InN:Mg/GaN films correlate directly to the SFH measurements as depicted in figure 5.8. As the electron background concentration is increased the dominant emission shifts to higher energy, following the Moss-Burstein effect observed in n-InN[29]. Meanwhile, it is perhaps unsurprising to see the non-monotonic trend of energy shift with increasing carrier concentration for the samples grown under the In-rich condition as expected from the compensated background electron concentration and a different type of transition (*ie*. the onset of Mg emission) becoming a dominant.

The PL quantum efficiencies as a function of Mg concentration are depicted in figure 5.9. It is shown that the integrated PL intensity is drastically affected by Mg doping regardless of growth flux conditions. It is worth noting that the In-rich PL can exhibit much higher intensity (a few orders of magnitude) than those from N-rich conditions. This trend may be correlated to the greater amplitude of potential fluctuations from N-rich zone[222-224], where largely dispersed electronic states owing to an increased number of defects, become very effective non-radiative channels (SRH). It is plausible to see similar variation of PL responses for the two different N-rich series with Mg doping density, although interestingly these were deposited on two different substrates of YSZ and GaN/Sapphire. Seeing ahead, this phenomenon provided useful information in terms of efficiency of p-InN.

5.3 Band-to-band transition; The first discovery

The characteristic of sample 714-InN:Mg grown using a low Mg cell temperature of 280 °C stood out among the wide range of electrical and optical properties in the In-rich zone as illustrated in figure 5.5 and 5.7, respectively. Its near bandedge PL feature at 0.67 eV is perfectly symmetrical and a very low FWHM of 20 meV can be recognized in figure 5.10. Worth noting is that the FWHM of 20 meV matches well with a reported ‘defect-free’ PL line-width of InN elsewhere[120,175].

The FWHM of N-rich InN:Mg/YSZ series of chapter 4 broadens with Mg content due to the donor-like Mg-H (or interstitial In) complexes generating strong many particle interactions. The FWHM of In-rich InN:Mg/GaN however, is markedly reduced as a function of Mg content, which also parallels the Hall measurements (SFH carrier concentration). The FWHM reaches a minimum value of 20 meV at the Mg cell temperature of 280 °C, then re-broadens. Hence this is further evidence of the background electron compensation with increasing Mg cell temperature (or Mg concentration) and the particle scattering effect becomes a less concern. The later FWHM increase is likely caused by an overdoping, which introduces native defects[168]. This understanding is supported by the increase of PL line-width in GS1810 by the effect of energetic particle irradiation to raise the electron concentration as discussed in Appendix C.

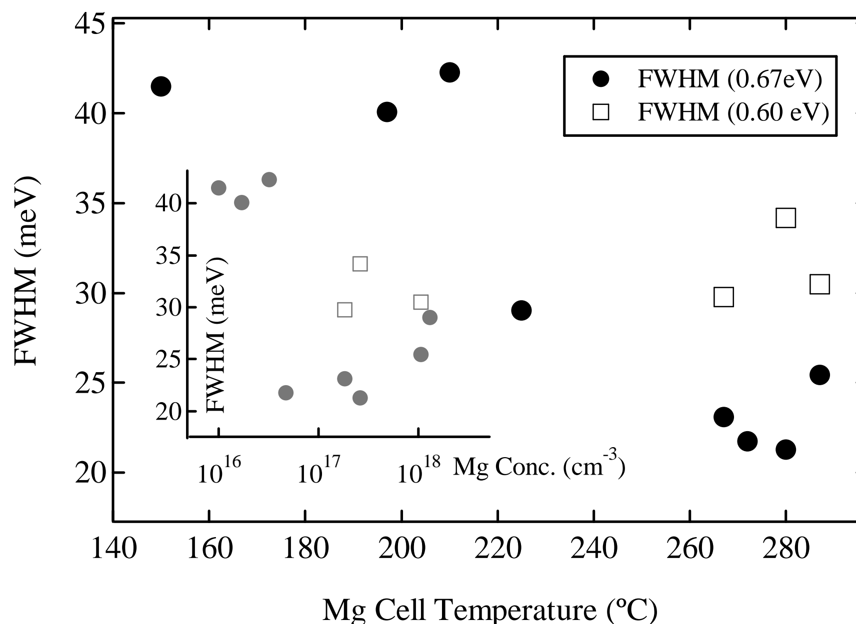

Figure 5.10 Extracted FWHM of PL spectra corresponds to Mg cell temperature, and Mg concentration (inset).

In order to firmly identify the luminescence mechanism, an excitation intensity dependent PL study was made. Figure 5.11 displays the excitation intensity dependent PL of In-rich 714-InN:Mg. Three PL emission peaks are clearly observed at 0.53 (I_{LO_fb}), 0.60 (I_{fb}), and 0.67 eV (I_{bb}). An analysis of the I_{bb} feature exhibits direct evidence of a band-to-band transition, which to our knowledge is the first such observation. As illustrated in the inset, the extracted power-law exponent k gives a quadratic power dependence and is a manifestation of "true" band-to-band recombination[255]. A quadratic relation is not known to have been mentioned elsewhere, although the most commonly seen optical transitions of InN in literatures are also peaking at 0.67 eV[75,90,91,100,133,155]. The extracted value of k from such literatures returned sub-linear power dependences.

The various peak intensities in the In-rich 714-InN:Mg/GaN spectrum as a function of excitation intensity return a different power-law exponent k. The extracted value of k is 0.59 for the I_{fb} peak and is attributed to a free-to-bound transition. The lowest energy component at approximately 0.53 eV is most likely the LO-phonon replica of I_{fb}. Considering the linkage between these two transitions, it is unsurprising to see their duplicated behaviors as a function of excitation intensity. The energy spacing of 72 meV between I_{fb} and I_{LO_fb} is indeed consistent with a previous report[91]. If these recombination mechanisms are correctly assigned, the pronounced blueshifts with increasing excitation power are attributed to the Moss-Burstein effect. Worth noting is that a low electron carrier concentration as extracted from

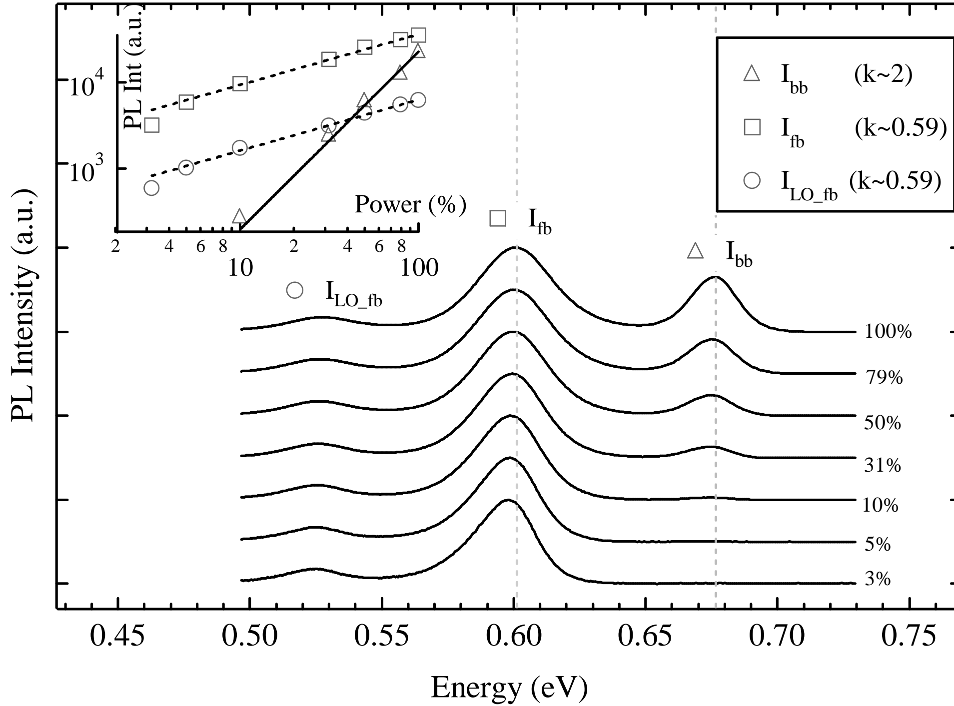

Figure 5.11 Excitation power dependent PL for the In-rich 714-InN:Mg/GaN film grown with a Mg cell temperature of 280°C (The features are normalized and offset vertically for clarity). The inset shows the log slope of three different components by using a power law equation.

VFH of this film should be in a vicinity of non-degenerate level for InN as discussed in section 3.5. This makes it possible to observe a pronounced blueshift of a free-to-deep acceptor I_{fb}, whereas this observation mostly swamped by the high background concentration of typical InN[91].

More useful information is available from temperature dependent PL. Its characteristics perfectly agree with the theoretical perspective and strongly support the proposal of a band-to-band transition. Temperature dependent PL spectra of 714-InN:Mg is displayed in figure 5.12. Clear band tailing effects[99,168] for I_{bb} at high temperatures are observed. This non-symmetric broadening effect of band-to-band transition at the high energy wing can be described by the classical Boltzman statistics[214]:

$$E_{\mathrm{g}}(h\nu) \propto \left(h\nu - E_{\mathrm{g}}\right)^{1/2} \exp\left(-\frac{h\nu - E_g}{k_{\mathrm{B}}T}\right) \quad (5.1)$$

This equation includes the high energy levels of the conduction band becoming thermally occupied as temperature increases. This gives the exponential tail (e^{kT}) on the high energy wing, forming a non-symmetrical PL line-shape. As shown in the figure, the high energy

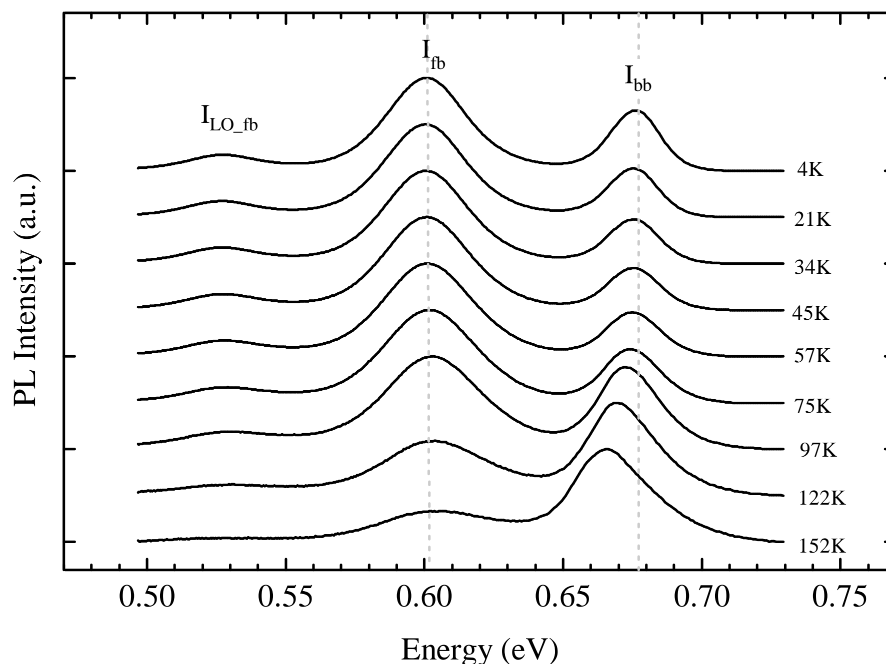

Figure 5.12 Temperature dependent PL for the In-rich 714-InN:Mg/GaN film grown with a Mg cell temperature of 280°C (The features are normalized and offset vertically for clarity).

shoulder of the bandgap transition at 152 K can be well described by an exponential decaying curve, as it follows the band tailing effect[99,168] and this theoretical view gives confidence to assign a true band-to-band recombination[104,105].

In order to solidly identify the origin of the transition at 0.6 eV, its Arrhenius decay characteristic has been examined using equation 3.16. As shown in figure 5.13, the activation energy of non-radiative recombination channel yields 50 meV, which coincides well with reported Mg activation energies of InN[75,92,133,216]. The lower activation energy of 14 meV is attributed to hole dissociation at the low temperature region. The rather high value of a second activation energy may correlate to the nature of Mg forming a deep acceptor. Theoretical treatment of Arrhenius on the band-to-band transition is rather superfluous since the formation of a non-radiative channel is rather meaningless.

Searching for more evidence continued, especially additional support for a band-to-band transition, and was found in the assignment of PL energy variation with temperature. I_{bb} exhibits a pronounced redshift effect (more prominent than from a DAP transition in figure 4.15) with increased temperature as it follows the bandgap narrowing. In temperature dependent PL, the dynamics of energy shifting is analysed by the Bose-Einstein and Pässler

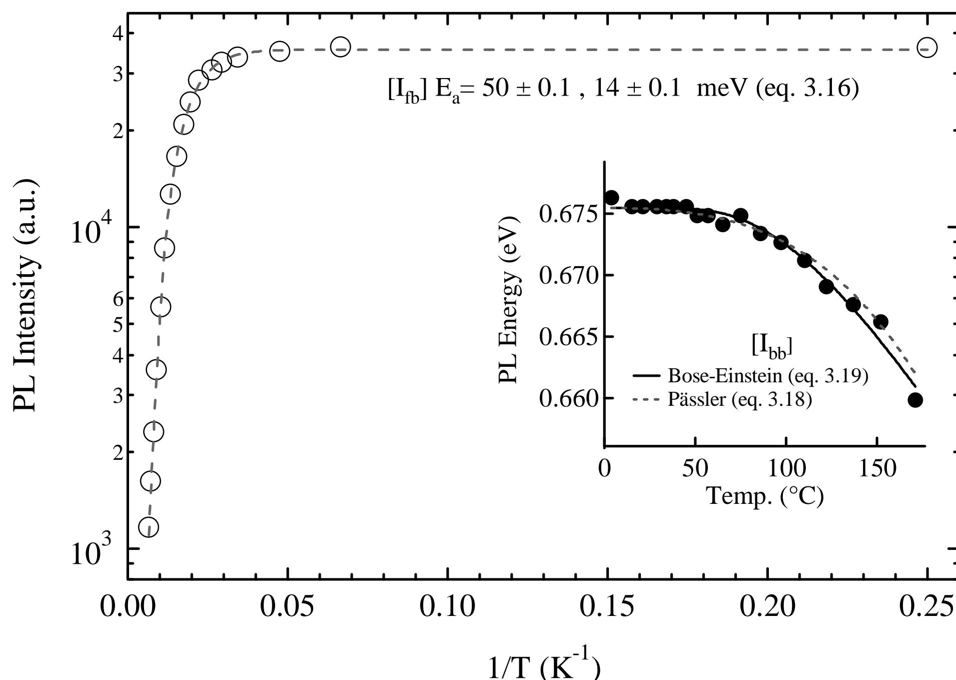

Figure 5.13 The Arrhenius plots of the absolute peak intensities for I_{fb} (0.6 eV). The inset shows the Pässler and Bose-Einstein plots of the variation of I_{bb} (~0.67 eV) emission centres as a function of temperature.

models[104,105]. The band-to-band recombination readily fits into empirical relations as shown in the inset of figure 5.13. The details of fitted parameters have already been covered in section 3.7. The combined PL results are intimately linked to a useful understanding of the optical bandgap transition and these plausible conclusions are of consequence in the potential bandgap determination of InN.

Meanwhile, the peak 0.6 eV appears to have a temperature induced 'S' shaped' (very slight) energy shift as shown in figure 5.12. This phenomenon, while previously seen in a potential Mg-related emission from 590-InN:Mg/YSZ ('C'.,N-rich), involves the thermally excited electrons being transferred to the resonant donor states above the CBM with increasing temperature. Considering the presence of band-to-band transition, the electron in the emitting state of conduction band of this particular sample should be non-degenerate and thus, the temperature induced 'S shaped' energy shift becomes much weaker (a less occupied conduction band state) relative to the emission from 590-InN:Mg/YSZ. Seemingly, this type of behavior is associated with a Mg related emission in some extent.

In figure 5.14, PL spectra were performed for In-rich 714-InN:Mg/GaN using the laser operating in the wavelength range from 488 nm to 808 nm as excitation sources. The results

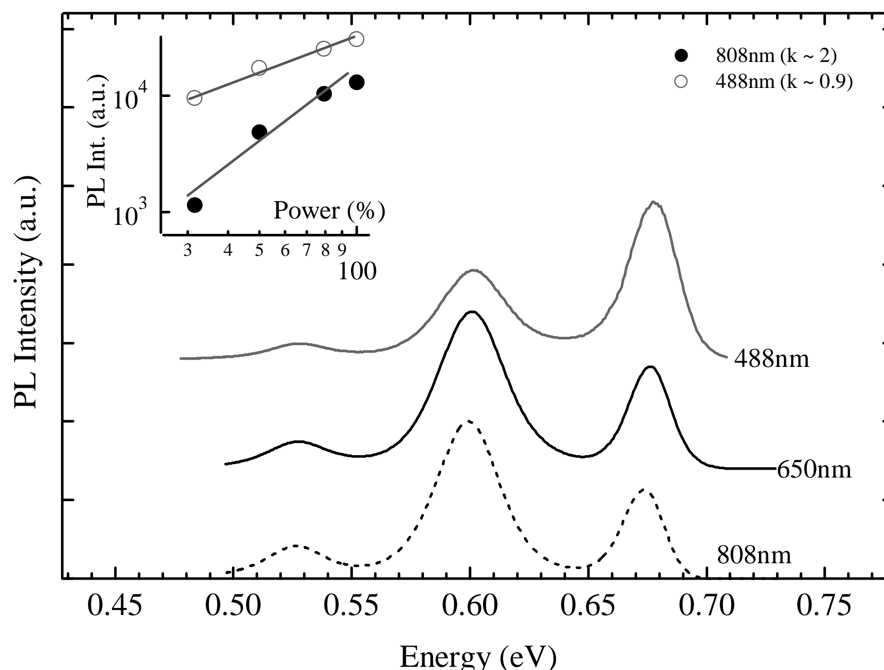

Figure 5.14 4 K PL spectra of sample In-rich 714-InN:Mg/GaN as a function of excitation wavelength (The features are normalized and offset vertically for clarity). The inset shows the log slope of I_{bb} peak extracted with a different excitation source. The power-law exponent k gives a quadratic and sub-linear relation for a 808 nm and a 488 nm lasers, respectively.

show that the band-to-band transition can be significantly affected by excitation energy as evidenced from the different power-law exponent k. The extracted value of k from a 488 nm Argon laser gives sub-linear power dependence, whereas with a 808 nm laser module k remains being a quadratic. The least square fit of power law using a 650 nm laser diode is already covered in figure 5.11 (a quadratic). A possible reason is associated with the shorter average depth that a photon penetrates for a 488 nm Argon laser as discussed in section 3.9. PL (the diffusion of photo-excited carriers) using a 488 nm Argon laser is somewhat perturbed by the surface electron accumulation layer and thus the band-to-band transition could be “washed away”. Also observed is the redistribution of PL intensity between the band-to-band and the Mg-related peak. This view infers the 0.67 eV peak being a free-to-shallow acceptor, where the trapping strength is relatively less than a deeper state.

5.4 Excitonic transition; The unexpected discovery

To the authors knowledge, the excitonic recombination also has never been mentioned in this material. Here, the evidence of a neutral acceptor bound exciton (A°X) is presented. Figure

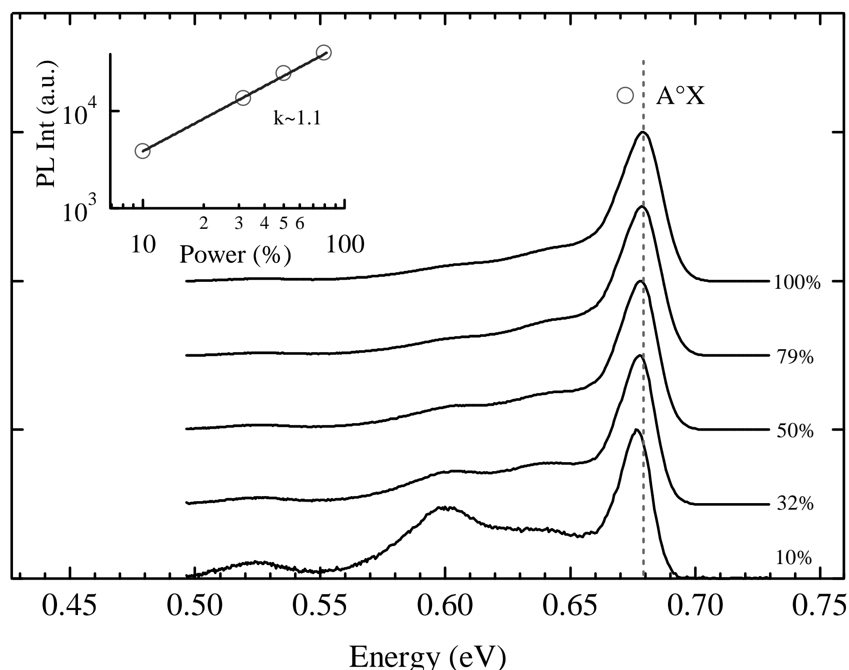

Figure 5.15 Excitation power dependent PL for the In-rich 713-InN:Mg/GaN film grown with a Mg cell temperature of 267 °C (The features are normalized and offset vertically for clarity). The inset shows the log slope of main component (A°X) by using power law equation.

5.15 displays the excitation intensity dependent PL of In-rich 713-InN:Mg/GaN grown using a low Mg cell temperature of 267 °C. The doping density of this film is just a step below In-rich714-InN:Mg/GaN. The PL is monopolized by the almost symmetrical spectrum near 0.68 eV and the feature blueshifts with increasing laser power as it follows the Moss-Burstein effect. This indicates that the originating state for PL should be connected to the CBM or above[29]. This interpretation rules out the possibility of a free or a neutral donor bound exciton and is an appropriate reason why this transition is at a higher energy than the band-to-band PL of In-rich 714-InN:Mg/GaN. It is concluded that the observed transition at 0.68 eV has a shallow acceptor bound exciton character as the VFH measurement indicates that the bulk hole carrier concentration is slightly higher than the electron population (figure 5.6).

The response of this peak to varying excitation intensity has a clear difference to a band-to-band transition. The inset of fig 5.15 describes the standard power-law relation of the dominant peak centre at 0.67 eV. A linear (k~1.1) characteristic corresponds to an excitonic recombination. Meanwhile, multiple overlapping PL components in a spectral range of 0.54 and 0.60 eV can be noticed at low excitation intensity. A tentative explanation is that the 0.6 eV peak arises from transitions of free electrons in the conduction band to a deep acceptor state and the 0.54 eV peak is the LO- phonon-replica.

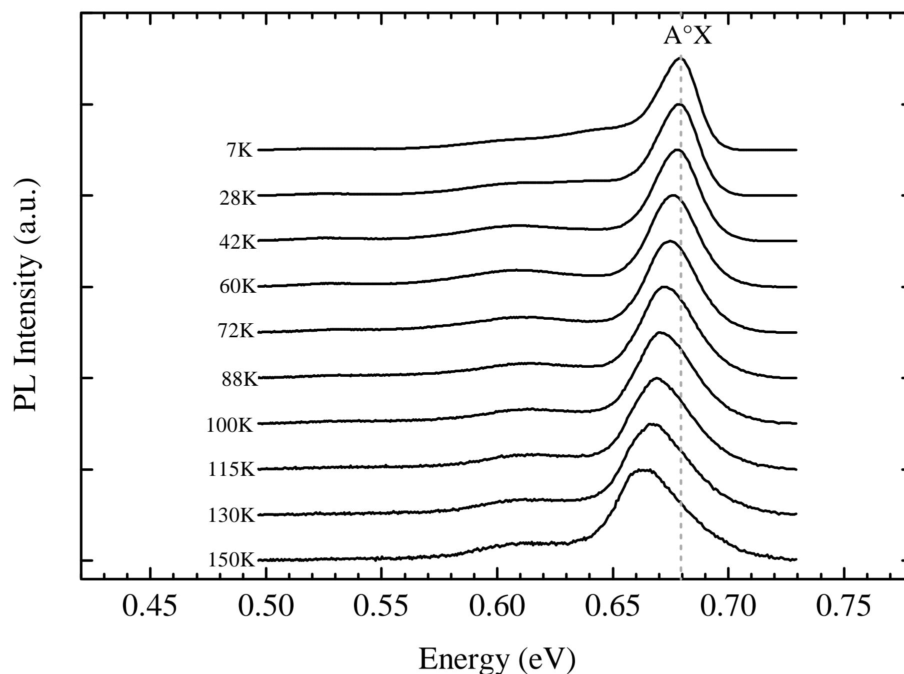

Figure 5.16 Temperature dependent PL for the In-rich 713-InN:Mg/GaN film grown with a Mg cell temperature of 267 °C (The features are normalized and offset vertically for clarity).

Once the existence of a neutral acceptor bound exciton is convincingly established, the question is naturally directed to its activation energy. Figure 5.16 shows the temperature dependent PL of 713-InN:Mg/GaN. A typical excitonic behaviour can be identified. The neutral acceptor bound exciton emission decayed in intensity and redshifted as the temperature increased. It thoroughly dominated the PL, even at higher temperatures, while the 0.6 eV peak is more apparent at the high temperature due the increased population of thermally released free carriers from the neutral acceptor bound exciton.

The thermal quenching process of exciton transition should be drawn by a single activation energy, representing the localization energy. However, as is shown in figure 5.17 a single energy model does not fit well at the “knee” point of the data. Therefore, a thermal quenching process with dual activation energies is considered and is also presented in figure 5.17. The fit returns the activation energies of 8 meV and 26 meV. The former represents the localization energy of 8 meV and the latter in this case may describe the energy required to thermally break the exciton pair, the ‘binding energy’. An unusually large thermal dissociation value of 26 meV is perhaps the physical signature of an excitonic nature. Arguably, the neutral bound exciton peak also has a high energy broadening at the high

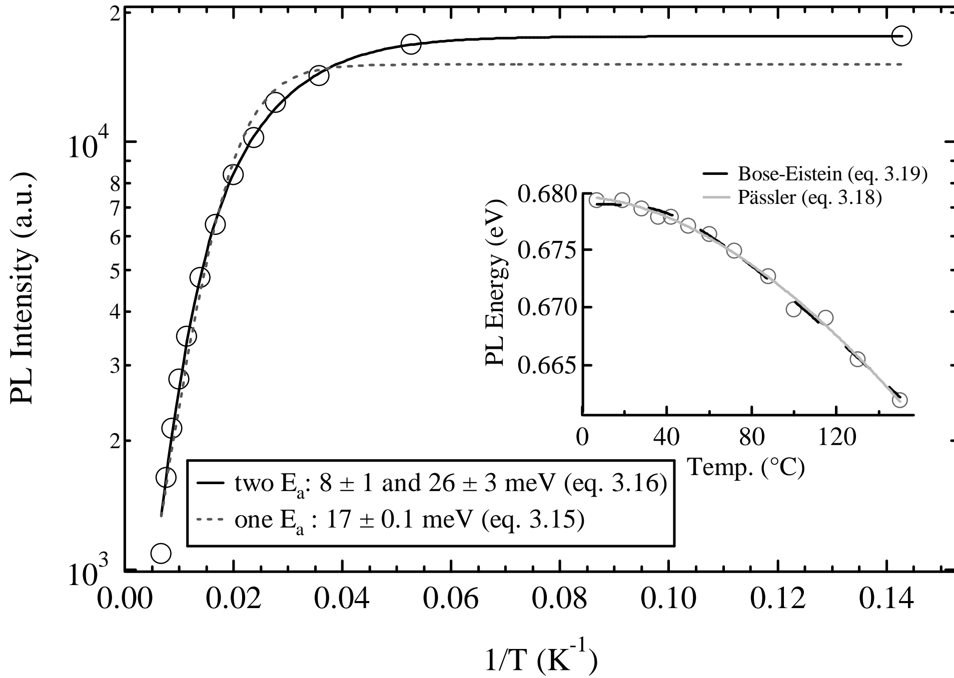

Figure 5.17 The Arrhenius plots of the absolute peak intensities for A°X. The inset shows the Pässler and Bose-Einstein plots of the variation of A°X emission centres as a function of temperature.

temperature like the band-to-band transition of the In-rich 714-InN:Mg/GaN. This may be attributed to the localization level of this transition being nearby the VMB. The inset of figure 5.17 shows the position of the neutral acceptor bound exciton peak with the solid and dotted lines representing the fits of Bose-Einstein and Pässler models (eq 3.18, and eq 3.19, respectively). The detail of fitted parameters is shown in section 3.7.

Another analytical treatment that can convincingly identify the exciton is a line broadening effect. At high temperature, the interaction between excitons and LO phonons becomes more vibrant and disperses across the bandgap, leading to the effective PL line broadening. This interpretation gives the theoretical formula for the line-width,[104,105]

$$\S(T) = \S_o + \O T + \frac{\S_{\mathrm{LO}}}{\exp\left(\frac{E_{\mathrm{LO}}}{k_{\mathrm{B}}T}\right)-1} \tag{5.2}$$

where $\S_{\mathrm{LO}}$ is a LO phonon energy, $\S_o$ is the broadening parameter at 0 K, $\O$ is the coupling strength of an exciton-acoustic phonon interaction, and E_{LO} is a parameter describing the exciton-LO phonon interaction. The LO phonon energy of 72 meV was used in this fitting[90].

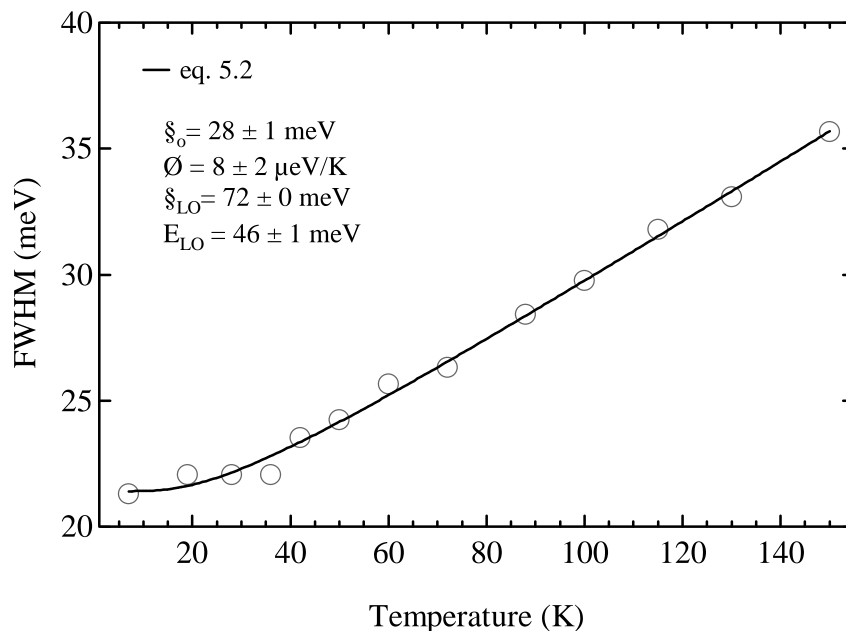

Figure 5.18 The Bose-Einstein plots of the PL line-width (FWHM) for A°X.

As shown in figure 5.18, the broadening effect is in agreement with the theoretical formula. This view is a strong evidence that the 0.68 eV emission is the exciton-induced PL. The fitted parameters using equation 5.2 return 28 meV, 8 μeV/K, and 46 meV for $\S_o$, *Ø*, and E_{LO}, respectively. As expected, the coupling strength of an exciton-acoustic phonon interaction (*Ø*) of 8 μeV/K is much weaker than in GaN (28 μeV/K) and AlN (57 μeV/K), which depends on the ironic bond strength of the material[247].

In order to convincingly understand the recombination dynamics of neutral acceptor bound excitonic recombination, the power-law coefficient k is examined as a function of temperature. A preliminary expectation concerns two step mechanisms: 1) the thermal dissociation of excitons into free carriers when the available thermal energy exceeds the binding energy of 26 meV and 2) after the excitonic pair is delocalized, an extra hole carrier from this “three-body” complex (2h1e) is transferring a free-to-shallow acceptor transition as discussed in section 3.2. The origin of PL emission therefore changes from a neutral acceptor bound exciton to a free-to-acceptor like with an increased temperature and thus the power law coefficient k value should be decreased[169-171].

Figure 5.19 draws together the dynamics of the power-law coefficient k as a function of temperature. The assignment of k clearly depends on ambient temperature. The exponents yield a constant value of 1.1 in the experimental temperature range of 7 to 150 K, while this

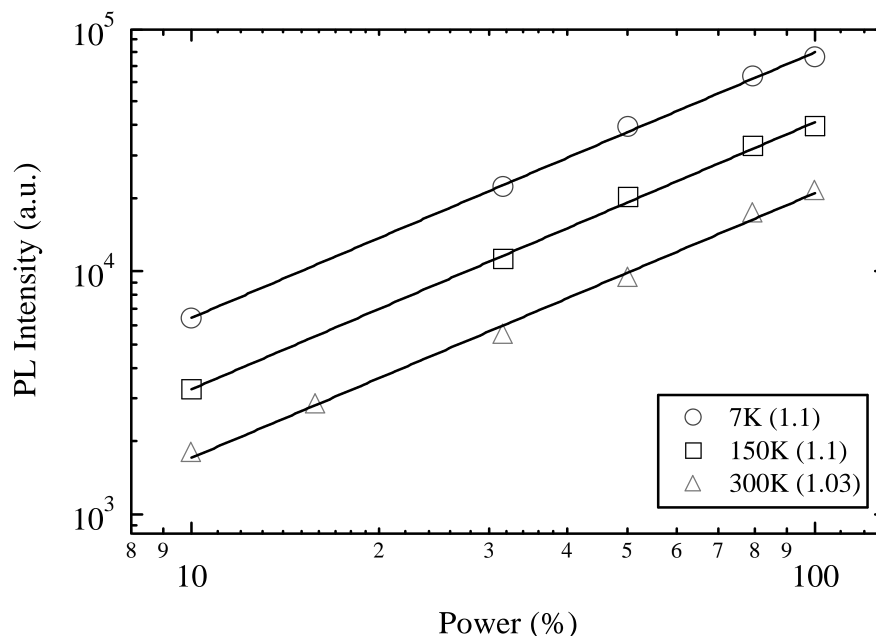

Figure 5.19 The fitted experimental data of In-rich 713-InN:Mg/GaN and the fit to the power-law as a function of laser power for several representative temperatures (offset vertically for clarity).

valuation slightly decreases at 300 K, which corresponds to an extracted binding energy of 26 meV. The findings are in accordance with the foregoing discussion that this trend is an elucidation of the onset of a thermalization process from being a neutral acceptor bound acceptor into a free-to-acceptor-like transition. Arguably, the extracted value of k for three temperatures is still within an experimental error. Perhaps a more rigorous practise is to extend the temperature range.

5.5 Brief Summary

The PL evolution in In-rich InN:Mg/GaN with changing Mg content has a discernible difference to the N-rich InN:Mg/YSZ series of chapter 4. Figure 5.20 displays the extracted power-law coefficient of observed transition as a function of Mg cell temperature. Sub-linear power dependences are in evidence for the three very lightly doped films. This observation is comparable to a N-rich InN:Mg/YSZ series and is attributed to a free-to-shallow acceptor transition. Perhaps, the only difference is the activation energy of the shallow acceptor level. The average activation energy extracted from the In-rich InN:Mg/GaN is in a range of 13-30 meV. This given range is approximately 10 meV greater than that those from a N-rich series of chapter 4, where the background electron concentration is much higher. This proposes that

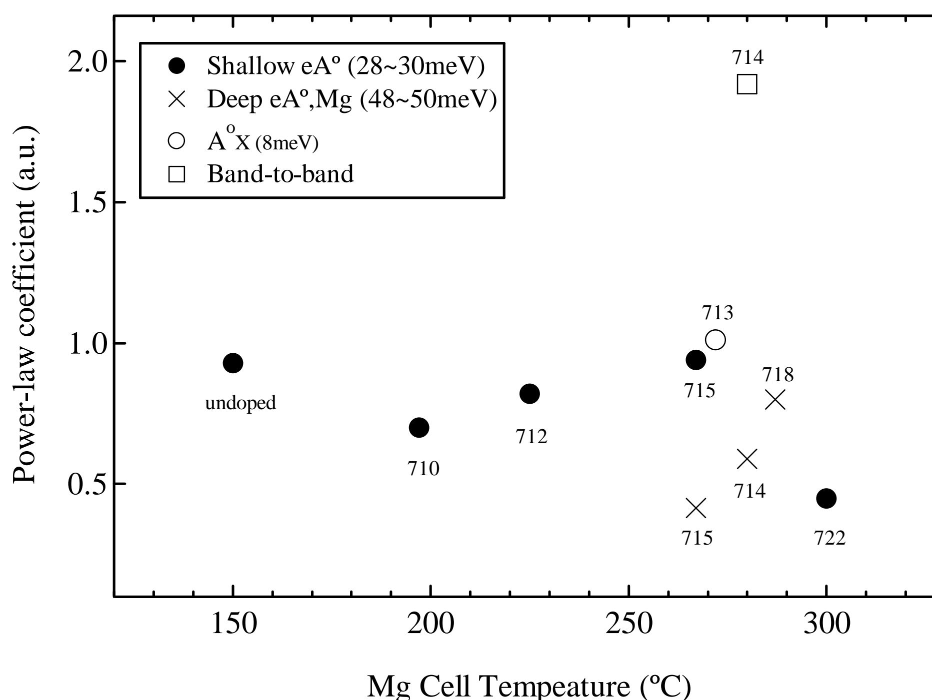

Figure 5.20 The compressive details of optical properties for In-rich InN:Mg/GaN as a function of Mg cell temperature. The symbols designate the discernible recombination processes which have been determined by the PL study. Parentheses indicate the activation energy (the formation of a non-radiative channel).

the non-radiative recombination process activation energies are affected by the carrier concentration since a larger number of ionized impurities are likely attracted by (the Coulomb interaction) the holes in the VBM.

The samples grown using a moderate Mg cell temperature of 280 °C produces the band-to-band transitions as evidenced from the PL. This conclusion is drawn by four theoretical supports of: 1) the corresponding power-law exponent being a quadratic relation, 2) a perfect symmetric line shape indicating the 'non-degenerate' (or 'defect-free') PL emission, 3) the band tailing effect at the high temperature region, and 4) a pronounced redshift as a function of temperature. Apart from this critical sample, the carrier concentrations as extracted from VFH are much higher for other samples, and the calculated exponent k equal or less than linear, indicative of a neutral acceptor bound exciton and free-to-shallow acceptor.

The potential "p-type window" in this series corresponds to a Mg cell temperature range of 272 °C to 287 °C (2.6×10^{17} to 1.0×10^{18} cm^{-3}), where VFH measurement recognized a p-type layer. This range is an order of magnitude less than reported ranges elsewhere[75,155]. The PL

for In-rich InN:Mg/GaN films grown inside the given Mg concentration range show a number of low energy peaks and are Mg deep acceptor states. The extracted Mg activation energy is in a range of 48 to 50 meV and is consistent with the expected deep acceptor level for Mg in InN[75,92,133,216]. Finally, at the highest doping level, the dominant PL feature shifts to higher energy and the transition type of a free-to-shallow bound re-appears. This implies the Mg incorporating in either the interstitial In or Mg-H complex as has been the case for N-rich InN:Mg/YSZ in chapter 4.

Our results conclude that careful controls of Mg doping level and the In/N flux ratio are necessary to successfully compensate the electron background concentration which leads to both the distinctive observation of a band-to-band and a Mg-related PL transition in InN. Also observed is that the In-rich growth favors Mg incorporation on In vacancy sites rather than N-rich growth. Detail of the observed luminescence transitions of the In-rich InN:Mg/GaN is listed in table 5.2.

Table 5.2 The list of transition detail and extracted important parameters.

In-rich Film #	Polarity	T_{Mg} (°C)	Mg_{conc} (cm^{-3})	Energy	Trans. Type
710-InN:Mg	In	197	1.7×10^{16}	0.68 eV	$I_{eA^\circ\,(shallow)}$
711-InN:Mg	In	210	3.2×10^{16}	0.69 eV	$I_{eA^\circ\,(shallow)}$
712-InN:Mg	In	225	1.31×10^{18}	0.68 eV	$I_{eA^\circ\,(shallow)}$
713-InN:Mg	In	267	1.84×10^{17}	0.68 eV	$I_{A^\circ X}$
715-InN:Mg	In	272	4.7×10^{16}	0.60, 0.67 eV	$I_{eA^\circ\,(Mg)}^{LO}$, $I_{eA^\circ\,(shallow)}$
714-InN:Mg	In	280	2.6×10^{17}	0.60, 0.67 eV	$I_{eA^\circ\,(Mg)}^{LO}$, I_{bb}
718-InN:Mg	In	287	1.06×10^{18}	0.60, 0.67 eV	$I_{eA^\circ\,(Mg)}^{LO}$, unknown
722-InN:Mg	N	300	4.99×10^{19}	0.69	$I_{eA^\circ\,(shallow)}$

Note: LO → Consists LO-phonon replica.

Chapter 6

Potential acceptor dopants

6.1 Zinc doped InN; a p-type dopant for InN?

Despite the great success in establishing that Mg is a viable p-type dopant for InN, the persistent issue of an extreme surface electron accumulation layer is still problematic. Potential solutions discussed in the literature highlight InAs. InAs also greatly suffered from a surface electron accumulation layer with a much n-type narrow bandgap of 0.36 eV[177]. If for no other reason, it seems natural to benchmark p-InAs given its success with Zn incorporation[178].

The propensity of Zn incorporation to the III-V semiconductors is rather unique. There is a tendency for Zn-doped III-Vs to be semi-insulating[179]. This situation rendered a difficulty in probing p-type characteristics and the high resistivity buffer layer was unconditionally needed in order to compensate the residual donors for a III-V:Zn and for an eventual device application (*ie*. GaN:Zn based LEDs)[179-181].

In terms of PL, GaN:Zn has been reported to be an effective light emitter, which can deliver a number of visible lines over a wide range of the spectrum[182,183], although GaN doping with Zn seemed to be insufficient due to its deep ionization energy of 340 meV[226]. This value is almost twice as much as a Mg ionization energy and returns a rather high Hall resistivity, which is rather problematic for an eventual application. Also reported was that GaN:Zn can be fitted into the substitutional, interstitial and complex arrangements[227].

To date, a limited number of studies have been conducted on Zn-doped InN. Chen *et al.*[184,185] reported an annealing study of InN:Zn. Their RF sputtering grown thin films exhibited a

weak onset of optical absorption edge located above 1.9 eV[185]. The electrical property was rather poor. The SFH measurement revealed the somewhat large carrier concentration of a 5.6×10^{20} cm^{-3} and low mobility of 14.6 $cm^2V^{-1}s^{-1}$. The likely reason for these poor properties is an oxygen contamination as has been the case for early RF-sputtered polycrysyallines of InN containing very high background electron concentration[26-29]. Recently, the characterization of MOCVD grown Zn doped InN nanorods was explored by Song *et al.*[186]. The emphasis was on growth morphology of InN:Zn nanorods, and less attention was paid to the optical and electrical characteristics. So far, only two reports of Zn doping in InN are published. Naturally, little is known about the central property of InN:Zn and conclusive results of recombination mechanism are yet to be discussed.

6.1.1 The growth parameters and electrical properties

Growth, SEM, and SFH by Dr. Chito Kendrick at University of Canterbury

In order to determine whether Zn is a true acceptor for InN, the investigation of Zn-doping of InN was explored. The research framework has followed the context of InN:Mg studies. As has been mentioned, a GaN buffer layer is expected to improve the material's performance in both the electrical and optical sectors[181]. The PAMBE growths of a Zn-doped InN series were grown both N- and In-rich on GaN template/sapphire. A 60cc effusion cell was installed as a source for a Zn.

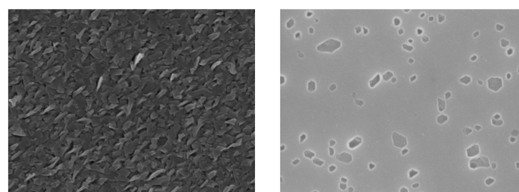

Figure 6.1 SEM images of the N- (left) and In-rich (right) InN:Zn/GaN films grown with a Zn cell temperature of 248 °C.

The flux condition was strongly connected to the surface morphology. The SEM images discriminate the N- and In-rich regimes as displayed in figure 6.1. As always has been for InN, a relatively smooth surface is evidence for In-rich, whereas N-rich displayed a roughness. KOH etching of InN:Zn/GaN found no polarity inversion from the In-face, consistent with a polarity effect study of GaN:Zn[182,183].

As displayed in figure 6.2, the SFH electrical properties are rather insensitive to Zn content. The higher mobility value is measured from samples taken from In-rich zone throughout a wide Zn cell temperature range. The N-rich Hall mobility shows a monotonic reduction with

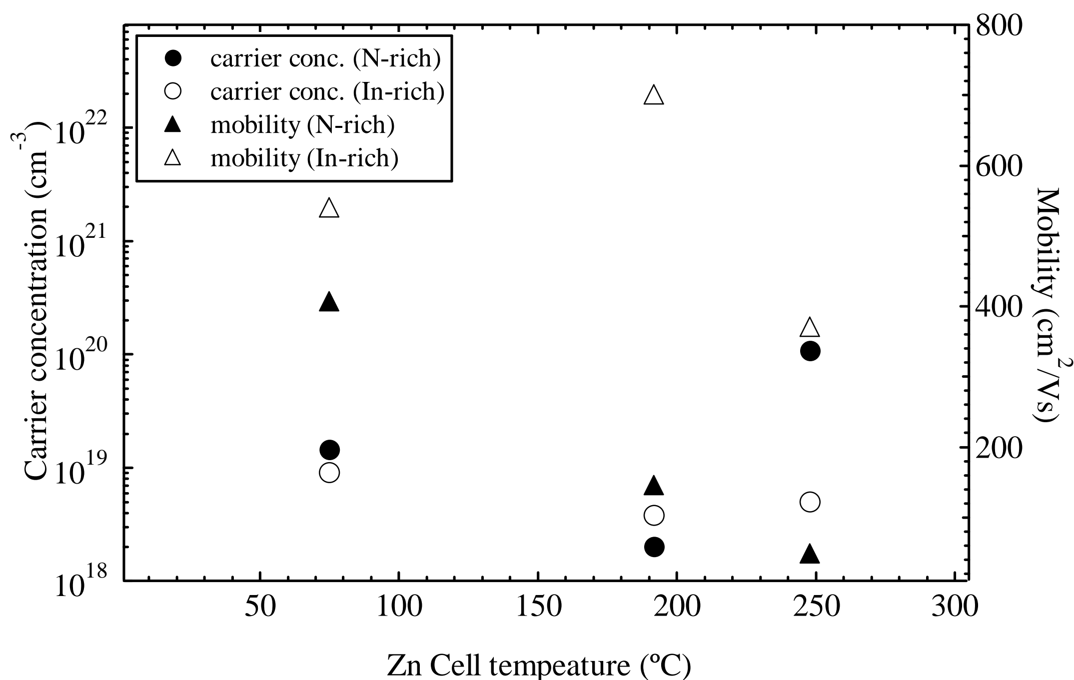

Figure 6.2 SFH electrical properties of an InN:Zn/GaN series as a function of Zn cell temperature.

increasing Zn concentration, whereas no particular pattern is obtained from the In-rich regime. Meanwhile, the carrier concentrations of both the N-rich and In-rich InN:Zn/GaN are randomly distributed, clustering at 10^{19} cm^{-3} and the rather high values from both indicate that the surface electron accumulation layer is still strongly present. The best electrical result is optimized at a Zn cell temperature of 192 °C, regardless of flux conditions, showing the lowest electron background concentration and the highest mobility.

For a better understanding, the electrical properties of InN:Zn were further explored by VFH. Despite this, a sign of p-type bulk layer has not been observed, and the SIMS also could not probe any Zn concentration. This tentatively suggests that Zn is introducing a large number of native donors and makes InN insufficient to compensate the background electron concentration. Nonetheless, the VFH carrier concentration shows a slight improvement, where this measurement is unlikely perturbed by the surface electrons. The obtained parameters as extracted from Hall effects are summarized in table 6.1. Similar to what has been previously seen for InN:Mg of chapter 4 and 5, the electrical property of the region grown under N-rich condition was poorer[117,155,156]. A main hurdle in this analysis is having such a small sample set. Consequently, a significant interpretation may be limited.

Table 6.1 A summary of growth conditions and Hall effect measurements of Zn doped InN/GaN films.

# Film (N-rich)	Polarity	T_{Zn} (°C)	Carrier conc. (cm^{-3})	Mobility (cm^2/Vs)
627-InN:Zn	In	75	1.44×10^{19}	406
621-InN:Zn	In	192	2.01×10^{18}	145
619-InN:Zn	In	248	1.08×10^{20}	48
# Film (In-rich)				
656-InN:Zn	In	75	9.00×10^{18} (3.4×10^{18})	540 (864)
653-InN:Zn	In	192	3.80×10^{18} (3.2×10^{18})	700 (875)
655-InN:Zn	In	248	5.00×10^{18} (2.1×10^{18})	370 (621)

Note: Parentheses indicate the VFH measurement.

6.1.2 Optical properties of InN:Zn/GaN

TRDT by Dr. Maurice Cheung at The State University of New York

The InN:Zn/GaN (N- and In-rich) samples were excited with a 650 nm radiation from a 150 mW diode module and the PL signal from these emissions were collected into a liquid nitrogen cooled InSb (and InGaAs detectors). Figure 6.3 shows 4 K PL from films grown under N- and In-rich conditions. PL of N-rich films exhibits the structureless multiple high-energy features as expected from the scattering effect of InN with the high background electron concentration. Despite this, the dominant peaks are realized with a careful analysis and it shows the Moss-Burstein effect as a function of Zn cell temperature[29]. This phenomenon literally suggests the introduction of many point native defects (increases carrier concentration) with a Zn doping as expected from a N-rich InN:Mg/YSZ series of chapter 4, where overall PL is governed by the recombination from highly degenerate free electrons to potential localized states somewhere near the valence band[91]. The PL spectrum of 619-InN:Zn grown with a Zn cell temperature of 248 °C is partially dismissed by the detector limitation of InGaAs and its dominant peak only can be estimated.

In contrast, the PL of the In-rich zone is well regulated. The total spectral configuration consist of four multiple radiative paths over a wide range of 0.54 to 0.72 eV. All samples exhibit features at energies above to the bandgap. The origins are worth considering. We

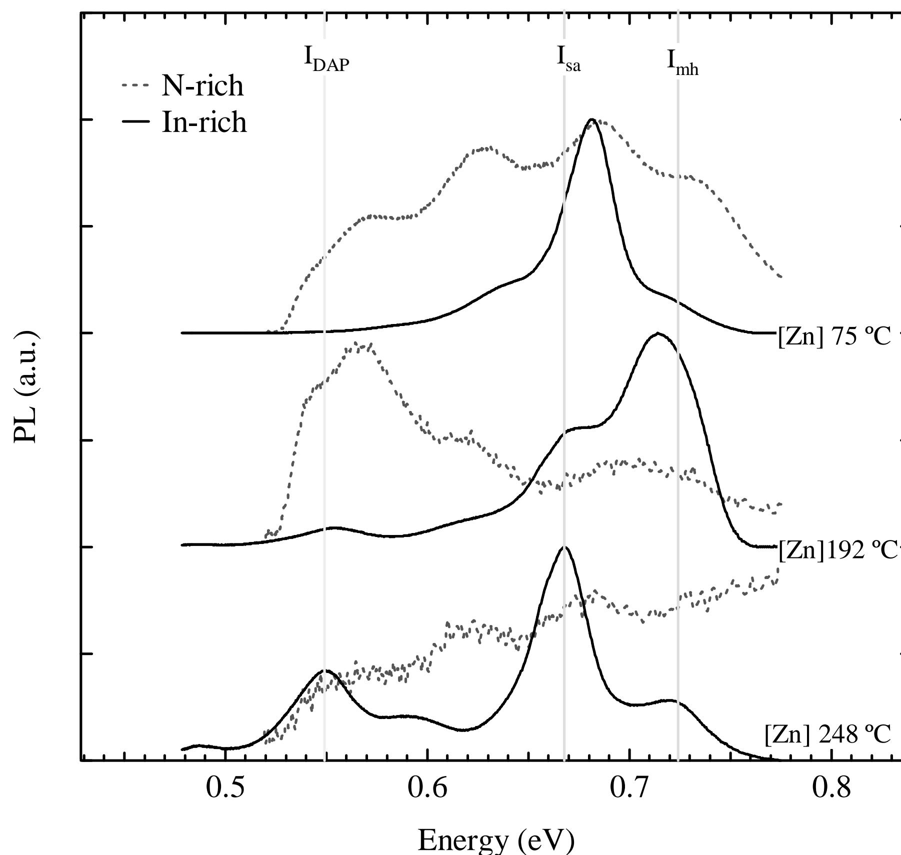

Figure 6.3 4 K PL of N- (gray dotted) and In-rich (black solid) InN:Zn/GaN.

assign the 0.72 eV peak to the Mahan exciton, involving transitions of free electrons in the Fermi sea level to a shallow acceptor bound state. The carrier concentration of this series increases as a function of Zn cell temperature. This naturally gives a rise to the Fermi edge and thus a Mahan exciton peak blueshifts[100,118] as displayed in figure 6.3. Conversely, the lower energy peak at 0.67 eV gradually redshifts as a function of Zn cell temperature. This behavior is attributed to a mixed procedure of the bandgap renormalization (BGR) and the potential fluctuation of donor and acceptor states as discussed in section 4.2. This means that a free-to-shallow acceptor approaches the midgap with increased doping level. As the Zn cell temperature is increased, PL reveals a number of low energy features peaking at 0.54 and 0.60 eV, and likely associated with residual deep acceptors. Perhaps, a single PL spectrum is insufficient to interpret the optical properties of InN:Zn. An extended PL analysis is certainly required to confidently identify the true origins.

As expected from the former InN:Mg series of chapter 4 and 5, the integrated intensity of the In-rich regime is a few orders of magnitude higher than that from N-rich films and the PL

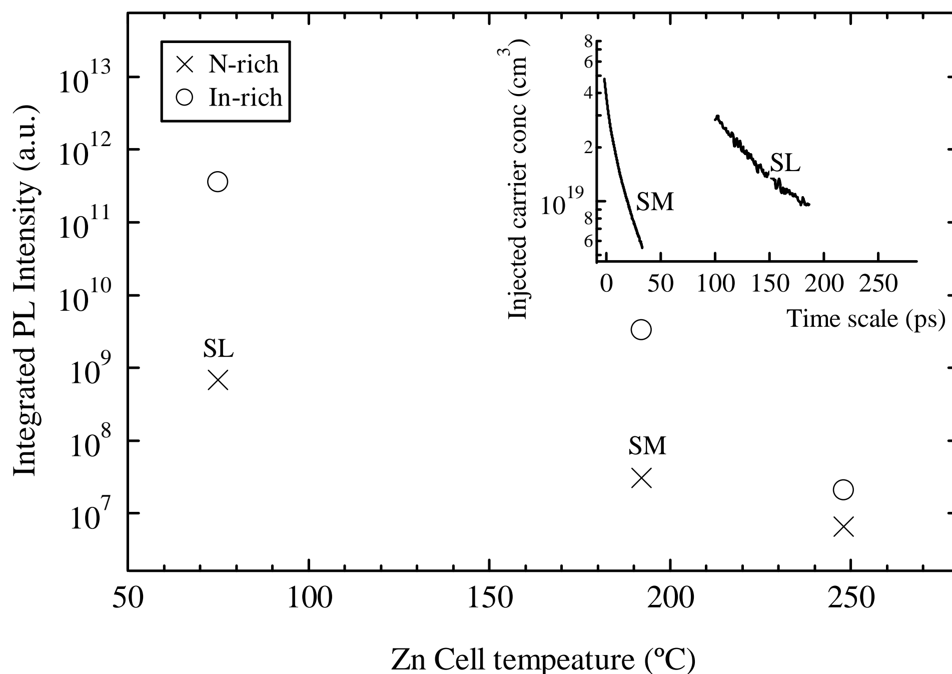

Figure 6.4 Variation of the PL intensity of InN:Zn/GaN with different Zn content The inset shows decay of the photogenerated carrier density according to TRDT measurement of selected samples at an injected density of 7.5×10^{19} cm^{-3} per pulse.

intensity decreases markedly with increasing Zn content for the both flux conditions as illustrated in figure 6.4. Again, the decay of photogenerated carrier density was performed by TRDT measurement and is shown in the inset of figure 6.4. A pump-probe technique was taken from N-rich films with doping temperature of 75°C (SL) and 192°C (SM). For SL, the decay exhibits a single exponential characteristic, while as a direct consequence of Auger recombination process, the decay time of SM is more rapid. This phenomenon is consistent with a N-rich InN:Mg/YSZ series as discussed in section 4.2.

More detailed PL study is required to ascertain the nature of luminescence. Figure 6.5 shows the PL spectra of 655-InN:Zn grown using a Zn cell temperature of 248 °C as a function of excitation intensity. As noted earlier, the origins of 0.67 eV and 0.72 peaks are likely a free-to-shallow (I_{sa}) and a Mahan exciton (I_{mh}). I_{sa} exhibits a pronounced blueshift as a function of excitation intensity due to the Moss-Burstein effect[29], whereas this effect is less relevant to I_{mh} since this PL emission is originated from the Fermi edge (rather than the CBM), where the band filling effect should be negligible[100,118]. A possible explanation of the lowest feature peaking at 0.54 eV is that the DAP transition (I_{DAP}) with increasing excitation intensity causing the strong Coulomb interaction and returns a blueshift. The 0.6 eV peak is more

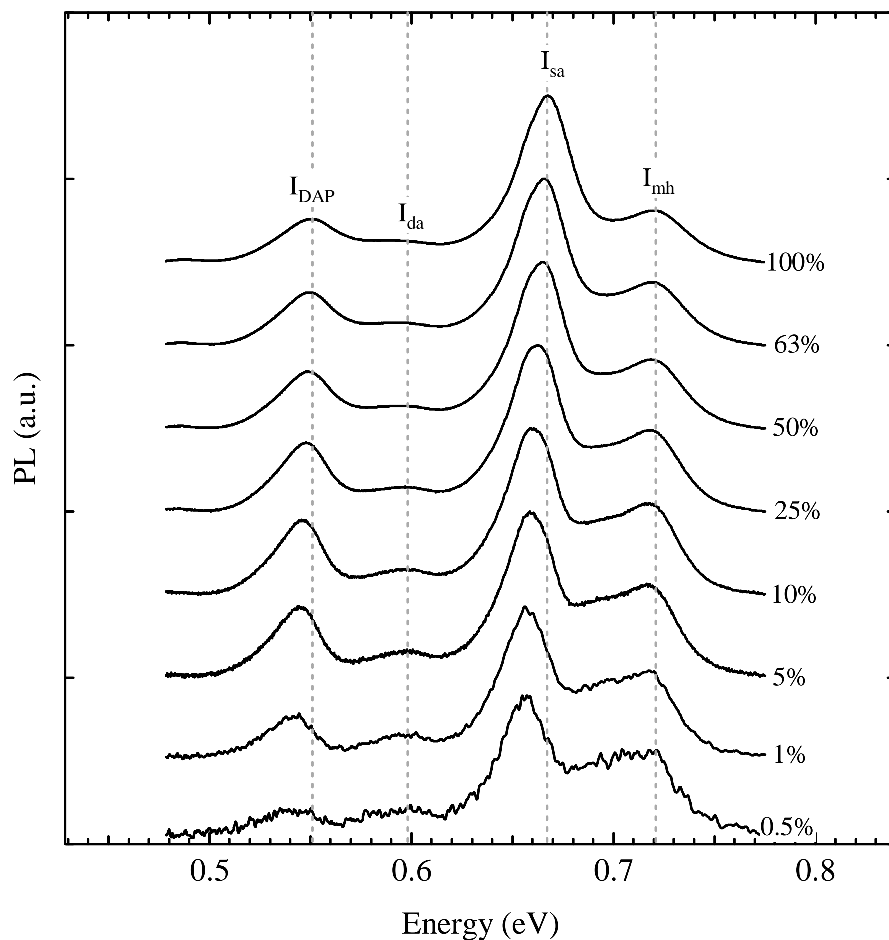

Figure 6.5 Excitation power dependent PL of the In-rich 655-InN:Zn film grown with a Zn cell temperature of 248°C (The features are normalized and offset vertically for clarity)

apparent at the low excitation intensity. This emission is pinned at the initial position, regardless of laser powers. As has been observed in the case of a N-rich InN:Mg/YSZ series, the expected blueshift of a free-to-deep acceptor transition is suppressed by a high background electron concentration of the material[91].

Additional information is determined by the power dependent PL as displayed in figure 6.6, where the intensity generally follows a power law $I \sim L^k$. This analysis supports the preliminary peak assignment as the power-law coefficients k being a sub-linear. Worth noting is the same returned value for the two very lower energy features of I_{da} and I_{DAP}. This points to the strong connection between two emissions, where the transitions of free electrons from the Burstein-Moss induced conduction band and electrons from a potential neutral donor state for I_{da} and I_{DAP}, respectively, radiatively recombine with hole at the same neutral deep

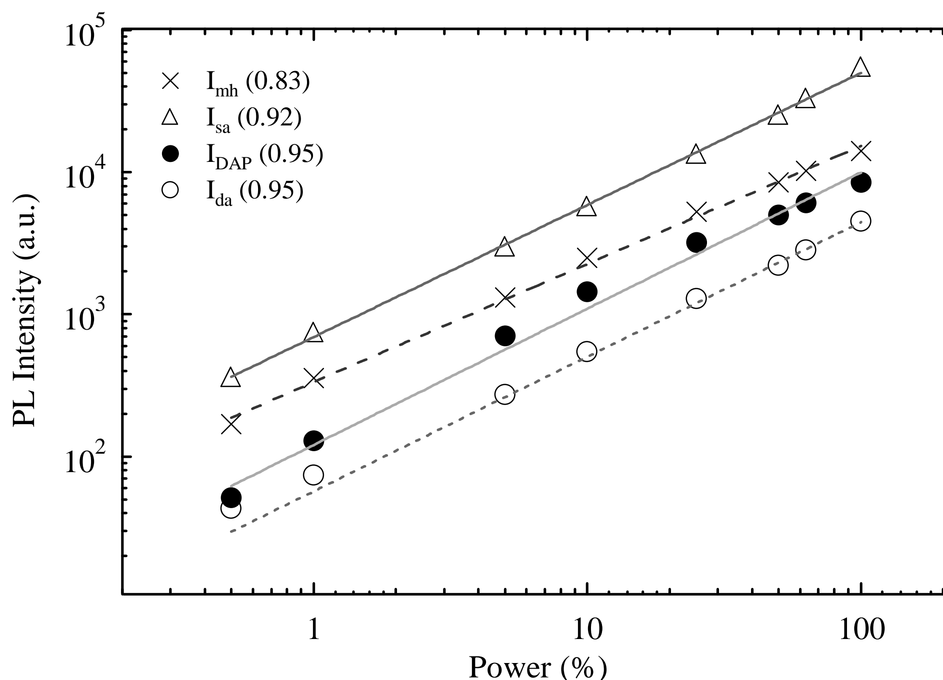

Figure 6.6 The fit of power law corresponds to determined components from the In-rich 655-InN:Zn/GaN sample.

acceptor state. Arguably, the energy separation between the two components is matched with the LO-phonon energy of 72 meV, though PL intensity of I_{DAP} surpasses I_{da}.

The PL spectrum was examined in more detail. The temperature dependent spectra are displayed in figure 6.7. The Mahan feature should not be strongly influenced by the bandgap shrinkage effect as expected from its originating state of the Fermi edge. The energy position of I_{mh} peak remained at the same position in the low temperature region but a slight redshift is noticeable at the highest temperature since the final recombination state should be nearby the VBM.

Both I_{da} and I_{sa} manifest temperature induced ‘S’ shaped’ energy shifts[40]. This behavior is also seen in both the N- and In-rich InN:Mg/(YSZ,GaN). An elevated temperature results in a primary blueshift in the peak I_{sa} until a threshold is reached, whereafter a gradual redshift is obtained, but vice versa for I_{da}. Since a combination of radiative process including: 1) the time dependent generation rate for the given transition, 2) the rate of electron (or hole) being captured, and 3) the activation energy of non-radiative centre, depend on the formation of localized states, these two contradictory trends are unsurprised to see[40]. I_{DAP} exhibits a less

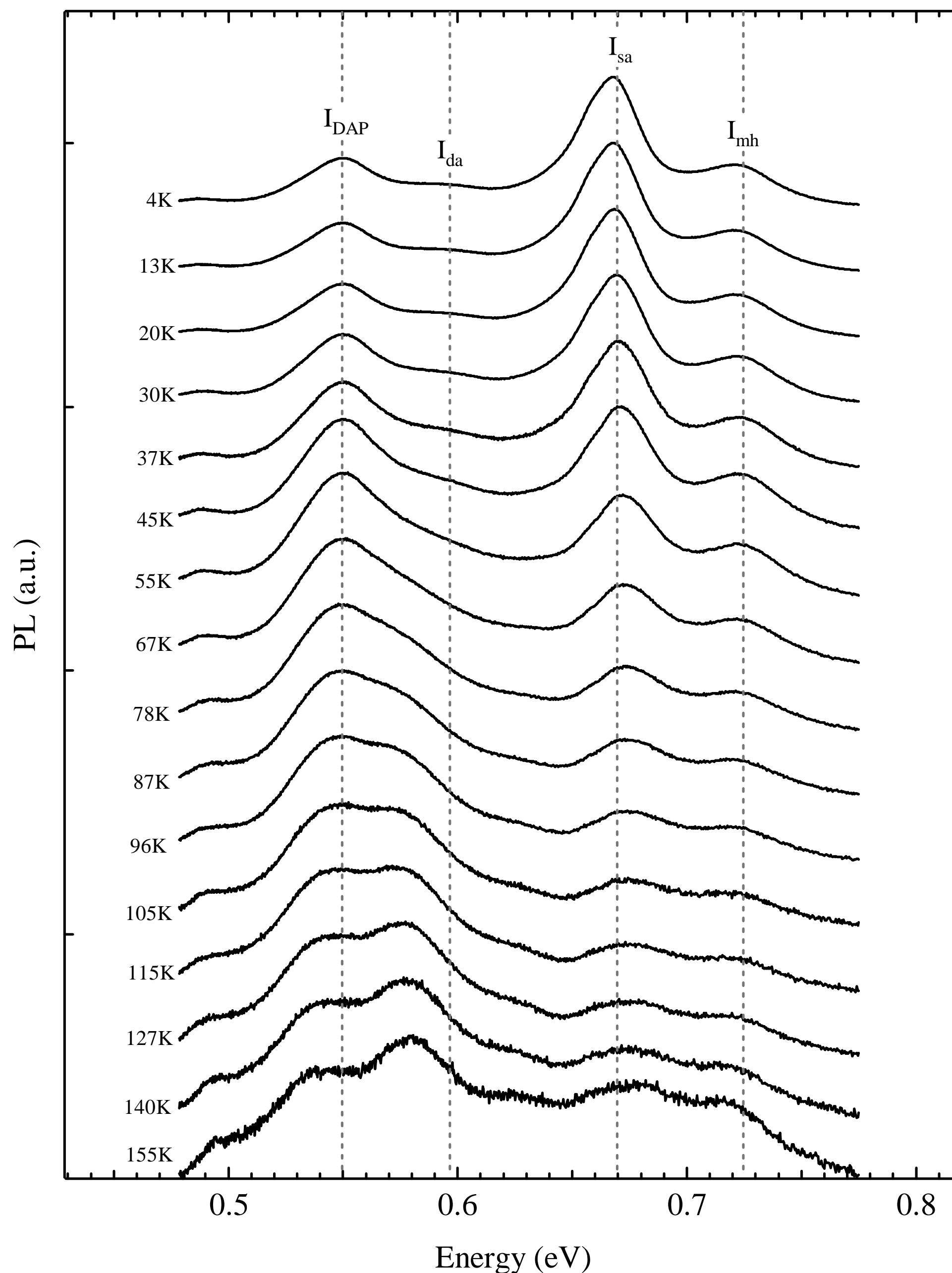

Figure 6.7 Temperature dependent PL of the In-rich 655-InN:Zn film grown with a Zn cell temperature of 248°C (The features are normalized and offset vertically for clarity).

amount of redshift with increasing temperature as expected from the thermal release of electrons from the donor state being transferred to its respective band (CBM)[215]. This DAP luminescence mechanism also results in the redistribution of PL intensity between I_{da} and I_{DAP}.

Both features have comparable intensity at 115 K. Also observed was that, the two emission peaks significantly emerge as a DAP transition changing its origin to a free electron-acceptor

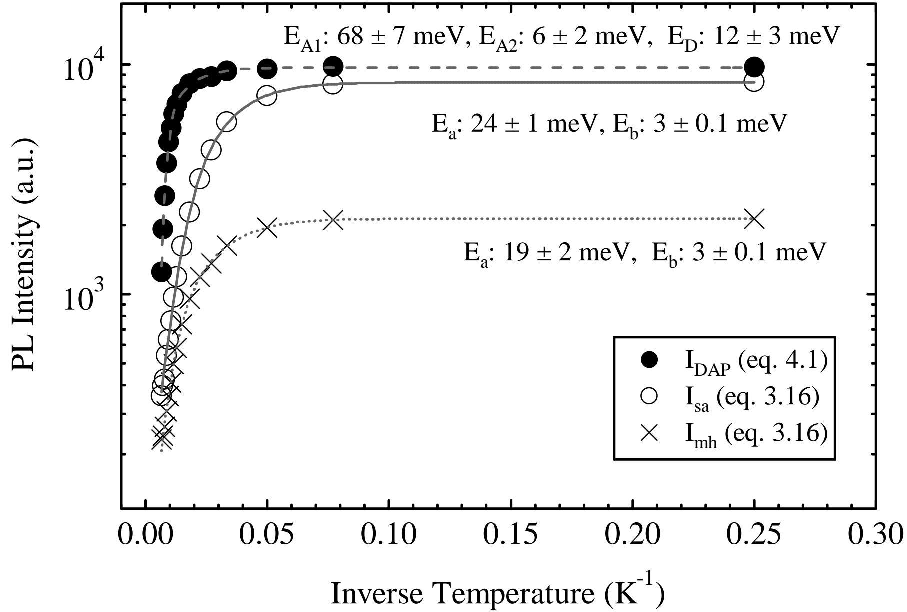

Figure 6.8 The Arrhenius plots of the absolute peak intensities for I_{DAP}, I_{sa}, and I_{mh} (offset vertically for clarity).

transition due to the low thermal dissociation energy of the shallow donor state[225]. More apparent PL intensities of the two lower energy features at high temperatures compared to the higher energy ones is owing to the redistribution of the localization states. As the temperature increases, a large distribution of carriers from the shallow acceptor states thermally excite to the deep acceptor states[90]. This behavior is consistent with the temperature dependent PL study of 590-InN:Mg/YSZ as discussed in section 4.3.

The intensity of each peak was extracted for an Arrhenius analysis and is displayed in figure 6.8. All Arrhenius fitting results were provided with two activation energies. These activation energies of E_a and E_b represent the non-radiative recombination channel of an acceptor state at the high temperature region and the thermal hole delocalization energy at the low temperature region, respectively. The 24 meV activation energy of I_{sa} matches well with an activation energy of shallow acceptor impurities reported for n-InN[90-92]. Meanwhile, a second activation energy of I_{sa} is only 3 meV. The rather low value of the thermal hole delocalization energy is owing to the non-radiative recombination channel of I_{sa} being nearby the VBM. Similarly, the return to equilibrium process of I_{mh} is associated with bandedge impurities which lie 19 meV above the VBM. The activation energy of the Mahan exciton in InN is less known and its nature is seldom mentioned elsewhere[209,210].

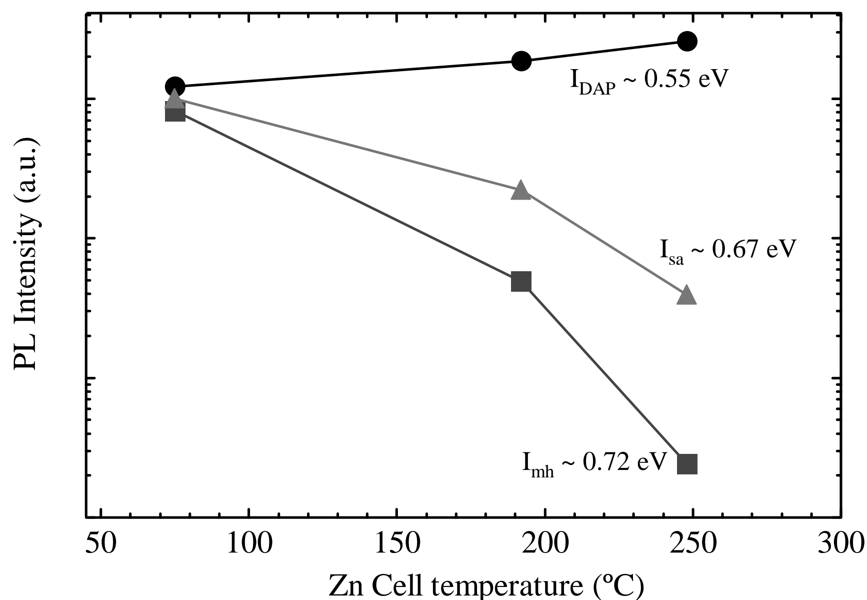

Figure 6.9 The absolute PL intensities of DAP, free-to-shallow, and Mahan exciton transitions as a function of Zn cell temperature.

The modified Arrhenius from equation 4.1 treated I_{DAP}. The activation energies of the non-radiative recombination channels yielded 68 and 12 meV for the deep acceptor and shallow donor levels, respectively. The activation energies of the donor and acceptor are in a vicinity of the reported a hydrogenic donor[133] and a deep acceptor (residual)[90,91] levels, respectively in n-InN. A deep acceptor activation energy of 69 meV for GaP:Zn is also noteworthy[211].

Seeing the multiple components, the question naturally follows whether the PL quenching effect applies to individual recombination processes. Relative PL intensities from each component have been plotted as a function of Zn cell temperature and are depicted in figure 6.9. The non-radiative recombination channels (E_A) of shallow neutral donor and deep neutral acceptor states have previously been increased as a function of Zn cell temperature. This means that both the neutral shallow donor and deep-acceptor bound states move further into the bandgap due to the greater amplitude of potential fluctuation upon increasing Zn content and leads to a redshift (approximately 7 meV) of I_{DAP}[222-224]. Correspondingly, a large number of donor-like impurities enhance the intensity of I_{DAP} slightly and more vibrant electron-electron scatter effect induces the PL line broadening effect with increasing Zn content[132,133,149]. Perhaps, a good example of this PL evolution is the effect of ion-bombardment of p-InN, which comprehensively discusses in Appendix C.

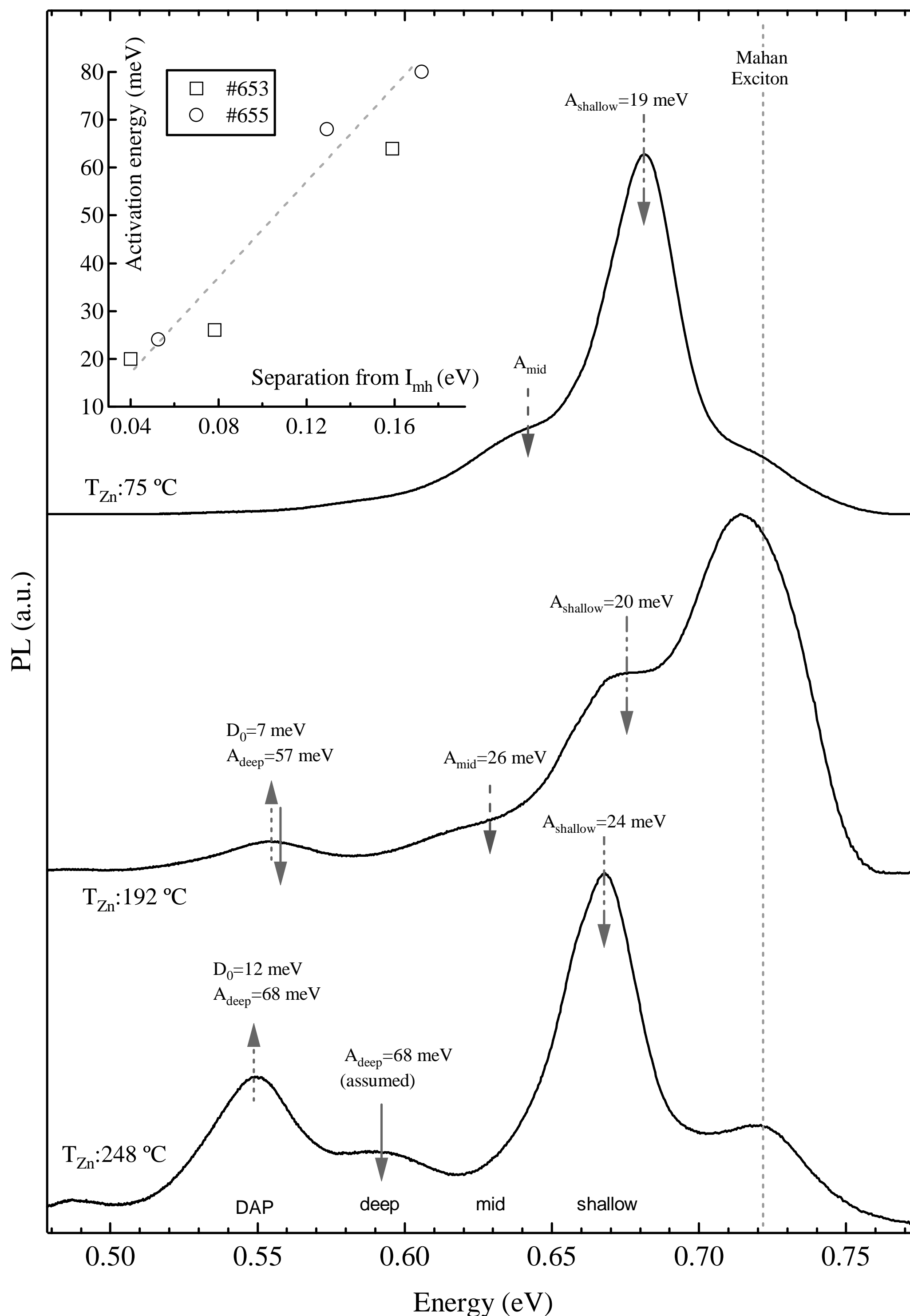

Figure 6.10 4 K PL spectra of In-rich InN:Zn/GaN. Positions of the thin headed arrows indicate the extracted activations from the designated transitions. The inset shows the activation energies correspond to localization states (For DAP, two activations energies of donor and acceptors were added).

Meanwhile, I_{sa} and I_{mh} quench in the usual manner as a function of Zn cell temperature. This concludes that Zn doping in these samples incorporates into either the interstitial In site (introducing native point defects)[231-233] or the complex arrangement of Zn-H[129,130,133], where both cases can considerably increases the background electron concentration.

Finally, the absolute PL energy separation from spectra accurately matches with the extracted activation energy respect to the VBM. In figure 6.10, the PL spectra of In-rich InN:Zn is displayed and each peak is designated with their activation energies (from Arrhenius plots). Worth noting is that the difference between individual activation energies are proportional to the absolute energy separations. For clarity, a plot of activation energy versus localization energy is shown in the inset of figure 6.10. The fitted activation energies lie on a straight line with a slope of 0.95, suggesting that these peaks should be all connected in some fashion by neutral bound acceptors.

6.1.3 Brief summary of Zn-doped InN

The electrical and optical properties of InN:Zn/GaN has been investigated. InN thin films are doped with Zn over a concentration range of several orders of magnitude, under both In- and N-rich growth conditions. SFH measurements are somewhat restricted due to the existence of a degenerate electron accumulation layer. Analysis of p-type doping using Zn has therefore been constrained to VFH, although the hole-mediated feature still remained vague. PL characteristics are also typical of overall n-type doping. Not so surprisingly, the quantum efficiency is drastically quenched upon Zn for both flux conditions but these films can exhibit a wide range of spectral features between 0.5 and 0.7 eV. A donor-acceptor pair, deep acceptor, shallow acceptor, and Mahan exciton are presented in decreasing energy order. This spectral morphology is similar to what is observed with GaN:Zn, where multi-radiative pathways including a DAP are present[182,183]. In this series, a donor-acceptor pair transition involves residual deep acceptors and shallow donors. The latter may be originated from the interstitial In or Zn-H complex with a range of activation energy of 7 - 12 meV. The extracted deep and shallow acceptor activation energies are in a range of 57 - 68 meV and 19 - 24 meV, respectively, which are in good agreement with the reported residual acceptors in n-InN[90,91]. The values of activation energies of the relevant transitions are correlated to the PL energy

position. Interestingly, the intensity of I_{DAP} is slightly enhanced as a function of increasing Zn content, while other components are strongly quenched. This implies the introduction of point defects and inhibits Zn incorporation as an acceptor.

6.2 Manganese doped InN; a potential dilute magnetic semiconductor

The alternative dopants such as Zn and Be[212] certainly have provided a plentiful fundamental roadmap for p-InN and enabled a better understanding regardless of whether (p-type is) successful or not. The realization of a p-type bulk layer has not been discovered from either dopant and are inferior to that of the most viable dopant, Mg. Work continued in this area by looking at a different aspect of InN doping associated with ferromagnetism.

Ferromagnetic materials in the context of dilute magnetic semiconductors (DMS) are of interest in spintronics[187]. The transition metals such as Manganese (Mn) and Chromium (Cr)[202] can be utilized for a spintronic based material as a dopant. The majority of initial DMS studies have focussed on HgTe and (Ga,In)As. Despite some success in determining that Mn can be used to realize the ferromagnetic property, a few relevant issues stop them being commercialized[188,189,194]. Not only the operation required an enormous applied magnetic field but their Curie temperature below 300 K was the key restriction for the application[190,191].

In a 2001 ab-initio electronic-structure calculation by Yoshida and Sato[213] proposed that these difficulties can be resolved by III-N semiconductors. Their work plausibly predicted the room temperature ferromagnetism of (In,Ga)N:Mn without much need of external magnetic field[192,193,197-199] (figure 6.11). After this breakthrough, Dietl *et al.*[196] successfully demonstrated a potential hole-mediated ferromagnetic property of (In,Ga,Al)MnN in the same year. Also reported by Pearton *et al.*[195] in 2003 was that Mn can be incorporated into a substitution arrangement of Mn^{2+}, although this configuration strictly requires the specific Mn mole fraction range of 0.01 - 0.1%.

Unfortunately, only a limited number of reports discuss p-(In,Ga,Al)MnN and has thus far contributed to the current poor understanding. The main reason for the lack of reports

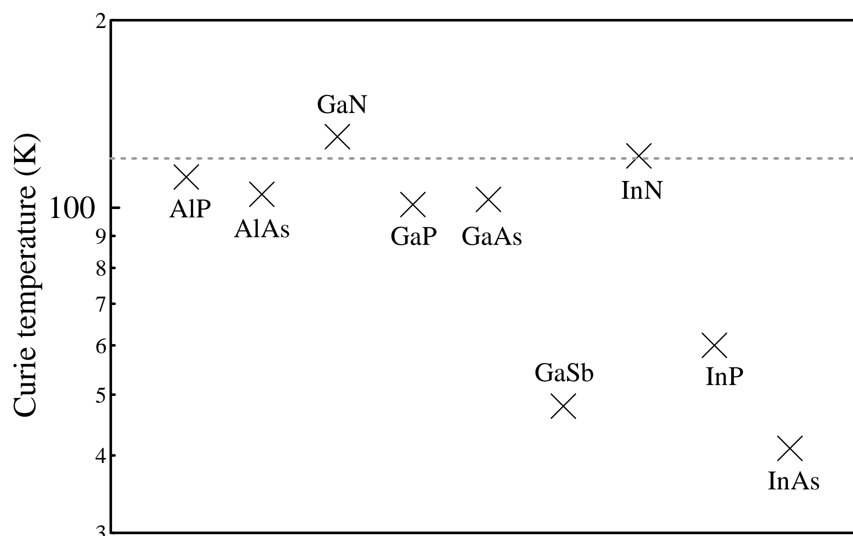

Figure 6.11 Extracted Curie temperatures for a wide range of III-V semiconductors grown with a targeting Mn mole fraction of 5% [196].

detailing the central property is that it is very hard to maintain p-type doping in these systems while also incorporating large fractions of Mn. Considerably more rigorous effort should be applied to growth and characterization of III-MnN. With the emphasis on extending the knowledge of ferromagnetism in InN, an investigation of p-InMnN is examined in this thesis. The study not only considers details of electrical properties but also the optical treatment is comparatively analysed for the first time.

6.2.1 The growth parameters and electrical properties.

Growth, SEM, and SFH by Dr. Jessica Chai at University of Canterbury

SIMS and XPS by Mr. Wojtek Linhart at University of Warwick

VFH by Prof. Thomas Myers at Texas State University

The growth parameter was carried out in a similar manner to previous series (*ie*. In cell and substrate temperature of 760 and 450 °C, respectively). The InN:Mn thin films were grown by a Perkin Elmer 430 molecular beam epitaxy system on Ga-polar GaN:Fe templates/sapphire and thickness of 1000 nm were obtained. The Mn was evaporated using a conventional 2 cc effusion cell. The Mn cell temperature was varied between 512 °C and 687 °C to match a Mn mole fraction between 0.001 % and 1 % for both the N- and In-rich zones. The extracted SIMS Mn concentration was evenly distributed in a concentration range

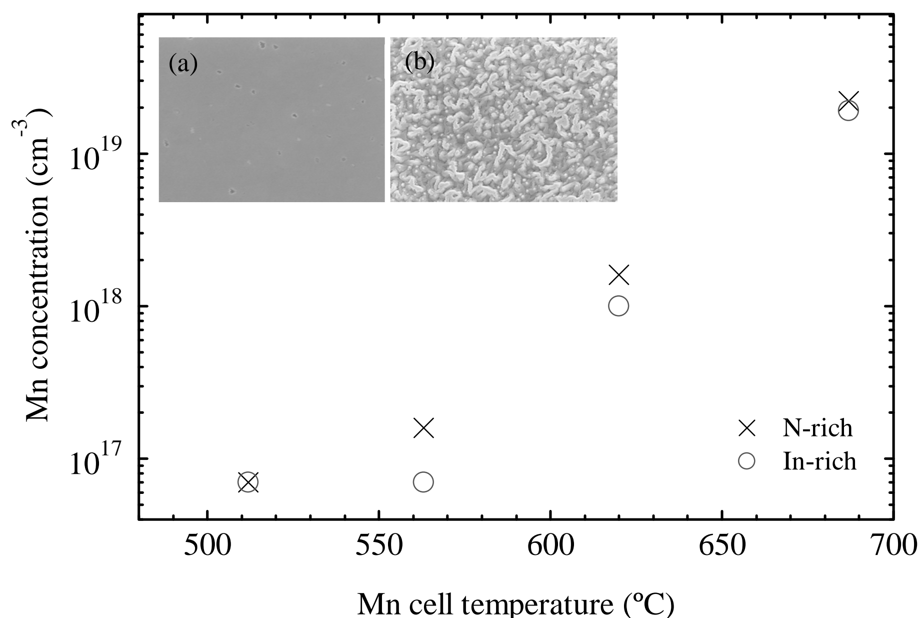

Figure 6.12 SIMS Mn concentration of an InN:Mn/GaN series as a function of Mn deposition source temperature. The inset shows SEM images of the In- (a) and N-rich (b) InN:Mn/GaN films grown with a Mn cell temperature of 563 °C.

of 10^{17} - 10^{19} cm^{-3} and is illustrated in figure 6.12. Our results show that the complete sticking of Mn on InN/GaN is slightly better in the N-rich regime and this situation perhaps significantly improve the surface morphology of N-rich surface as evidenced from the SEM images in the inset of figure 6.12. This phenomenon is in sharp contrast to the earlier results of InN:(Mg,Zn), although this trend is often seen from a p-type GaMnN epilayers[200].

The standard Hall effect measurements were performed at room temperature and the results shown in figure 6.13. In SFH measurement, the greater Mn content results in higher electron concentration and mobility, regardless of flux conditions. Also observed is a significant drop of resistivity as a function of Mn content as shown in the inset of figure 6.13. In this this series, an optimum of “low-defect” is recognized for the sample grown with a Mn cell temperature of 563°C, which corresponds to the ‘critical’ Mn mole fraction of 0.01% (for III-V semiconductors) as discussed in a previous section[192,194,195,200,201].

VFH measurement was employed to further understand the bulk property. The magnetotransport measurement of the In-rich films only indicated electron conduction, whereas the N-rich InMnN sample grown with a Mn cell temperature of 563 °C (Mn mole fraction of 0.01%) returned a hole-mediated feature according to QMSA in figure 6.14 (a). A

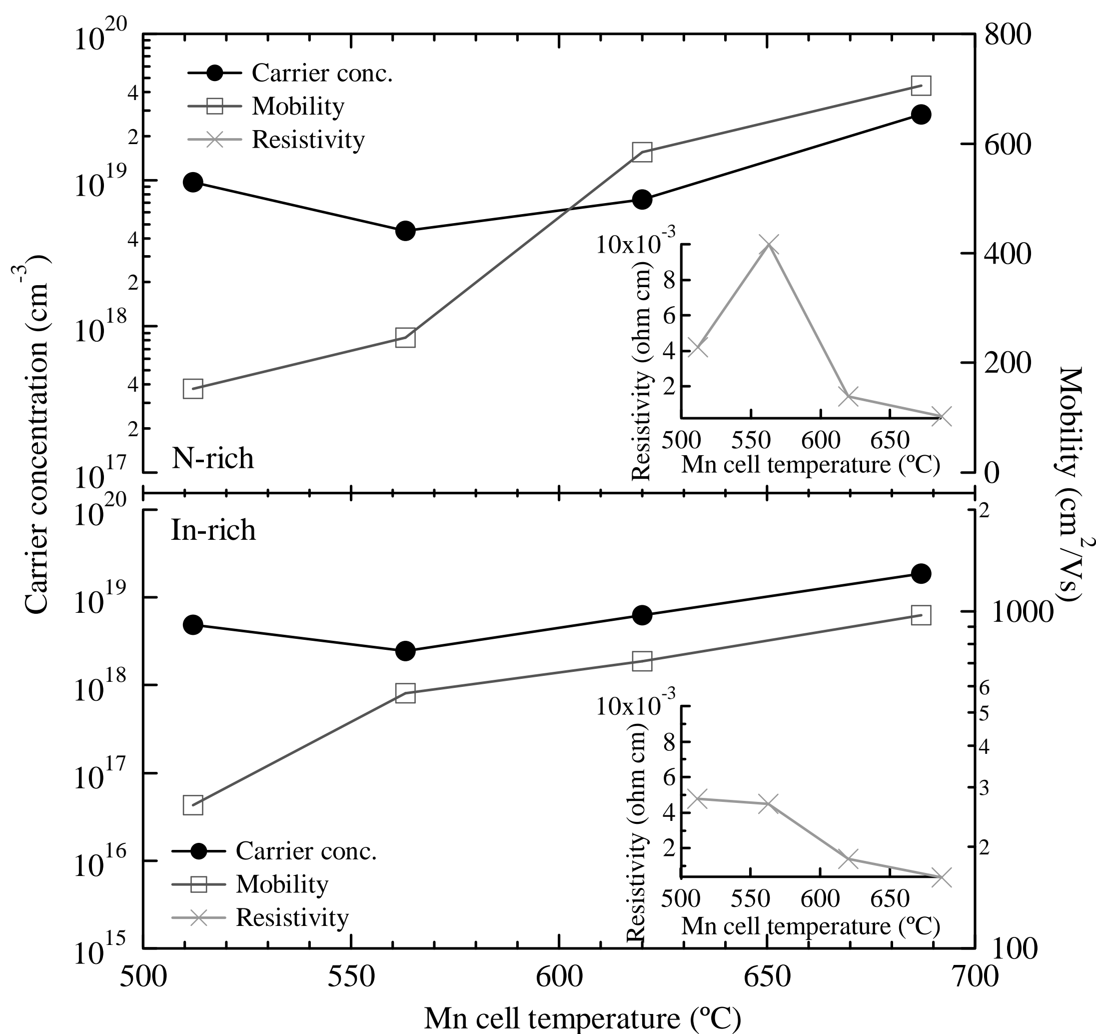

Figure 6.13 SFH electrical properties of a N- (top) and In-rich (bottom) InN:Mn/GaN series as a function of Mn cell temperature.

wide spread of hole mobility represents multiple hole conducting paths, which is of interest in a potential p-type InMnN[208]. This observation parallels X-ray photoemission spectroscopy (XPS) measurement, where the surface Fermi energy points to the minimum value of 1.15 eV (respect to the VBM) at the critical Mn cell temperature of 563 °C as shown in figure 6.14 (b). This view implies that the Mn is successful in lowering the E_F, which is a strong indication of the background electron compensation. Outside of this critical Mn cell temperature of 563 °C, a p-type bulk layer cannot be found and correspondingly the surface E_F give intrinsic value of 1.4 eV[67,68], suggesting too much Mn can lead to the onset of n-type. The summary of Hall effect measurements are listed in table 6.2.

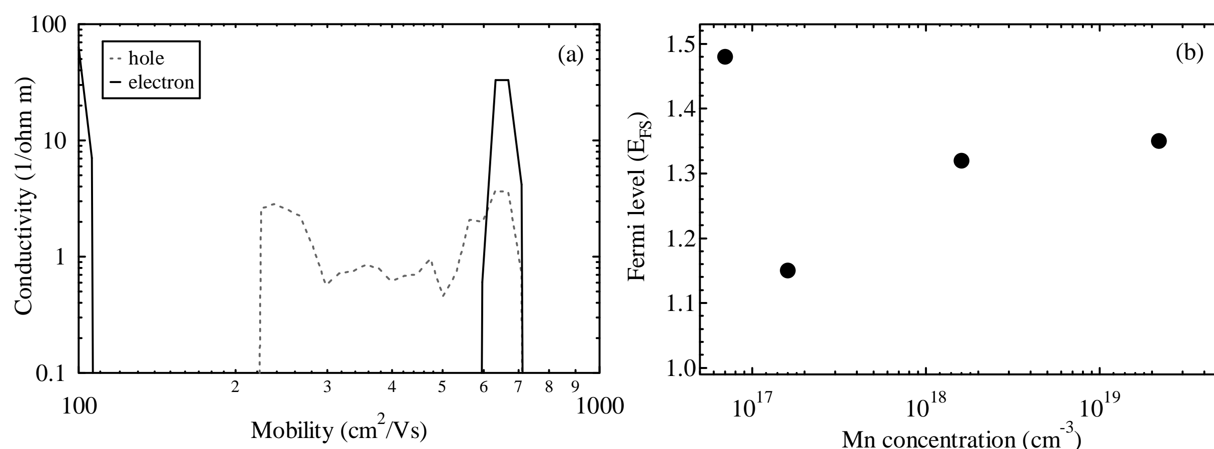

Figure 6.14 (a) QMSA spectrum of InN:Mn/GaN film grown with a Mn cell temperature of 563°C under N-rich condition. (b) Valence band edge XPS data for N-rich InN:Mn/GaN films with respect to the surface Fermi level as a function of Mn concentration.

Table 6.2 A summary of growth conditions and Hall effect measurements of Mn doped InN/GaN films.

# Films (N-rich)	T_{Mn} (°C)	Mn_{conc} (cm^{-3})	n (cm^{-3})	μ (cm^2/Vs)
723 (N-rich)	512	7.0×10^{16}	9.67×10^{18} (2.66×10^{18})	153 (339)
724 (N-rich)	563	1.6×10^{17}	4.51×10^{18} (8.51×10^{17})	246 (605)
725 (N-rich)	620	1.6×10^{18}	7.37×10^{18} (4.36×10^{18})	584 (779)
726 (N-rich)	687	2.2×10^{19}	2.81×10^{19} (1.32×10^{19})	705 (1036)
# Films (In-rich)				
723 (In-rich)	512	$< 7.0\times10^{16}$	4.91×10^{18} (1.63×10^{18})	266 (226)
724 (In-rich)	563	$< 7.0\times10^{16}$	2.44×10^{18} (2.17×10^{17})	570 (551)
725 (In-rich)	620	1.0×10^{18}	6.26×10^{18} (2.41×10^{18})	709 (386)
726 (In-rich)	687	1.9×10^{19}	1.88×10^{19} (1.49×10^{19})	972 (1003)

Note: Parentheses indicates the VFH measurement. N → carrier conc., μ → mobility

6.2.2 Optical properties of InN:Mn/GaN

PL of samples measured from both N- and In-rich InN:Mn was performed at liquid helium temperature using a 808 nm line diode module laser and an InSb detector. The output power of this excitation source is 250 mW. As illustrated in figure 6.15, the PL evolution of In-rich

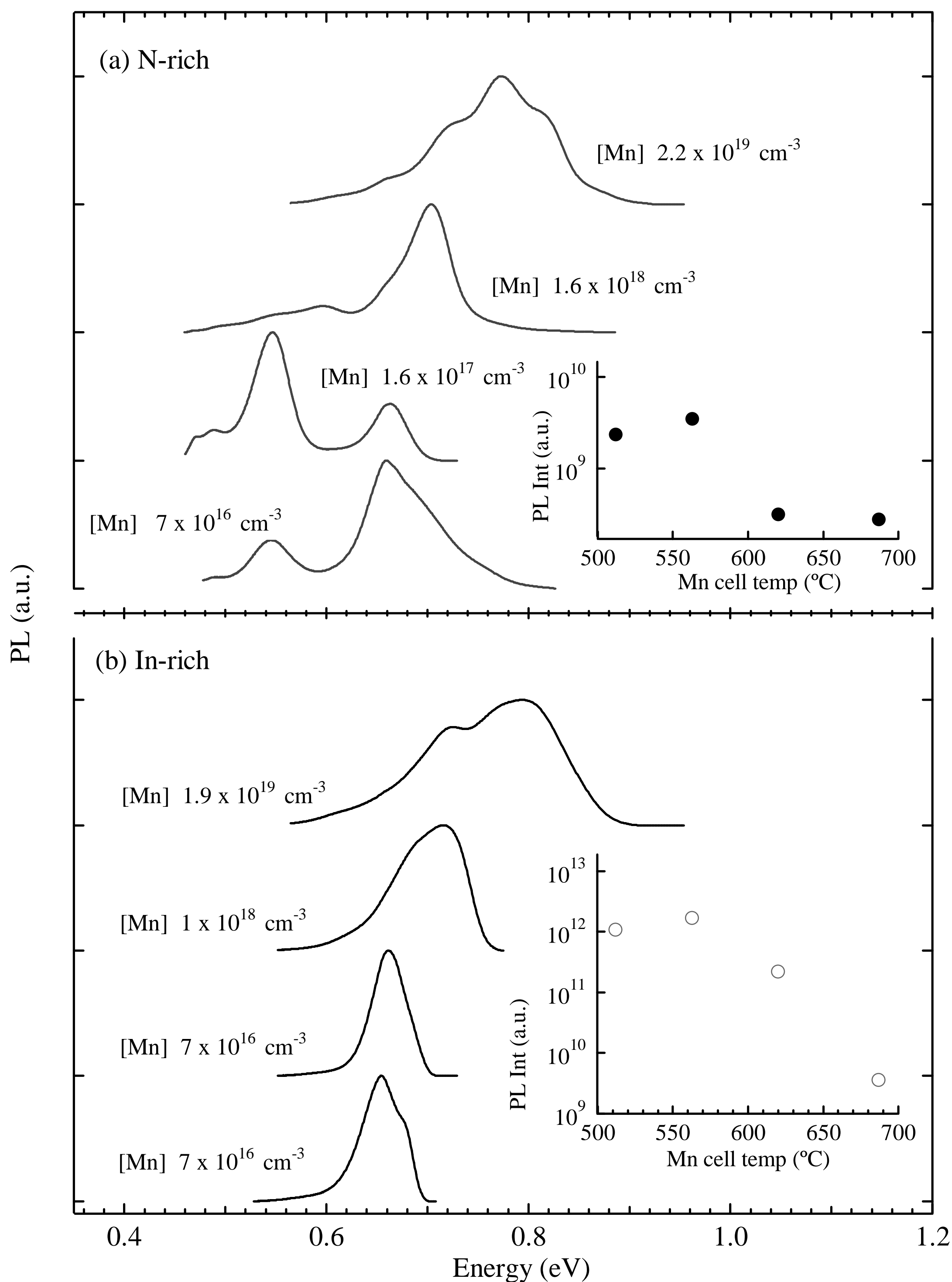

Figure 6.15 4 K PL spectra of N- (a) and In-rich (b) InN:Mn/GaN. The insets display variation of the PL intensity of InN:Mn/GaN with different Mn cell temperature.

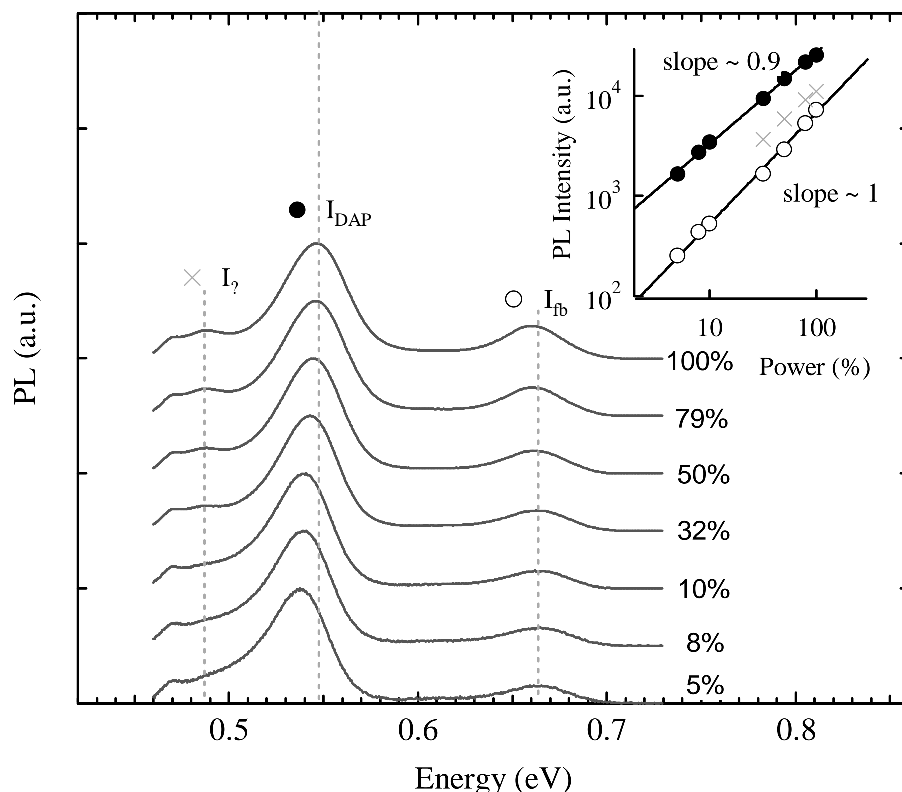

Figure 6.16 Power dependent PL of the N-rich 724-InN:Mn/GaN film grown with a Mn cell temperature of 563°C (the features are normalized and offset vertically for clarity). The inset shows the log slope of three different components by using a power law equation.

zone samples exhibits a typical n-type characteristic as evidenced from a combination of the PL line broadening (containing multi overlapping components) and the Moss-Burstein effects (blueshift) as a function of Mn concentration[29].

Meanwhile, the PL of lightly doped films in the N-rich regime exhibit distinct structure. Worth noting is the PL configuration of the sample grown with the Mn cell temperature of 563 °C (Mn mole fraction of 0.01%) showing a dominant low energy feature at 0.54 eV, which is an unusual case for InN. This feature is a credible candidate to be Mn-related as expected from the VFH and XPS measurements. As the Mn concentration is further increased, the high energy PL feature blueshifts, and multiple features are obtained.

As displayed in the inset of figure 6.15, commonly observed was a noticeable reduction in PL intensity as a function of Mn concentration, regardless of the flux conditions and is attributed to the Auger recombination. As always has been the case, In-rich InN:Mn films produced more efficient light comparing to those from N-rich zones throughout a wide range of Mn concentration range.

The PL properties were characterized in more detail. Figure 6.16 displays the power dependent PL spectrum of N-rich 724-InN:Mn/GaN that has a the critical Mn mole fraction of 0.01%. Two strong luminescence features are peaking at the 0.66 and 0.54 eV. A lower energy feature exhibits a profound blueshift as a function of excitation intensity, while a higher energy features slightly redshifts. The latter may be caused by the laser heating as the power is increased (note: as discussed earlier, the excitation source used in this series is much more intense compared to other series reported in this thesis).

Considering its low energy position of 0.54 eV, this peak arises from transitions of donor-acceptor pairs (I_{DAP}). The blueshift is therefore attributed to the electrostatic Coulomb interaction. The peak 0.66 eV is typical of free-to a shallow bound state transition (I_{fb}). Correspondingly, sub-linear power dependences are evidence for the both peaks. A 0.49 eV peak can be determined by a careful analysis. As the excitation increases, a clear blueshift is seen and the extracted power-law exponent k value is consistent with nearby transitions. The energy separation between the two lowest peaks is only 60 meV, which rules out the possibility of LO-phonon-replica. A genuine physical origin of this peak is still unknown.

Additional information can be gained from a temperature dependent PL study and is displayed in figure 6.17. Both PL features redshift with increasing temperature as they follow the bandgap narrowing. It is interesting to note more apparent I_{fb} peak at high temperatures. This observation is due to the fact that the intensity of I_{DAP} decreases more rapidly than the I_{fb}, which is a typical nature of DAP transition as discussed in section 6.1.2. Moreover, the energy separation between I_{DAP} and I_{fb} is too far apart (~130 meV) that thermally excited carriers from I_{fb} is difficult to contribute the population of a deep acceptor state of DAP centre (*ie*. a lower energy PL normally becomes a dominant at 300 K due to the thermally excited carriers from a higher energy feature, if the formations of two acceptor states are close enough).

As shown in the inset of figure 6.17, the intensity of each peak was extracted for Arrhenius analysis. A typical shallow acceptor activation energy of 11 meV (E_a) is given for I_{fb}. The non-radiative recombination channel is very close to the VBM that a thermal hole dissociation energy (E_b: 1 meV) is rather weak. The extracted activation energy of I_{DAP}, yield 91 and 35 meV for the activation energies of a Mn deep acceptor and shallow donor sites,

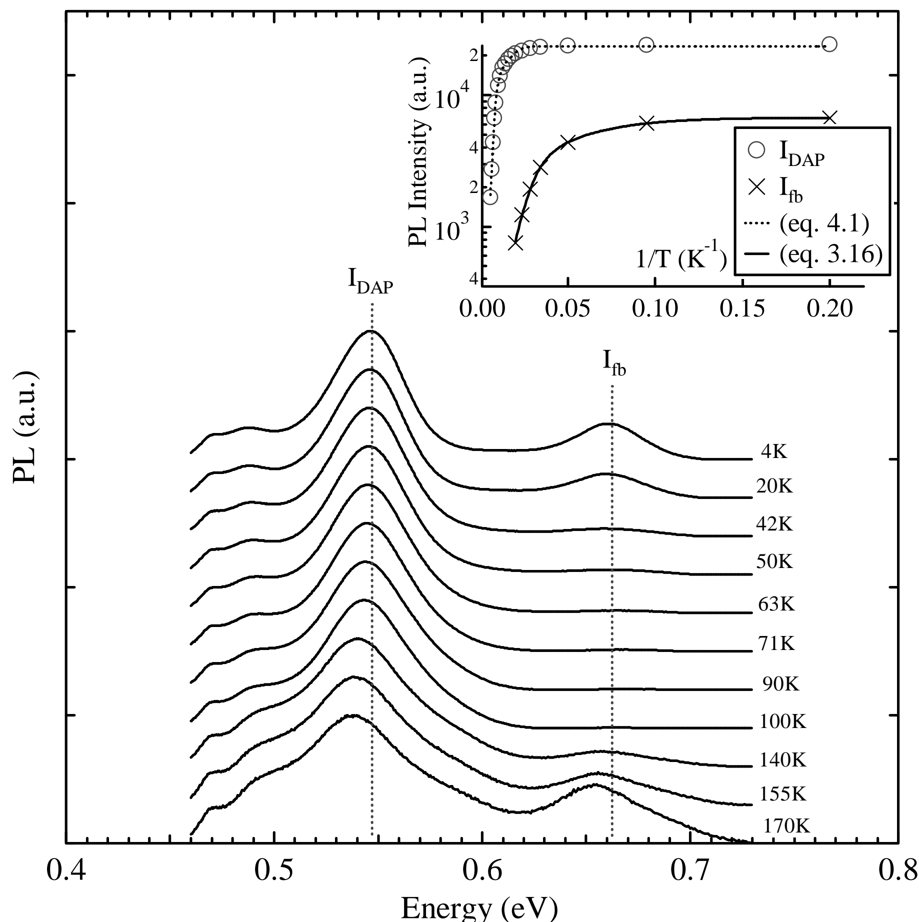

Figure 6.17 Temperature dependent PL of the N-rich 724-InN:Mn/GaN with a Mn cell temperature of 563°C (the features are normalized and offset vertically for clarity). The inset shows the Arrhenius plots of the absolute peak intensities for I_{DAP} and I_{fb}.

respectively (eq.4.1). The extracted Mn energy of 91 meV is reasonably similar to Mg activation in InN[75,92,127,133]. This observation is also in good agreement with GaN:Mn studies, where the substitution arrangement of Mn^{2+} was discovered for the samples grown within the Mn mole fraction of 0.01%, where Mn acted as a deep acceptor[194,195].

The E_{A2} (10 meV) represents the hole dissociation energy and its value matches well with the extracted value of 14 meV observed in Mg-doped InN/GaN in chapter 5 (a Mg-related emission in figure 5.13). Seemingly, an acceptor dopant (Mg or Mn), which correlates to a 'p-type-related deep acceptor state gives a large value of the hole dissociation energy (E_{A2}) in some extent. Another interpretation is the Coulomb interaction between electrons and holes may contribute a strong ionization energy as discussed in section 3.3. In the context of InN:(Mg,Zn), the physical origin of donors were the hydrogen induced complex, having an activation energy range of 7 to 12 meV. However, the rather high value of the donor

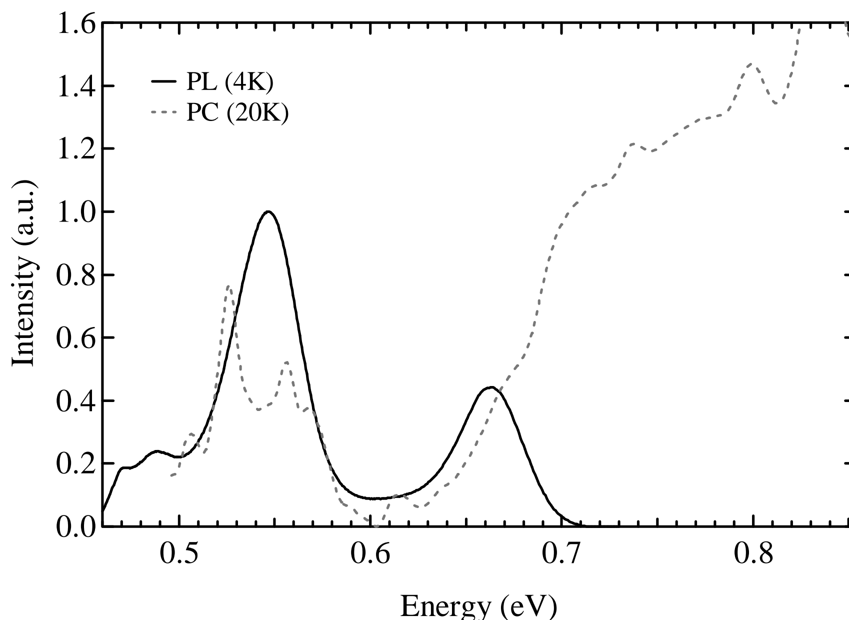

Figure 6.18 The PL and PC signals from N-rich 724-InN:Mn/GaN at 4K and 20K, respectively. A xenon lamp was used for an excitation source and the applied current was 54mA (closed cycle system).

activation energy of 35 meV observed here in InN:Mn disagrees with such an interpretation. Perhaps, the high donor activation energy is the reason why the I_{DAP} transition is relatively strong and does dominate the total PL as discussed in figure 6.9.

The extended evidence supporting the nature of a lower energy feature is valid from a photoconductivity (PC) measurement. A xenon lamp was used for an excitation source and the applied current was 54 mA. The closed cycle system allowed bringing temperature close to 30 K.

Figure 6.18 shows the simultaneous plot of PL and PC spectra of 724-InN:Mn. Despite the signal-to-noise ratio being rather poor, the correlation between features of the photo-current and PL can be recognized. Worth noting is a midgap photocurrent roughly peaking at the same position as I_{DAP} (PL). This onset is a manifestation of the electron-hole pair as reported in detailed studies of PC in InAs[204-206].

6.2.3 Brief Summary of Mn-doped InN

A series of Mn-doped InN films has been grown with Mn concentration varied over three orders of magnitude. In VFH, a clear evidence of hole mobility is seen for the sample grown

with a Mn mole fraction of 0.01% and correspondingly the surface Fermi level is significantly lowered. In PL, this particular film exhibits an unusually strong low energy feature peaking at 0.54 eV. The extracted Mn activation energy is 91 meV, consistent with Mg activation energy in InN as an acceptor. Also observed is a blueshift with excitation power, which is a strong representative of a DAP nature. Further work is required to clarify the genuine physical origin of the donors. Its high activation energy of 35 meV is not consistent with potential donor candidates reported in III-Nitrides.

Worth noting is that a similar low energy feature is observed from the sample grown with a Mn mole fraction of 0.001%, although the VFH measurement cannot detect a p-type bulk layer. The likely reason is that the Mn concentration of such film too low to compensate the background electron concentration. As always has been the case, overdoping with Mn increases the carrier concentration and desired substitution of Mn^{2+} cannot be formed. The Mn acceptor level is only found for a Mn mole fraction of 0.01% under N-rich flux, whereas typical n-type characteristics are determined from other Mn concentrations and under In-rich flux conditions. This phenomenon parallels with GaN:Mn studies[195-199]. This concludes that Mn can act as an acceptor in InN with a rigorous control of acceptor concentration.

Chapter 7

Conclusion and Future research

7.1 Key results of Mg-doped InN

A systematic study of InN epilayers with trace amounts of dopants has been undertaken via electrical and optical studies, with most attention paid to the latter. PL measurement has been a critical part of the research. This analysis has drawn significant evidence of a genuine optical property of acceptor doped InN and has successfully provided a fruitful path for the development of p-InN.

Of the acceptor candidates, Mg doping was considered a priority, by benchmarking a family alloyed material of p-GaN. All Mg doped InN thin films used in this study were grown by plasma-assisted molecular beam epitaxy (PAMBE). The central property of the material was strongly connected to the specific relative fluxes (Mg and In), substrate choices, and use of buffer layers.

YSZ substrate is the closest lattice matched to InN and was an initial preference for this research. As a direct consequence of the surface electron accumulation layer, single magnetic field Hall effect (SFH) measurements were somewhat perturbed by ‘heavy’ donor-like defects and many of useful electrical parameters were inaccurately drawn. The SFH electron concentration values were clustered at 10^{19} cm^{-3} without any particular patterns, and the rather low value of mobility was also insensitive to Mg content.

The surface electron accumulation layer is still the ongoing issue for InN and many potential solutions to overcome this effect are offered. Chief among them, the most realistic approach is the employment a GaN capping layer. This effect can sufficiently terminate many of the 'unwanted' local impurities at the InN surface by precluding external species such as hydrogen and oxygen, which exclusively act as donors. A main hurdle however, is the discernible difference in growth temperature between InN and GaN.

Photoluminescence (PL) measurements have drawn significant interpretation regarding p-InN. PL of N-rich InN:Mg/YSZ generally consisted of asymmetric broad single peak. The effect of Mg pushed the acceptor bound states deeper into the gap from the valence band. This phenomenon resulted from a mixture of the bandgap renormalization (BGR) and the potential fluctuations of electrons and holes. Such an interpretation initially referred to the background electron concentration increasing as a function of Mg content.

A potential Mg related deep emission centre at 0.65 eV was eventually realized from a sample grown with a Mg cell temperature of 220 °C and this conclusion was tentatively drawn by the extracted activation energy from the Arrhenius being close to the reported Mg activation energy in InN. As the Mg concentration further increased, a DAP transition peaking at 0.6 eV was observed with a LO-phonon replica 72 meV lower energy. The DAP transition involved a shallow neutral donor bound state and a residual deep acceptor bound state with the activation energies of 10 and 37 meV, respectively. In the excitation intensity dependent PL, this transition considerably shifted to blue as the intensity increased due to the electrostatic Coulomb interaction. Heavy Mg doping of InN reduced a deep acceptor activation energy, since a large number of ionized acceptors were attracted by holes in the valence band. Donors (in DAP) were likely originated from either the Mg-H complex or interstitial In, which can increase the background electron concentration and possessed the 'heavy' n-type character.

Integrated PL intensity was monotonically decreased as a function of the Mg concentration. In time-resolved differential transmission (TRDT) measurements, bi-exponential decay was in evidence for the heavily doped films, which is not an 'ideal' recombination dynamic of n-InN. Thus our conclusion was that the commonly reported PL quenching effect upon Mg is in fact due to the onset of trap-assisted Auger. This finding is expected to have significant impact on the device applications of group III-nitrides. If Auger is the true origin of

unexpected quenching of the PL, its intrinsic character cannot be simply removed. Alternately, the potential fallback is reducing the carrier concentration of the material. Under this circumstance, the Auger's impact is likely minimized.

A selection of In-rich growth was part of a larger program investigating Mg doping in InN, and both the electrical and optical properties of InN:Mg/GaN markedly improved. The effect of Mg in this series significantly lowered the carrier concentration and essentially plateaus at 10^{18} cm^{-3}. Also observed was a monotonic reduction in the mobility value upon increased Mg concentration. This is an ideal manifestation of a compensated predominant donor-like bulk layer. Correspondingly, a buried p-type layer was deduced by using the variable magnetic field Hall (VFH) effect measurement, although probing p-type conductivity was only seen over a limited Mg concentration range.

In PL, InN:Mg/GaN films exhibited a wide range of spectral features between 0.55 and 0.70 eV. The spectral structure of a high-energy peak just below 0.7 eV was significantly improved for the sample grown with a Mg cell temperature of 280 °C. This spectral feature was perfectly fit into a symmetrical Gaussian shape and the FWHM was only 20 meV. This intriguing property was characterized by a unique quadratic power-law relation in the excitation intensity dependent PL. This surely is irrefutable evidence of a "true" band-to-band transition. In temperature dependent PL, evidence of the band-tailing effect in the high energy wing was clearly seen, further confirming its nature.

The presence of a neutral acceptor bound acceptor was also the highlight of this thesis. Its response to varying excitation intensity yielded a linear power-law exponent k, which was a manifestation of excitonic transition. The non-monotonic trend of line broadening as a function of temperature has been described by the Bose-Einstein model and elucidated the temperature induced exciton-phonon interaction. Seeing the neutral acceptor bound exciton transition, PL excitation spectroscopy (PLE) is highly recommended for the future research. PLE is a widely used technique to determine the excitonic structure and in fact, has previously been employed to investigate excitons in Ga(As,N).

Also observed were a number of low PL energy features in an intermediate Mg level. These were originated from the Mg-related deep acceptor states, where the magnetotransport measurements pointed to the buried p-type layers. This view was in parallel with the

preliminary reported activation energies, being in a range of 48 to 50 meV. These levels were only apparent over a limited Mg cell temperature range of 272 to 287 °C, corresponding to the potential “p-type window”. Overdoping of Mg led to the transitions of free-to shallow acceptor bound states, which is a typical of n-InN. These phenomena suggest that a careful balance between relative In and Mg fluxes is required to successfully achieve both the p-type and non-degenerate conduction band (a band-to-band transition). These distinctive observations have provided a significant step towards implications for devices and beyond.

5.2 Key results of Zn-doped InN

Zn was considered to be a potential solution to overcome a surface electron accumulation layer, given its success with InAs. A study of Zn doped InN was also explored using a plasma-assisted molecular beam epitaxy technique. Both In- and N-rich growth conditions were examined over a wide range of Zn cell temperature of 75 to 248 °C. A surface accumulation layer still strongly affected the surface dependent studies and rendered electrical properties of the InN:Zn/GaN being inaccurate. Nevertheless, the VFH measurement only revealed an electron-mediated feature.

PL measured from N-rich films was swamped by a number of native impurities. The PL spectrum was broadened and shifted to higher energy as Zn concentration increased. Rather structureless PL line-shape restricted further analysis. In contrast, InN:Zn films grown under In-rich conditions exhibited better spectral resolution and consisted of multiple radiative paths over a wide range of PL features between 0.54 and 0.72 eV.

Similar to the effect of Mg, Zn doping of InN also resulted in alternative formation of neutral acceptor bound states initially peaking at 0.6 and 0.67 eV (at a low Zn level). Correspondingly, the activation energies as extracted from the Arrhenius equation also increased as a function of Zn cell temperature. A possible explanation of the highest energy feature at 0.72 eV was the transition of free electrons in the Fermi sea to a shallow bound state, the so called Mahan exciton. Meanwhile, a lower energy feature at 0.54 eV originated from the DAP and the effect of Zn doping particularly gave a rise to its PL intensity. This further confirms that the Zn doping resulted in an increase of the background electron

concentration and as has been the case for a N-rich InN:Mg/YSZ series, either the interstitial In or Zn-H complex doping arrangement was expected.

5.3 Key results of Mn-doped InN

The plausible theoretical calculation predicting room temperature ferromagnetism of III-MnN has triggered the research interest in this area. The central property of InN:Mn has therefore been investigated. In contrast to the former series of Mg and Zn doped InN, the N-rich growth condition not only significantly improved the Mn incorporation but also the catalogue of electrical and optical properties was advanced. Careful control of the Mn mole fraction was of the essence, in order for Mn to incorporate on an In vacancy site and thus forming a p-type. As a direct consequence of the electron accumulation layer, both the carrier concentration and mobility from SFH measurements rather were overestimated and returned an increase with Mn content. Alternatively, VFH measurement has probed a distinctive hole mobility in N-rich InN:Mn, although this finding was observed only with the critical Mn nominal mole fraction of 0.01%. Meanwhile, evidence of a buried p-type layer was not determined from In-rich zones.

As expected from VFH measurements, PL of In-rich zones gave typical n-type characteristics. As the Mn temperature was increased, the emission broadened and the Moss-Burstein effect was distinguishable. In contrast, PL spectra were well-structured for the samples from the N-rich zone. The sample grown with a critical Mn mole fraction of 0.01% particularly exhibited a dominant low feature at 0.54 eV and was indeed a Mn deep acceptor. This feature likely corresponded to a buried p-type layer, which was recognized by VFH and was in fact determined to have a minimum value of the surface Fermi energy as measured by XPS. The transition type of the 0.54 eV peak was convincingly confirmed by photoconductivity measurement (PC), where the onset of a midgap photocurrent (DAP) was in the vicinity of the PL peak. The activation energies were 91 and 35 meV for a Mn deep acceptor and a shallow donor, respectively. The former value coincided with a Mg activation energy in InN. However, the origin of the donors in this DAP transition has remained an open question.

This work concludes that InMnN is a promising ferromagnetic candidate alternative to (In,Ga)MnAs. Answers inevitably lead to more questions and the work undertaken in this thesis is only a partial solution. Essentials of substrate choice, growth temperatures, and annealing effect should be comprehensively investigated for an understanding of the genuine physical properties of InMnN. More importantly, the magnetic property of InMnN also should be carried out to correlate with both electrical and optical properties.

Appendix

A. Molecular beam epitaxy growth and characterization techniques

MBE Growth by Dr. Jessica Chai and Dr. Chito Kendrick at University of Canterbury

SIMS by Dr. Richard Morris and Mr. Wojtek Linhart at University of Warwick

SFH and SEM by Dr. Jessica Chai and Dr. Chito Kendrick at University of Canterbury

VFH by Prof. Thomas Myer, at Texas State University

Molecular beam epitaxy (MBE) is the ideal growth method for research purposes due to an easy and precise control of the growth parameters[237]. One major factor which utilizes the MBE technique is the UHV environment in the region of 10^{-9} Torr. This clean growth mode significantly precludes oxygen contamination, which initially brought a subject prolific of controversy over InN bandgap.

All InN thin films grown in this thesis is based on a plasma-assisted MBE technique and its system overview is schematically drawn in figure A. Substrates are attached on molybdenum blocks and transfers into the UHV chamber via the load-locks, where a sorption pump brings an initial pressure down to 10^{-4} Torr. A combined operation of a cryogenic pump and an ion pump can further reduce the pressure to 10^{-8} Torr. The latter process is to outgas the growth blocks, although this system shuts down during the actual growth and the pressure maintains at 10^{-5} Torr (only the cryogenic pump operates).

The manipulator heater is connected to the substrate mounted molybdenum block, which enables precise control of the substrate temperature. An HD25 Oxford Applied Research plasma source (the radio frequency inductively coupled) activates N_2 molecule, which makes a low dissociation temperature of InN of less concern. All metallic species including indium, magnesium, manganese, and zinc are produced by conventional Knudsen effusion cells. Finally, the laser interferometer monitors the growth rate and characterizes the surface morphology through an analysis of reflection high energy electron diffraction (RHEED)

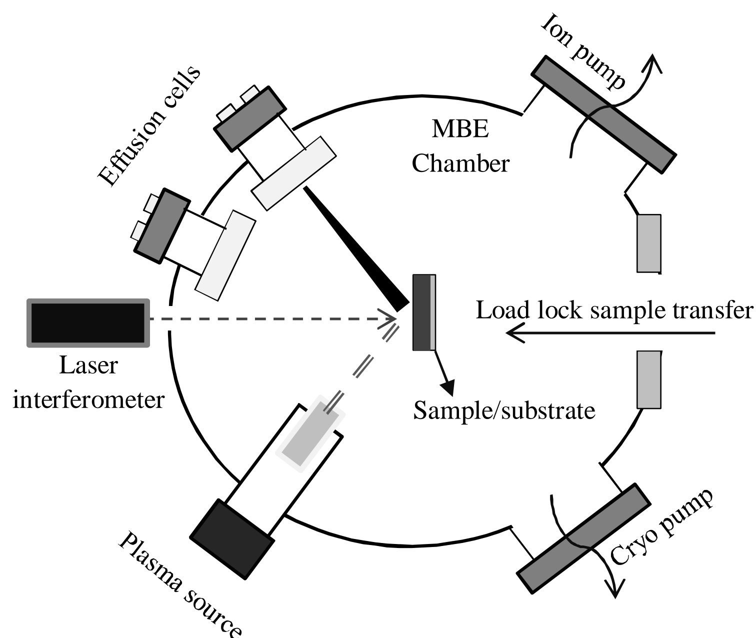

Figure A A simple schematic diagram of the nitride MBE system.

pattern.

The acceptor doping concentration was extracted from secondary ion mass spectrometry (SIMS). SIMS experiments in this thesis used an Atomika 4500 SIMS instrument and a primary 500 eV O_2^+ ion beam was employed for the sputtering source. A simple description of SIMS is that the resultant ejected charged secondary ions (*ie*. positive or negative) are collected by a mass spectrometer and a careful analysis of the mass/charge gives a precise dopant concentration range.

The surface morphology was recognized by Scanning electron microscope (SEM). SEM in this thesis used a Raith 150 electron beam lithography system. A tightly focused electron beam directed to the thin film surface with voltage of 10 keV and the resultant ejected electron digitized into the image via a Leica field emission electron microscope.

Detailed electrical property of p-InN was determined from Hall effect measurements. Room temperature single magnetic Hall effect (SFH) measurements were performed using an EGK HEM-2000 meter. This system is based on the van der Pauw geometry. A combination of a current supply current via evaporated Au ohmic contacts and a magnetic field operation of

0.51 T gives a potential difference across the surface layer. This transverse force characterized by the Lorentz force model returns the useful electrical parameters such as the carrier concentration and mobility.

Meanwhile, variable magnetic field Hall effect measurements (VFH) were conducted using a Quantum Design Model 6000 Physical Property Measurement System. Use of various magnetic fields, which distinguishes groups of carriers with multiple conducting paths, discriminates this type of measurement from the SFH. Hall voltage of each layer can be modeled using quantitative mobility spectrum analysis (QMSA) and the discovery of the carrier concentration and mobility of bulk layers is feasible. (note: one electron, one hole, and a residual low mobility carrier fit was used in this analysis; *ie*. figure 5.6)

B. Film thickness effect

Growth and SFH by Dr. Chito Kendrick at University of Canterbury

The one major growth parameter to be optimized is the film thickness. A number of studies have adequately addressed the effect of thickness on the central properties of InN[139-142], where commonly observed was Hall measurements being strongly influenced by the growth rate. Particularly the single magnetic field Hall effect (SFH) measures a lower background electron concentration with an increased film thickness, which represents that the surface effect of the density of threading location and an electron accumulation layer become less relevance[139-143].

Table B A summary of growth condition (thickness) and Hall effect measurements of InN/YSZ films.

Film number	Thickness (nm)	μ ($cm^2V^{-1}s^{-1}$)	n (cm^{-3})
683-InN/YSZ	5000	1281	6.8×10^{18}
674-InN/YSZ	500	442	1.5×10^{19}
672-InN/YSZ	200	210	2.8×10^{19}
671-InN/YSZ	100	230	3.7×10^{19}
670-InN/YSZ	50	136	8.5×10^{19}
682-InN/YSZ	5	29	5.0×10^{20}

Note: μ → mobility, n → carrier concentration

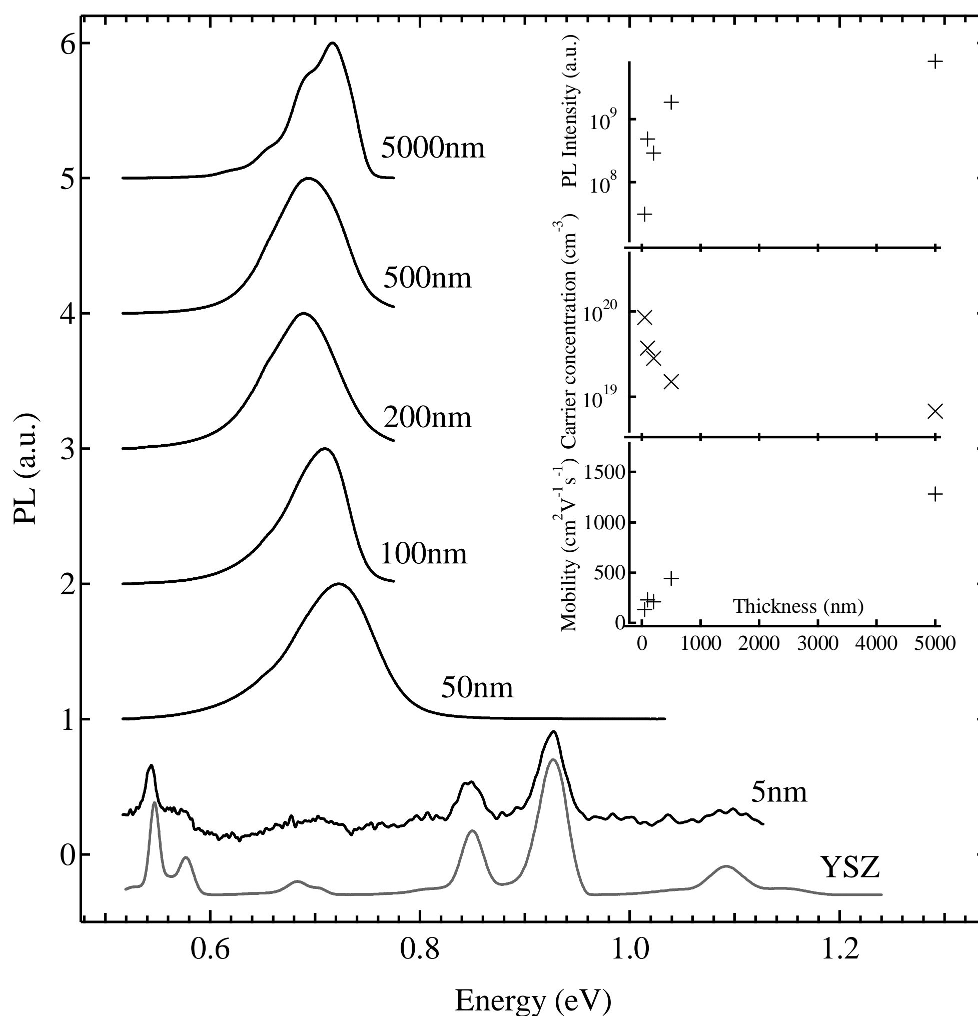

Figure B 4 K PL spectra of InN/YSZ with a wide range of film thicknesses. The inset shows the PL intensity (top), SFH carrier concentration (middle), and SFH mobility as a function of film thickness.

In this study, a series of InN samples were grown with various film thicknesses ranging from 5 to 5000 nm. The parameters of films grown in a thickness dependent series on (111) YSZ are present in table B. Similar to what has been reported previously, the values of the mobility and carrier concentration have gradually improved with thin film thickness. The SFH carrier concentration shows a decrease as a function of film thickness, while the extracted mobility value is considerably increased. The rather low mobility in thinner samples strongly implies the strong influence of the surface electron accumulation layer and the threading dislocation, whereas the sudden upswing of mobility near 5 micron thickness is noteworthy.

The study of optical properties fully agrees with the trend in SFH electrical parameters. In PL, the quantum efficiency increases with the film thickness as shown in figure B. Also observed

was a gradual blueshift of the main emission as it follows the Moss-Burstein effect. All features are asymmetric, having a broad FWHM range approximately 60 meV to 80 meV, which is correlated to the film thickness in some extent. The later onset of high energy feature for the sample grown with a 5000 nm thickness is not consistent with such a trend, although a better spectral resolution suggests a better thin film quality. Meanwhile, an emission from the YSZ substrate is evident in the 5 nm thick InN sample. This indicates that 5 nm is perhaps an insufficient thickness for the optical characterization, where the diffusion of photo-excited carriers occurs much deeper than the actual epilayer.

C. Ion bombardment and annealing effect of Mg-doped InN

Ion implantation by Dr. John Kennedy at GNS Science Ltd.

Many literatures discussed that a Mg overdoping introduces donor-like defect complexes and significantly enhances the PL intensity. Detailed studies of PL in Mg-doped InN by Wang *et al.*[133] observed that the sample with the heaviest doping concentration gave a rise of PL intensity from the completely quenched signals. An irradiation particle induced PL study by Jones *et al.*[132] supported such an understanding. In order to more solidly identify the role of native point defects in InN, the effect of ion-bombardment was explored in this research. 2 MeV He^+ particle beam of 0.42 cm^2 with 200 nA operating current was used. As mentioned elsewhere, He^+ irradiation exclusively acts as a donor in InN and significantly increases the background electron concentrations[149]. Also reported was the He^+ fluence of 2×10^{15} cm^{-2} being the most ‘efficient dose’ to override the hole concentration[132]. The film damage caused by the irradiated He^+ has been recovered by rapid thermal annealing (RTA) processes.

Figure C shows the evolution of the PL spectrum of GS1810 film subjected to 2 MeV He^+ and RTA. Subsequent to irradiation, the electron background concentration of this film is likely increased, which corresponds to a high energy feature well above the bandgap. Two features are peaking at 0.82 and 0.42 eV. A possible explanation of these two peaks is that the 0.82 eV peak arises from transitions of degenerate electrons above the CBM to some type of neutral acceptor bound state while the 0.54 peak is likely related to a ‘residual’ Mg acceptor. This Mg level shifts to red owing a combination of the creation of new Mg-H donor level (forms a DAP transition) and the potential fluctuation of neutral bound states[222-224] as discussed in section 4.2. Most notably, newly introduced PL intensity increases by more than

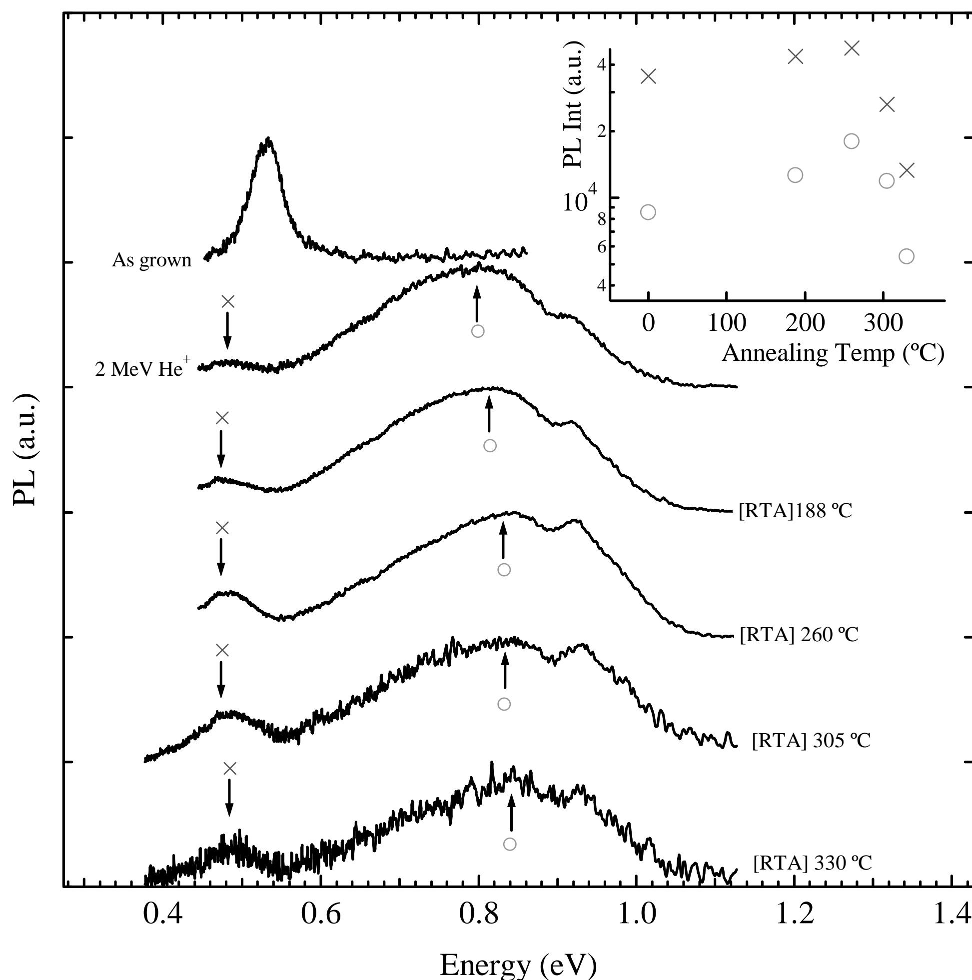

Figure C PL spectra of GS1810 as grown, irradiated fluence of 2×10^{15} cm^{-2} and various annealing temperatures. The inset shows the absolute PL intensities of two designated (arrows) features as a function of annealing temperature.

an order of magnitude, and the maximum PL intensity is reached at an annealing temperature of 260°C. A reduction of intensity is observed at an annealing temperature of 305°C onwards. This refers to the onset of Auger recombination as the p-type re-establishes[150]. Correspondingly, as the RTA temperature increases, the higher energy feature emission blueshifts until the threshold is reached. The same result is obtained for a lower energy peak, although by a lesser amount. This represents a significant reduction in the background electron concentration upon RTA[154]. A noticeable dip at 0.9 eV is attributed to the OH vibration as discussed in section 3.8.

Reference

[1] G. E. Moore, “Cramming more components onto integrated circuits,” Electronics magazine, **38**, 114, (1965).

[2] H. P. Maruska, and J. J. Tietjen, “The preparation and properties of vapor-deposited single-crystal-line GaN,” Appl. Phys. Lett. **15**, 327 (1969).

[3] O. Ambacher, “Growth and applications of Group III-nitrides,” J. Phys D: Appl. Phys. **31**, 2653 (1998).

[4] H. Amano, I. Akasaki, T. Kozowa, H. Hiramatsu, N. Sawak, K. Ikeda, and Y. Ishii, “Electron beam effects on blue luminescence of zince-doped GaN,” J. Luminescence **40**, 121 (1988).

[5] H. P. Maruska and J. J. Tietjen, “The preparation and properties of vapor-deposited single-crystal-line GaN,” Appl. Phys. Lett. **15**, 327 (1969).

[6] Isamu Akasaki and Hiroshi Amano, “Crystal Growth and Conductivity Control of Group III Nitride Semiconductors and Their Application to Short Wavelength Light Emitters,” Jpn. J. Appl. Phys. **36**, 5393 (1997).

[7] A. A. High, E. E. Novitskaya, L. V. Butov, M. Hanson, and A. C. Gossard, “Control of exciton fluxes in an excitonic integrated circuit,” Science **321**, 229 (2008).

[8] H. Yamashita, K. Fukui, S. Misawa, and S. Yoshida, “Optical properties of AlN epitaxial thin films in the vacuum ultraviolet region,” J. Appl. Phys. **50**, 896 (1979).

[9] S. Nakamura, M. Senoh, and T. Mukai, “P-GaN/N-InGaN/N-GaN double-heterostructure blue-light-emitting diode,” Jap. J. Appl. Phys. Part 2: Lett. **32**, L8 (1993).

[10] S. Nakamura, T. Mukai, and M. Senoh, “High-power GaN P-N junction blue-lighting diodes,” Jap. J. Appl. Phys. Part 2: Lett. **30**, L1998 (1991).

[11] S. Nakamura, “InGaN/AlGaN blue-light-emitting diodes, “J. Vac. Sci. Tech. A **13**, 705 (1995).

[12] S. Nakamura, M. Senoh, S. ichi Nagahama, N. Iwasa, T. Yamada, T. Matsushita, H. Kiyoku, and Y. Sygimoto, “InGaN multi-quantum-well structure laser diodes grown on $MgAl_2O_4$ substrates, “ Appl. Phys. Lett. **68**, 2105 (1996).

[13] I. Akasaki and H. Amano, “GaN,” Academic **1**, New York (1998).

[14] V. Yu Davydov, A.A. Klochikhin, V.V. Emtsev, S.V. Ivanov, V.V. Vekshin, F. Bechstedt, J. Furthmuller, H. Harima, A.V. Mudryi, A. Hashimoto, A. Yamamoto, A.J. Aderhold, J. Graul, E.E. Haller, “Absorption and emission of hexagonal InN. Evidence of narrow fundamental band gap,” Phys. Stat. Sol. b **23**, R4 (2002).

[15] R. Juza and H. Hahn, “Uber die kristallstrukturen von Cu_3N, GaN und InN metallamide und metallnitride," Anorg. Allgem. Chem. **234**, 282 (1938).

[16] D. –J. Jang, G. –T. Lin, C. –L. Hsiao, L. W. Tu, and M. –E. Lee, “Auger recombination in InN thin films,” Appl. Phys. Lett. **92**, 042101 (2008).

[17] A. J. Sierakowskia and L. F. Eastman, “Analysis of schottky gate electron tunneling in polarization induced AlGaN/GaN high electron mobility transistors," J. Appl. Phys. **86**, 3398 (1999).

[18] T.L. Tansley, C.P. Foley, “Optical band gap of indium nitride,” J. Appl. Phys. **59**, 3241 (1986).

[19] K. L. Westra, R. P. W. Lason, and M. J. Brett, “The effects of exygen contamination on the properties of reactively sputtered indium nitride films,” J. Vac. Sci. Technol. A **6**, 1730

(1989).

[20] D. W. Jenkins and J. D. Dow, “Electronic structures and doping of InN, $In_xGa_{1-x}N$ and $In_xAl_{1-x}N$,” Phys. Rev. B **39**, 3317 (1989).

[21] K. Ikuta, Y. Inoue, and O. Takai, “Optical and electrical properties of InN thin films grown on ZnO/alpha-Al_2O_3 by RF reactive magnetron sputtering,” Thin Solid Films, **334**, 49 (1998).

[22] T. Inushima, V.V.Mamutin, V.A. Vekshin, S.V. Ivanov, T. Sakon, M. Motokawa, S. Ohoya, “Physical properties of InN with the band gap energy of 1.1 eV,” J. Cryst. Growth **481**, 227 (2001).

[23] M. Sumiya, N. Ogusu, Y. Yotsuda, M. Itoh, , S. Fuke, T. Nakamura, S. Mochizuki, T. Sano, S. Kamiyama, H. Amano, and I. Akasaki, “Systematic analysis and control of low temperature GaN buffer layers on sapphire substrates," J. Appl. Phys. **93**, 1311 (2003).

[24] J. Wu, W. Walukiewicz, K.M. Yu, J.W. Ager III, E.E. Haller, H. Lu, W. Schaff, Y. Saito, Y. Nanishi, “Unusual properties of the fundamental band gap of InN,” Appl. Phys. Lett. **80**, 3967 (2002).

[25] M. Higashiwaki, and T. Matsui, “Estimation of band-gap energy of intrinsic InN from photoluminescence properties of undoped and Si-doped InN films grown by plasma-assisted molecular-beam epitaxy,” J. Cryst. Growth **269**, 162 (2004).

[26] T. Yodo, H. Yona, H. Ando, D. Nosei, and Y. Harada, “Strong band edge luminescence from InN films grown on Si substrates by electron cyclotron resonance-assisted molecular beam epitaxy,” Appl. Phys. Lett. **80**, 968 (2002).

[27] D. B. Haddad, J. S. Takur, V. M. Naik, G. W. Auner, R. Naik, L. E.Wenger, “Optical band gap measurements of InN films in the strong degeneracy limit,” Mater Res. Soc. Symp. Proc. **743**, 701 (2003).

[28] T. V. Shubina, S. V. Ivanov, V. N. Jmerik, D. D. Solnyshkov, V. A. Veshkin, P. S. Kop'ev, A. Vasson, J. Leymarie, A. Kavokin, H. Amano, K. Shimono, A. Kasic and M. Monemar, “Mie resonances, infrared emission, and the band gap of InN,” Phys. Rev. Lett. **92,** 117407-1 (2004).

[29] E. Burstein, “Anomalous optical absorption limit in InSb,” Phys. Rev. **93**, 632 (1954)

[30] R. Bechstedt, J. Furthmüller, O. Ambacher, and R. Goldhahn, “Comment on ‘Mie resonances, infrared emission, and the band gap of InN,” Phys. Rev. Lett. **93,** 269701 (2004).

[31] I. Mahboob, T. D. Veal, L. F. J. Piper, C. F. McConville, L. Hai, W. J. Schaff, J. Furthmüller, and F. Bechstedt, “Origin of electron accumulation at wurtzite InN surfaces,” Phys. Rev. B **69**, 201307 (2004).

[32] W. Walukiewicz, S. X. Li, J. Wu, K. M. Yu, J. W. Ager III, E. E. Haller, H. Lu, and W. J. Schaff, “Optical properties and electronic structure of InN and In-rich group III-nitride alloys,” J. Cryst. Growth **269**, 119 (2004).

[33] V. Y. Davydov, A. A. Klochikhin, V. V. Emtsev, D. A. Kurdyukov, S. V. Ivanov, V. A. Vekshin, F. Bechstedt, J. Furthmuller, J. Aderhold, J. Graul, A. V. Mudryi, H. Harma, A. Hashimoto, A. Yamamoto, and E. E. Haller, “Band gap of hexagonal InN and InGaN alloys,” Phys. Stat. Sol. (b) **234**, 787 (2002).

[34] A. Marti and G. L. Araujo, “Limiting efficiencies for photovoltaic energy conversion in multigap systems," Solar Energy Materials and Solar Cells **43**, 203 (1996).

[35] A. Kasic, M. Schubert, Y. Saito, Y. Nanishi, and G. Wagner, “Effective electron mass and phonon modes in n-type hexagonal InN,” Phys. Rev. B **65**, 115206 (2002).

[36] C. Persson and A. Zunger, “s-d coupling in zinc-blende semiconductors,” Phys. Rev. B **68**, 073205 (2003).

[37] F. Bechstedt and J. Furthmüller, "Do we know the fundamental energy gap of InN?," J. Cryst. Growth **246**, 315 (2002).

[38] J. Furthmüller, P. H. Hahn, F. Fuchs, and F. Bechstedt, "Band strucutres and optical spectra of InN polymorphs: Influence of quasiparticle and excitonic effects," Phys. Rev. B **72**, 205106:1-14 (2005).

[39] M. Yoshimoto, H. Yamamoto, W. Huang, H. Harima, J. Saraie, A. Chayahara, Y. Horino, "Widening of optical bandgap of polycrystalline InN with a few percent incorporation of oxygen," Appl. Phys. Lett. **83**, 3480 (2003).

[40] Q Li, S. J. Xu, M. H. Xie, and S. Y. Tong, "Origin of the 'S-shaped' temperature dependence of luminescent peaks from semiconductors," J. Phys.: Condens. Matter **17**, 4853 (2005).

[41] J. Frenkel, "On the Transformation of light into Heat in Solids. I," Physical Review **37**, 17 (1931).

[42] R. Ramesh, and N. A. Spaldin, "Multiferroics: Progress and prospects in thin films," Nat. matter **6**, 21-29 (2007).

[43] W. Y. Liang, "Excitons". Physics Education **5**, 226 (1970).

[44] C. F. Klingshirn, "Semiconductor optics," Springer (1997).

[45] A. Dmitriev, and A. Oruzheinikov, "The rate of radiative recombination in the nitride semiconductors and alloys," J. Appl. Phys, **86,** 3241 (1999).

[46] B. K. Meyer, H. Alves, D. M. Hofmann, W. Kriegseis, D. Forster, F. Bertram, J. Christen, A. Hoffmann, M. Straburg, M. Dworzak, U. Haboeck, and A.V. Rodina, "Bound exciton and donor-acceptor pair recombinations in ZnO," Phys. Stat. Sol. (b) **241**, 231 (2004).

[47] L. Stauffer, and B. Stebe, "Binding energy of ionized-donor-bound exictons in two-dimensional semiconductors," Phys. Rev. B **39**, 8 (1989).

[48] D. C. Reynold, D. C. Look, B. Jogai, V. M. Phanse, and R. P. Vaudo, "Identification of an ionized-donor-bound-exciton transition in GaN," Sol. Stat. Comm. **103,** 533 (1997).

[49] E. O. Kane, "Band structure of Indium Antimonide," J. Phys. Chem. Solids **1**, 249-261 (1957).

[50] H. A. Washburn, J. R. Sites, and H. H. Wieder, "Electronic profile of *n*-InAs on semi-insulating GaAs," J. Appl. Phys. **50**, 4872 (1979).

[51] J. Wu, W. Walukiewicz, K.M. Yu, J.W. Ager III, E.E. Haller, H. Lu, W. J. Schaff, "Effects of the narrow band gap on the properties of InN," Phys. Rev. B **66**, 201403 (2002).

[52] C. Skierbiszewski P. Perlin, P. Wisniewski, W. Knap, T. Suski, W. Walukiewicz, W. shan, K. M. Yu, J. W. Ager, E. E. Haller, J. F. Geisz, and J. M. Olson, "Large, nitrogen-induced increase of the electron effective mass in $In_yGa_{1-y}N_xAs_{1-x}$," Appl. Phys. Lett. **76**, 2409 (2000).

[53] J. S. Im, A. Moritz, F. Steuber, V. Härle, F. Scholz, and A. Hangleiter, "Radiative carrier lifetime, momentum matrix element and hole effective mass in GaN," Appl. Phys. Lett. **70**, 631 (1997).

[54] P. Perlin, E. Litwin-Staazewska, B. Suchanek, W. Knap, J. Camassel, T. Suski, R. Piotrzkowski, I. Grzegory, S. Porowski, E. Kaminska, and J. C. Chervin, "Determination of the effective mass of GaN from infrared reflectivity and Hall effect," Appl. Phys. Lett. **68**, 1114 (1996).

[55] I. Vurgaftman, J. R. Meyer, and L. R. Ram-Mohan,"Band parameters for III-V compound semiconductors and their alloys," J. Appl. Phys. **89**, 5815 (2001).

[56] K. Sugita, H. Takatsuka, A. Hashimoto, A. Yamamoto, "Photoluminescence and optical absorption edge for MOVPE-grown InN," Phys. Stat. Sol. b **240**, 421 (2003).

[57] V. A. Tyagai, A. M. Evstigneev, A. N. Krasiko, A. F. Andreeva, V. Y. Malakhov, "Optical-properties of Indium Nitride films," Sov. Phys. Semicond. **11**, 1257 (1977).

[58] K. S. A. Butcher, M. Wintrebert-Fouquet, P. P.-T. Chen, K. E. Prince, H. Timmers, S. K. Shrestha, T. V. Shubina, S. V. Ivanov, R. Wuhrer, M. R. Phillips, B. Monemar, "Nonstoichiometry and nonhomogeneity in InN," Phys. Stat. Sol. c **2**, 2263 (2005).

[59] B. R. Natarajan, A. H. Eltoukhy, J. E. Greene, T. L. Barr, "Mechanisms of reactive sputtering of Indium. 1. Growth of InN in mixed AR-N2 discharges," Thin Solid Films **69**, 201 (1980).

[60] V. Cimalla, G. Ecke, M. Niebelschutz, O. Ambacher, R. Goldhahn, H. Lu, and W. Schaff, "Surface conductivity of epitaxial InN," Phys. Stat. Sol. c **2**, 2254 (2005).

[61] P. A. Anderson, C. H. Swartz, D. Carder, R. J. Reeves, S. M. Durbin, S. Chandril, and T. H. Myers, "Buried *p*-type layers in Mg-doped InN," Appl. Phys. Lett. **89**, 184104 (2006).

[62] W. J. Schaff, H. Lu, J. Hwang, and H. Wu, "Growth of InN for heterojunction field effect transistor applications by plasma enhanced MBE," IEEE proceedings, Cornell conference on high performance devices 225-231, Ithaca New York, USA (2000).

[63] H. Lu, W. J. Schaff, L. F. Eastman, and C. E. Stutz, "Surface charge accumulation of InN films grown by molecular-beam epitaxy," Appl. Phys. Lett. **82**, 1736 (2003).

[64] K. A. Rickert, A. B. Ellis, F. J. Himpsel, H. Le, W. Schaff, J. M. Redwing, F. Dwikusuma, and T. F. Kuech, "X-ray photoemission spectroscopic investigation of surface treatements, metal deposition, and electron accumulation on InN," Appl. Phys. Lett. **82**, 3254 (2003).

[65] V, -T. Rangel-Kuoppa, S. Suihkonen, M. Sopanen, and H. Lipsanen, “Metal contacts on InN: Proposal for Schottky contact,” Jpn. J. Appl. Phys. **45**, 162107 (2007).

[66] R. Khanna, B. P. Gila, L. Stafford, S. J. Pearton, F. Ren, I. I. Kravchenko, A. Dabiran, and A. Osinsky, “Thermal stability of Ohmic contacts to InN,” Appl. Phys. Lett. **90**, 162107 (2007).

[67] I. Mahboob, T. D. Veal, C. F. McConville, H. Lu, and W. J. Schaff, “Intrinsic electron accumulation at clean InN surface,” Phys. Rev. Lett. **92**, 036804 (2004).

[68] S. X. Li, K. M. Yu, J. Wu, R. E. Jones, W. Walukiewicz, J. W. Ager III, W. Shan, E. E. Haller, Hai Lu, and W. J. Schaff, “Fermi-level stabilization energy in group III-nitrides,” Phys. Rev. B **71**, 161201 (2005).

[69] I. P. Smorchkova, E. Haus, B. Heying, P. Kozodoy, P. Fini, J. P. Ibbetson, S. Keller, S. P. DenBaars, J. S. Speck, and U. K. Mishra, “Mg doping of GaN layers grown by plasma-assisted molecular-beam epitaxy,” Appl. Phys. Lett. **76,** 718 (2000).

[70] M. F. Schubert, S. Chhajed, J. K. Kim, E. F. Schubert, D. D. Koleske, M. H. Crawford, S. R. Lee, and A. J. Fischer, “Effect of dislocation density on efficiency droop in GaInN/GaN light-emitting diodes,” Appl. Phys. Lett. **91**, 231114 (2007).

[71] L. F. J. Piper, T. D. Veal, I. Mahboob, C. F. McConville, H. Lu, and W. J. Schaff, “Temperature invariance of InN electron accumulation,” Phys. Rev. B **70**, 115333 (2004).

[72] P. D. C. King, T. D. Veal, P. H. Jefferson, C. F. McConville, H. Lu, and W. J. Schaff, “Variation of band bending at the surface of Mg-doped InGaN: Evidence of *p*-type conductivity across the composition range,” Phys. Rev. B **75**, 115312 (2007).

[73] P .D. C. King, T. D. Veal, W. J. Schaff, and C. F. McConville, “Surface electronic properties of Mg doped InAlN alloys,” Phys. Stat. Sol. b **246**, 1169 (2009).

[74] T. D. Veal, P. H. Jefferson, L. F. J. Piper, C. F. McConville, T. B. Joyce, P. R. Chalker, L. Considine, H. Lu, and W. J. Schaff, “Transition from electron accumulation to depletion at InGaN surfaces,” Appl. Phys. Lett. **89**, 202110 (2006).

[75] N. Miller, J. W. Ager, H. M. Smith, M. A. Mayer, K. M. Yu, E. E. Haller, W. Walukiewicz, W. J. Schaff, C. Gallinat, G. Koblmuller, and J. S. Speck, “Hole transport and photoluminescence in Mg-doped InN,” J. Appl. Phys. **107**, 113712 (2010).

[76] D. Imai, Y. Ishitani, M. Fujiwara, K. Kusakabe, X. Wang, and A. Yoshikawa, “Carrier recombination processes in Mg-doped N-polar InN films,” Appl. Phys. Lett. **98**, 181908 (2011).

[77] M. –H. Kim, M. F. Schubert, Q. Dai, J. K. Kim, F. E. Schubert, J. Piprek, and Y. Park, “Origin of efficiency droop in GaN-based light-emitting diodes,” Appl. Phys. Lett. **91**, 183507 (2007).

[78] A. A. Efremov, N. I. Bochkareva, R. I. Gorbunov, D. A. Larinovich, Y. T. Rebane, D. V. Tarkhin, and Y. G. Shreter, “Effect of the joule heating on the quantum efficiency and choice of thermal conditions for high-power blue InGaN/GaN LEDs,” Semiconductors **40**, 605 (2006).

[79] A. Y. Kim, W. Götz, D. A. Steigerwald, J. J. Wierer, N. F. Gardner, J. Sun, S. A. Stockman, P. S. Martin, M. R. Krames, R. S. Kern, and F. M. Steranka, “Performance of high-power AlInGaN light emitting diodes,” Phys. Stat. Sol. a, **188**, 15 (2001).

[80] Y. C. Shen, G. O. Müller, S. Watanabe, N. F. Gardner, A. Munkholm, and M. R. Krames, “Auger recombination in InGaN measured by photoluminescence,” Appl. Phys. Lett. **91**, 141101 (2007).

[81] E. Ohshima, H. Ogino, I. Niikura, K. Maeda, M. Sato, M. Ito, and T. Fukuda, “Growth of the 2-in-size bulk ZnO single crystals by the hydrothermal method,” J. Cryst. Growth **260**, 166 (2004).

[82] A. Luque, A. Martí, E. Antolín, and C. Tablero, “Intermediate bands versus levels in non-radiative recombination,” Physica B **382**, 320 (2006).

[83] K. T. Delaney, P. Rinke, and C. G. Van de Walle, “Auger recombination rates in nitrides from first principles,” Appl. Phys. Lett. **94**, 191109 (2009).

[84] A. E. Chernyakov, M. M. Sobolev, V. V. Ratnikov, N. M. Shmidt, and E. B. Yakimov, “Nonradiative recombination dynamics in InGaN/GaN LED defect system,” Superlattices and Microstructure **45**, 301 (2009).

[85] P. E. Petersen, “Auger Recombination in $Hg_{1-x}Cd_xTe$,” J. Appl. Phys. **41**, 3465 (1970).

[86] M. A. Kinch, M. J. Brau, and A. Simmons, “Recombination mechanisms in 8-14-μ HgCdTe,” J. Appl. Phys. **44**, 1649 (1973).

[87] S. Krishnamurthy, and T. N. Casselman, “A detail calculation of the Auger lifetime in p-type HgCdTe,” J. Elec. Mat. **29**, 6 (2000).

[88] S. Anikeev, D. Donetsky, G. Belenky, S. Luryi, C. A. Wang, J. M. Borrego, and G. Nichols, “Measurement of the Auger recombination rate in *p*-type 0.54 eV GaInAsSb by time-resolved photoluminescence,” Appl. Phys. Lett. **83**, 16 (2003).

[89] M. A. Kinch, F. Aqariden, D. Chandra, P. –K. Liao, H. F. Schaake, and H. D. Shin, “Minority carrier lifetime in p-HgCdTe,” J. Elec. Mat. **34**. 6 (2005).

[90] A. A. Klochikhin, V. Y. Davydov, V. V. Emtsev, A. V. Sakharov, V. A. Kapitonov, B. A. Andreev, H. Lu, and W. J. Schaff, “Acceptor states in the photoluminescence spectra of n-InN,” Phys. Rev. B **71**, 195207 (2005).

[91] B. Arnaudov, T. Paskova, P. P. Paskov, B. Magnusson, E. Valcheva, B. Monemar, H. Lu, W. J. Schaff, H. Amano, and I. Akasaki, “Energy position of near-band-edge emission spectra of InN epitaxial layers with different doping levels,” Phys. Rev. B **69**, 115216 (2004).

[92] N. Khan, N. Nepal, A. Sedhain, J. Y. Lin, and H. X. Jiang, “Mg acceptor level in InN epilayers probed by photoluminescence,” Appl. Phys. Lett. **91**, 012101 (2007).

[93] B. N. Pantha, A. Sedhain, J. Li, J. Y. Lin, and H. X. Jiang, “Electrical and optical properties of p-type InGaN,” Appl. Phys. Lett. **95**, 261904 (2009).

[94] Y.P. Varshni, “Temperature dependence of the energy gap in semiconductors,” Physica **34**, 149 (1967).

[95] R. Pässler, “Temperature dependence of exciton peak energies in multiple quantum wells,” J. Appl. Phys. **83**, 3356 (1998).

[96] M. Quintero, R. Tovar, C. Bellabara, and J. C. Woolley, “Temperature variation of optical energy gap and deformation potentials in $AgInTe_2$,” Phys. Stat. Sol (b) **162**, 517 (1990).

[97] S. A. Lourenço, I. F. L. Dias, J. L. Duarte, E. Laureto, E. A. Meneses, J. R. Leite, and I. Mazzaro, “Temperature dependence of optical transitions inAlGaAs,” J. Appl. Phys. **89**, 11 (2001).

[98] A. S. Zubrilov, S. A. Nikishin, G. D. Kipshidze, V. V. Kuryatkov, H. Temkin, T. I. Prokofyeva, and M. Holtz, “Optical properties of GaN grown on Si (111) by gas source molecular beam epitaxy with ammonia,” J. Appl. Phys. **91**, 3 (2002).

[99] N. W. Winogradoff, and A. H. Neill, JR., “Band-tailing effects and the temperature dependence of radiative recombination in compensated epitaxial GaAs laser junctions,” J. Quantum electronics **4**, 111 (1968).

[100] M. Feneberg, J. Däubler, K. Thonke, R. Sauer, P. Schley, and R. Goldhahn, “Mahan excitons in degenerate wurtzite InN: Photoluminescence spectroscopy and reflectivity measurements,” Phys. Rev. B **77**, 245207 (2008).

[101] L. Bergman, M. Dutta, M. A. Stroscio, S. M. Komirenko, R. J. Nemanich, C. J. Eiting, D. J. H. Lambert, H. K. Kwon, and R. D. Dupuis, “Photoluminescence and recombination mechanisms in GaN/$Al_{0.2}Ga_{0.8}N$ superlattice,” Appl. Phys. Lett. **76**, 15 (2000).

[102] I. Hamberg, C. G. Granqvist, K. F. Berggren, B. E. Sernelius, and L. Engstrom, “Band-gap widening in heavily Sn-doped In_2O_3,” Phys. Rev. B **30**, 3240 (1984).

[103] A. W. Juarez, L. F. Da Silva, and S.-H. Wei, “Origins of band-gap renormalization in degenerately doped semiconductors,” Phys. Rev. B **78**, 075211 (2008).

[104] R. Hellmann, M. Koch, J. Feldmann, S.T. Lundiff, E.O. Gobel, D.R. Yakovler, A. Waag, G. Landwehr, “Homogeneous linewidth of excitons in semimagnetic CdTe/$Cd_{1-x}Mn_xTe$ multiple quantum wells,” Phys. Rev. B **48**, 2847 (1993).

[105] M. O’Neill, M. Oestriech, W.W. Ruhle, D.E. Ashenford, “Exciton radiative decay and homogeneous broadening in CdTe/$Cd_{0.85}Mn_{0.15}Te$ multiple quantum wells,” Phys. Rev. B **48**, 8980 (1993).

[106] S. Zemon, and G. Lambert, “Photoluminescence spectra in an applied magnetic field for excitons bound to ionized donors in high-purity, epitaxial GaAs,” J. Appl. Phys. **70**, 4909 (1991).

[107] T. Taguchi, J. Shirafuji, and Y. Inuishi, “Excitonic emission on Cadium Telluride,” Phys. Stat. Sol. b, **68**, 727 (1975).

[108] A. Manoogian and A. Leclerc, “Determination of the dilation and vibrational contributions to the energy band gaps in germanium and silicon,” Phys. Stat. Sol. b **92**, K23 (1979).

[109] A. Manoogian and J.C. Woolley, “Temperature dependence of the energy gap in semiconductors,” Can. J. Phys. **62**, 285 (1984).

[110] L. Viña, S. Logothetidis, and M. Cardona, “Temperature dependence of the dielectric function of germanium,” Phys. Rev. B **30**, 1979 (1984).

[111] J. R. Taylor, “Introduction to Error Analysis,” 2nd Edition, University Science Books, Sausalito,CA, (1997).

[112] S. P. Fu, T. T. Chen, and Y. F. Chen, “Photoluminescent properties of InN epifilms,” Semicond. Sci. Technol. **21**, 244 (2006).

[113] T. Shmidt, K. Lischka, and Zulehner, “Excitation-power dependence of the near-band-edge photoluminescence of semiconductors,” Phys. Rev. B **45**, 8989 (1992).

[114] G. Kresse, and J. Furthmüller, “Efficient iterative schemes for ab initio total energy calculations using a plane-wave basis set,” Phys. Rev. B **54**, 11169 (1996).

[115] E. A. Braude, J. S. Fawcett, and C. J. Timmons, “Fluorescence and the Beer-Lambert law- a note on the technique of absorption spectrophotometry,” J. Chem. Soc. 1019 (1950).

[116] J. Wu, W. Walukiewicz, W. Shan, K. M. Yu, J. W. Ager, S. X. Li, E. E. Haller, H. Lu, and W. J. Schaff, “Temperature dependence of the fundamental band gap of InN,” J. Appl. Phys. **94**, 4457 (2003).

[117] Y. Z. Yao, T. Sekiguchi, N. Ohashi, Y. Adachi, and T. Ohgaki, “Photoluminescence and x-ray diffraction measurements of InN epi-films grown with varying In/N ratio by plasma-assisted molecular-beam epitaxy,” App. Phys. Lett. **92**, 211910 (2008).

[118] G. D. Mahan, “Phonon-broadened optical spectra - Urbachs rule,” Phys. Rev. **145**, 602 (1966).

[119] J. Segura-Ruiz, N. Garro, A. Cantarero, C. Denker, J. Malindretos, and A. Rizzi, “Optical studies of MBE-grown InN nanocolumns: Evidence of surface electron accumulation,” Phys. Rev B **79**, 115305 (2009).

[120] Y-.L. Chang, Z. Mi, and F. Li, "Photoluminescence properties of a nearly intrinsic single InN nanowire," Adv. Funct. Mater **20**, 4146 (2010).

[121] R. E. Jones, S. X. Li, K. M. Yu, J. W. Ager, E. E. Haller, W. Walukiewicz, H. Lu, and W. J. Schaff, "Properties of native point defects in In1-xAlxN alloys," J. Phys. D-appl. Phys. **42**, 095406 (2009).

[122] Z. Yu, S. L. Buczkowski, N. C. Giles, T. H. Myers, and M. R. Richards-Babb, "The effect of atomic hydrogen on the growth of gallium nitride by molecular beam epitaxy," Appl. Phys. Lett. **69**, 2731 (1996).

[123] W. –L. Chen, R. L. Gunshor, J. Han, K. Higashimine, and N. Otsuka, "Growth of InN by MBE," MRS Internet J. Nitride Semicond. Res. 5S1, W3.30 (2000).

[124] K. Xu, and A. Yoshikawa, "Effects of film polarities on InN growth by molecular beam epitaxy," Appl. Phys. Lett. **83**, 251 (2003).

[125] T. Yamaguchi, K. Mizuo, Y. Saito, T. Noguchi, T. Araki, and Y. Nanishi, "Single crystalline InN films grown on Si substrates by using a brief substrate nitridation process materials," Mat. Res. Soc. Symposium Proceedings **743**, L3.26.1 (2003).

[126] M. Amirhoseiny, Z. Hassan, S. S. Ng, and M. A. Ahmad, "Characterizations of InN thin films grown on Si(110) substrate by reactive sputtering," J. Nanomat. **2011**, 7 (2011)

[127] P. A. Anderson, C. E. Kendrick, R. J. Kinsey, A. Asadov, W. Gao, R. J. Reeves, and S. M. Durbin, "(111) and (100) YSZ as substrates for indium nitride growth," Phys. Stat. Sol. c **2**, 2320 (2005).

[128] S.-G. Lee and K. J. Chang, "Atomic model for blue luminescences in Mg-doped GaN," Semicond. Sci. Technol. **14**, 138 (1998).

[129] M. E. Zvanut, D. M. Matlock, R. L. Henry, D. Koleske, and A. Wickenden, "Thermal activation of Mg-doped GaN as monitored by electron paramagnetic resonance spectroscopy," J. Appl. Phys. **95**, 1884 (2004).

[130] P. Ruterana, M. Albrecht, and J. Neugebauer, "Nitride Semiconductors Handbook on Materials and Devices," Weiheim: WILEY-VCH (2003).

[131] A. V. Blant, T. S. Cheng, N. J. Jeffs, L. B. Flannery, I. Harrison, J. F. W. Mosselmans, A. D. Smith, and C. T. Foxon, "EXAFS studies of Mg doped InN grown on Al_2O_3," Mat. Sci. Eng. (b) **59**, 218 (1999).

[132] R. E. Jones, K. M. Yu, S. X. Li, W. Walukiewicz, J. W. Ager, E. E. Haller, H. Lu, and W. J. Schaff, "Evidence for p-type doping of InN," Phys. Rev. Lett. **96**, 125505 (2006).

[133] X. Wang, S.-B. Che, Y. Ishitani, and A. Yoshikawa, "Growth and properties of Mg-doped In-polar InN films," Appl. Phys. Lett. **90**, 201913 (2007).

[134] X. Wang, S.-B. Che, Y. Ishitani, A. Yoshikawa, H. Sasaki, T. Shinagawa, and S. Yoshida, "Polarity inversion in high Mg-doped In-polar InN epitaxial layers," Appl. Phys. Lett. **91**, 081912 (2007).

[135] X. Wang, S.-B. Che, Y. Ishitani, and A. Yoshikawa, "Systematic study on p-type doping control of InN with different Mg concentrations in both In and N polarities," Appl. Phys. Lett. **91**, 242111 (2007).

[136] X. Wang, S. Che, Y. Ishitani, and A. Yoshikawa, "Hole mobility in Mg-doped p-type InN films," Appl. Phys. Lett. **92**, 132108 (2008).

[137] M. Bockowski, P. P. Strak, P. P. Kempisty, I. I. Grzegory, B. B. Lucznik, S. Krukowski, and S. S. Porowski, "Liquid phase epitaxy of GaN on MOCVD GaN of sapphire and HVPE free-standing substrates under high nitrogen pressure," Phys. Stat. Sol. c **5,** 1539 (2008).

[138] M. A. Herman, and H. Sitter, "Molecular beam epitaxy fundamentals and current status," Spring series in Mat. Sci. **7** (1996).

[139] H. Lu, W. J. Schaff, J. Hwang, H. Wu, G. Koley, and L. F. Eastman, "Effect of an AlN buffer layer on the epitaxial growth of InN by molecular-beam epitaxy," Appl. Phys. Lett. **79**, 1489 (2001).

[140] S. Yamaguchi, M. Kariya, S. Nitta, T. Takeuchi, C. Wetzel, H. Amano, and I. Akasaki, "Structural properties of InN on GaN grown by metalorganic vapor phase epitaxy," J. Appl. Phys. **85**, 7682 (1999).

[141] V. Cimalla, V. Lebedev, F. M. Morales, M. Niebelschutz, G. Ecke, R. Goldhahn, and O. Ambacher, "Origin of n-type conductivity in nominally undoped InN," Materialwissenschaft und Werkstofftechnik **37**, 924 (2006).

[142] C. H. Swartz, R. P. Tompkins, N. C. Giles, T. H. Myers, H. Lu, W. J. Schaff, and L. F. Eastman, "Investigation of multiple carrier effects in InN epilayers using variable magnetic field Hall measurements," J. Cryst. Growth **269**, 29 (2004).

[143] C. S. Gallinat, G. KoblmÄuller, J. S. Brown, S. Bernardis, J. S. Speck, G. D. Chern, E. D. Readinger, H. Shen, and M. Wraback, "In-polar InN grown by plasma-assisted molecular beam epitaxy," Appl. Phys. Lett. **89**, 032109 (2006).

[144] E. Haus, I. P. Smorchkova, B. Heying, P. Fini, C. Poblenz, T. Mates, U. K. Mishra, and J. S. Speck, "The role of growth conditions on the p-doping of GaN by plasma-assisted molecular beam epitaxy," J. Cryst. Growth **246**, 55 (2002).

[145] V. Y. Davydov, A. A. Klochikhin, A. N. Smirnov, I. Y. Strashkova, A. S. Krylov, H. Lu, W. J. Schaff, H. M. Lee, Y. L. Hong, and S. Gwo, "Selective excitation of E(1)(LO) and A(1)(LO) phonons with large wave vectors in the Raman spectra of hexagonal InN," Phys. Rev. B **80**, 081204 (2009).

[146] L. H. Dmowski, M. Baj, T. Suski, J. Przybytek, R. Czernecki, X. Wang, A. Yoshikawa, H. Lu, W. J. Schaff, D. Muto, and Y. Nanishi, "Search for free holes in InN:Mg-interplay between surface layer and Mg-acceptor doped interior," J. Appl. Phys. **105**, 123713 (2009).

[147] S. Nargelas, R. Aleksiejunas, M. Vengris, T. Malinauskas, K. Jarasiunas, and E. Dimakis, "Dyanmics of free carrier absorption in InN layers," Appl. Phys. Lett. **95**, 162103 (2009).

[148] G. Shigaura, M. Ohashi, Y. Ichinohe, M. Kanamori, N. Kimura, N. Kimura, T. Sawada, K. Suzuki, and K. Imai, "Deep emission of MBE-ZnTe on tilted GaAs substrate," J. Cryst. Growth **301**, 297 (2007).

[149] W.Walukiewicz, "Amphoteric native defects in semiconductors," Appl. Phys. Lett. **54**, 2094 (1989).

[150] R. E. Jones, S. X. Li, K. M. Yu, J. W Ager III, E. E. Haller, W. Walukiewicz, H. Lu, and W. J. Schaff, "Properties of native point defects in $In_{1-x}Al_xN$ alloys," J. Phys. D: Appl. Phys. **42**, 095406 (2009).

[151] F. Urbach, "The long-wavelength edge of photographic sensitivity and of the electronic absorption of solids," Phys. Rev. **92**, 1324 (1953).

[152] R. Chen, G. Z. Xing, J. Gao, Z. Zhang, T. Wu, and H. D. Sun, "Characteristics of ultraviolet photoluminescence from high quality tin oxide nanowires," Appl. Phys. Lett. **95**, 061908 (2009).

[153] K. –F. Berggren, and B. E. Sernelius, "Band-gap narrowing in heavily doped many-valley semiconductors," Phys. Rev. B **24**, 1971 (1981).

[154] G. W. Shu, P. F. Wu, Y. W. Liu, J. S. Wang, J. L. Shen, T. Y. Lin, P. J. Pong, G. C. Chi, H. J. Chang, and Y. C. Lee, "Effects of rapid thermal annealing on the optical and electrical properties of InN epilayers," J. Phys: Condens. Matter **18**, L543 (2006).

[155] A. Yoshikawa, X. Wang, Y. Ishitani, and A. Uedono, “Recent advances and challenges for successful p-type control of InN films with Mg acceptor doping by molecular beam epitaxy,” Phys. Stat. Sol. a **207**, 1011 (2010).

[156] C. S. Gallinat, G. Koblüller, J. S. Brown, and J. S. Speck, “A growth diagram for plasma-assisted molecular beam epitaxy of In-face InN,” J. Appl. Phys. **102**, 064907 (2007).

[157] A. Bhattacharyya, W. Li, J. Cabalu, T. D. Moustakas, D. J. Smith, and R. L. Hervig, “Efficient *p*-type doping of GaN films by plasma-assisted molecular beam epitaxy,” Appl. Phys. Lett. **85**, 4956 (2004).

[158] A. Yoshikawa, S. Che, Y. Ishitani, and X. Wang, “Advances in InN epitaxy and its material control by MBE towards novel InN-based QWs,” Journal of Crystal Growth **311,** 2073 (2009).

[159] V. V. Mamutin, V. A. Vekshin, V. Y. Davydov, V. V. Ratnikov, Y. A. Kudriavtsev, B. Y. Ber, V. V. Emtsev, and S. V. Ivanov, “Mg-doped hexagonal InN/Al_2O_3 films grown by MBE,” Phys. Stat. Sol. a, Applied Research **176,** 373 (1999).

[160] P. D. C. King, T. D. Veal, H. Lu, S. A. Hatfield, W. J. Schaff, and C. F. McConville, “The influence of conduction band plasmons on core-level photoemission spectra of InN,” Surface Science **602,** 871 (2008).

[161] M. C. Gold, and D. A. Nelson, “Variable magnetic field Hall effect measurements and analyses of high purity, Hg vacancy (p-type) HgCdTe,” J. Vac. Sci&Technol A **4**, 2040 (1986).

[162] V. A. Vilkotskii, D. S. Domanevskii, R. D. Kakankow, V. V. Krasovskii, and V. D. Tkachev, “Bustein-Moss effect and near-band-edge luminescence spectrum of highly doped indium arsenide,” Phys. Stat. Sol (b) **91**, 71 (1979).

[163] I. D. Abella, “Optical double-photon absorption in Cesium vapour,” Phys. Rev. Lett. **9**, 453 (1962).

[164] J. Antoszewski, D. J. Seymour, L. Faraone, J. R. Meyer, and C. A. Hoffman, “Magneto-transport characterization using quantitative mobility-spectrum,” J. Elec. Mat. **24**, 1255 (1995).

[165] P. D. C. King, T. D. Veal, and C. F. McConville, “Unintentional conductivity of indium nitride: transport modeling and microscopic origins,” Journal of Physics-Condensed Matter **21,** 174201 (2009).

[166] J. R. Meyer, C. A. Hoffman, F. J. Bartoli, D. A. Arnold, S. Sivananthan, and J. P. Faurie, “Methods for magnetotransport characterization of IR detector materials,” Semiconductor Science and Technology **8,** 805 (1993).

[167] W. A. Beck and J. R. Anderson, “Determination of electrical transport properties using a novel magnetic field-dependent Hall technique,” Journal of Applied Physics **62,** 541 (1987).

[168] M. Moret, S. Ruffenach, O. Briot, and B. Gil, “The determination of the bulk residual doping in indium nitride films using photoluminescence,” Appl. Phys. Lett. **95**, 031910 (2009).

[169] S. Jin, Y. Zheng, and A. Li, “Characterization of photoluminescence intensity and efficiency of free excitons in semiconductor quantum well structures,” J. Appl. Phys. **82**, 8 (1997).

[170] X.-B. Chen, J. Huso, J. L. Morrison, and L. Bergman, “Dynamics of GaN band edge photoluminescence at near-room-temperature regime,” J. Appl. Phys. **99**, 046105 (2006).

[171] X.-B. Chen, J. Huso, J. L. Morrison, and L. Bergman, “The properties of ZnO photoluminescence at and above room temperature,” J. Appl. Phys. **102**, 116105 (2007).

[172] I. P. Smorchkova, E. Haus, B. Heying, P. Kozodoy, P. Fini, J. P. Ibbetson, S. Keller, S. P. DenBaars, J. S. Speck, and U. K. Mishra, “Mg doping of GaN layers grown by plasma-assisted molecular-beam epitaxy,” Appl. Phys. Lett. **76**, 718 (2000).

[173] A. Feduniewicz, C. Skierbiszewski, M. Siekacz, Z. R. Wasilewski, I. Sproule, S. Grzanka, R. Jakieła, J. Borysiuk, G. Kamler, E. Litwin-Staszewska, R. Czernecki, M. Boćkowski, and S. Porowski, " Control of Mg doping of GaN in RF-plasma molecular beam epitaxy," J. Cryst. Growth **278**, 443 (2005).

[174] L. K. Li, M. J. Jurkovic, W. I. Wang, J. M. Van Hove, and P. P. Chow, "Surface polarity dependence of Mg doping in GaN grown by molecular-beam epitaxy," Appl. Phys. Lett. **76**, 1740 (2000).

[175] C. –L. Hsiao, H. –C. Hsu, L. –C. Chen, C. –T. Wu, C. –W. Chen, M. Chen, L. –W. Tu, K. –H. Chen, "Photoluminescence spectroscopy of nearly defect-free InN microcrystals exhibiting nondegenerate semiconductor bahaviours," Appl. Phys. Lett. **91**, 181912 (2007).

[176] C. S. Gallinat, G. Koblmüller, F. Wu, J. S. Speck, "Evaluation of threading dislocation densities in In- and N-face InN," J. Appl. Phys. **107**, 053517 (2010).

[177] J. R. Dixon, "Anomalous Electrical Properties of p-Type Indium Arsenide," J. Appl. Phys. **30**, 1412 (1959).

[178] I. Melngailis and R. H. Rediker, "Properties of InAs Lasers," J Appl. Phys. **37**, 899 (1966).

[179] F. Ermanis and K. Wolfstirn, "Hall Effect and Resistivity of Zn-Doped GaAs," J Appl. Phys. **37**, 1963 (1966).

[180] P. J. Dean, E. G. Schönherr, and R. B. Zetterstrom, "Pair Spectra Involving the Shallow Acceptor Mg in GaP," J. Appl. Phys. **41**, 3475 (1970).

[181] J. I. Pankove and P. E. Norris, "Luminescence from GaN MIS diodes," R.C.A. Review **33**, 377 (1972).

[182] B. Monemar, O. Lagerstedt, and H. P. Gislason, “Properties of Zn-doped VPE-grown GaN. I. Luminescence data in relation to doping conditions,” J. Appl. Phys. **51**, 625 (1980).

[183] N. I. Kuznetsov, A. E. Nikolaev, A. S. Zubrilov, Y. V. Melnik, and V. A. Dmitriev, “Insulating GaN:Zn layers grown by hydride vapor phase epitaxy on SiC substrates,” Appl. Phys. Lett. **75**, 3138 (1999).

[184] L.-C. Chen, W.-H. Lan, R.-M. Lin, H.-T. Shen, and H.-C. Chen, “Optical properties of *In*2*O*3 oxidized from InN deposited by reactive magnetron sputtering,” Appl. Surf. Sci. **252**, 8438 (2006).

[185] L.-C. Chen and H.-C. Chen, “Annealing characteristics of Zn-doped InN Films on sapphire substrates by reactive magnetron sputtering,” Jpn. J. Appl. Phys. Part 1, **44**, 2995 (2005).

[186] H. Song, A. Yang, R. Zhang, Y. Guo, H. Wei, G. Zheng, S. Yang, X. Liu, Q. Zhu, and Z. Wang, “Well-aligned Zn-doped InN nanorods grown by metal-organic chemical vapor deposition and dopant distribution,” Gryst. Growth & design **9**, 3292 (2009).

[187] A. Ney, R. Rajaram, E. Arenholz, J. S. Harris Jr, M. Samant, R. F. C. Farrow, and S. S. P. Parkin, Journal of Magnetism and Magnetic Materials **300,** 7 (2006).

[188] G. Bastard, C. Rigaux, and A. Mycielski, “Giant spin splitting induced by exchange interactions in $Hg_{1-k}Mn_kTe$ mixed crystals,” Phys. stat. sol. b **79**, 585 (1977).

[189] H. Ohno, H. Munekata, T. Penny, S. von Molnár, and L. L. Chang, “Magnetotransport properties of p-type (In,Mn)As diluted magnetic III-V semiconductors,” Phys. Rev. Lett. **68**, 363 (1996).

[190] M. Oestreich, J. Hübner, D. Hägele, P. J. Klar, W. Heimbrodt, W. W. Rühle, D. E. Ashenford, and B. Lunn, “Spin injection into semiconductors,” Appl. Phys. Lett. **74**, 1251 (1999).

[191] M. Frazier, R. N. Kini, K. Nontapot, G. A. Khodaparast, T. Wojtowicz, X. Lie, and J. K. Furdyna, “Time resolved magneto-optical studies of ferromagnetic InMnSb films, “Appl. Phys. Lett. **92**, 061911 (2008).

[192] P. P. Chen, H. Makino, and T. Yao, “InN:Mn: a nitride-based diluted magnetic semiconductor,” Sol. State. Comm. **130**, 25 (2004).

[193] S. Granville, B. J. Ruck, A. R. H. Preston, T. Stewart, F. Budde, H. J. Trodahl, A. Bittar, J. E. Downes, and M. Ridgway, “Electronic properties of (Ga,Mn)N thin films with high Mn content,” J. Appl. Phys. **104**, 103710 (2008).

[194] H. Ohno, A. Shen, F. Matsukura, A. Oiwa, A. Endo, S. Katsumoto, and Y. Iye, “(Ga,Mn)As: A new diluted magnetic semiconductor based on GaAs,” Appl. Phys. Lett. **69**, 363 (1996).

[195] S. J. Pearton, C. R. Abernathy, D. P. Norton, A. F. Hebard, Y. D. Park, L. A. Boatner, and J. D. Budai, “Advances in wide bandgap materials for semiconductor spontronics,” Mater. Sci. Eng R **40,** 137 (2003).

[196] T. Dietl, H. Ohon, and F. Matsukura, “Hole-mediated ferromagnetism in tetrahedrally coordinated semiconductors,” Phys. Rev. B. **63**, 195205 (2001).

[197] Y. Endo, T. Sato, A. Takita, Y. Kawamura, and M. Yamamoto, “Magnetic, electrical properties, and structure of Cr-AlN and Mn-AlN thin films grown on Si substrates,” IEEE transactions on Magnetics **41**, 2718 (2005).

[198] R. Frazier, G. Thaler, M. Overberg, B. Gila, C. R. Abernathy, and S. J. Pearton, “Indication of hysteresis in AlMnN,” Appl. Phys. Lett. **83**, 1758 (2003).

[199] A. Ney, R. Rajaram, R. F. C. Farrow, J. S. Harris, Jr., and S. S. P. Parkin, “A promising diluted magnetic semiconductor material,” J. Supercond. **18**, 41 (2005).

[200] C. T. Foxon, S. V. Novikov, L. X. Zhao, K. W. Edmonds, A. D. Giddings, K. Y. Wang, R. P. Campion, C. R. Staddon, M. W. Fay, Y. Han, P. D. Brown, M. Sawicki, and B. L. Gallagher, “Molecular beam epitaxy of p-type cubic GaMnN layers,” J. Cryst. Growth **278**, 685 (2005).

[201] Z. Sofer, D. Sedmidubsky, J. Stejskal, J. Hejmanek, M. Marygsko, K. Jurek, M. Vaclavu, V. Havranek, and A. Mackova, “Growth and characterization of GaN:Mn layers by MOVPE,” J. Cryst. Growth **310**, 5025 (2008).

[202] Y. H. Kim, J. Jeong, K. S. Lee, J. K. Park, Y. J. Baik, T. Y. Seong, and W. M. Kim, “Characteristics of ZnO:Al thin films co-doped with hydrogen and fluorine,” Appl. Surf. Sci. **256**, 5102 (2010).

[203] P. D. C. King, T. D. Veal, and C. F. McConville, “Unintentional conductivity of indium nitride: transport modeling and microscopic origins,” J. Phys.: Cond. Matt. **21**, 174201 (2009).

[204] L. Y. Chen, and C. S. Ting, “Theoretical investigation of noise characteristics of double-barrier resonant-tunneling systems,” Phys. Rev. B **43**, 4534 (1991)

[205] L. Landin, H. Pettersson, M. Kleverman, M.Borgström, X. Zhang, W. Seifert, and L. Samuelson, “Interband transitions in InAs quantum dots in InP studied by photoconductivity and photoluminescence techniques,” J. Appl. Phys. **95**, 8007 (2004).

[206] Z. C. Huang, D. B. Mott, P. K. Shu, R. Zhang, J. C. Chen, and D. K. Wickenden, “Optical quenching of photoconductivity in GaN photoconductors,” J. Appl. Phys. **82**, 2707 (1997).

[207] H. A. Washburn, J. R. Sites, and H. H. Wieder, “Electronic profile of *n*-InAs on semi-insulating GaAs,” J. Appl. Phys. **50**, 4872 (1979).

[208] J. H. Chai, T. H. Myers, Y.-W. Song, R. J. Reeves, W. M. Linhart, R. J. H. Morris, T. D. Veal, M. G. Dowsett, and S. M. Durbin, “MBE growth and characterization of Mn-doped

InN," J. Vac. Sci. Technol. B **30**, 02B124 (2012).

[209] M. S. Skolnick, J. M. Rorison, K. J. Nash, D. J. Mowbray, P. R. Tapster, S. J. Bass, and A. D. Pitt, "Observation of a many-body edge singularity in quantum-well luminescence spectra," Phys. Rev. Lett. **58**, 2130 (1987).

[210] F. Fuchs, K. Kheng, P. Koidl, and K. Schwarz, "Fermi-edge singularity in degenerate *n*-type bulk InAs," Phys. Rev. B **48**, 7884 (1993).

[211] P. J. Dean, E. G. SchÄonherr, and R. B. Zetterstrom, "Pair Spectra Involving the Shallow Acceptor Mg in GaP," J. Appl. Phys. **41**, 3475 (1970).

[212] H. Lu, W. J. Schaff, L. F. Eastman, J. Wu, W. Walukiewicz, D. C. Look, and R. J. Molnar, "Growth of thick InN by molecular beam epitaxy," Mat. Research. Soc. Symp. Proceedings **734**, 317 (2003).

[213] H. KatayamaYoshida, and K. Sato, "Material design for semiconductor spintronics by ab-initio electronic-structure calculation," Physica B **327**, 337 (2003).

[214] B. Bansal, "A model for the temperature dependence of photoluminescence from self-assembled quantum dots," J. Appl. Phys. **100**, 093107 (2006).

[215] Z. Yang, and J. L. Liu, "Donor-acceptor-pair photoluminescence in Ga-doped ZnO thin films grown by plasma-assisted molecular beam epitaxy," J. Vac. Sci. Technol. B **28**, 1071 (2010).

[216] O. Bierwagen, S. Choi, and J. S. Speck, "Hall and Seebeck measurement of a p-n layer stack: Determining InN bulk hole transport properties in the presence of a strong surface electron accumulation layer," Phys. Rev B **85**, 165205 (2012).

[217] T. S. Jeong, C. J. Youn, M. S. Han, J. W. Yang, and K. Y. Lim, "Analysis of Mg-related emissions in p-GaN grown by MOCVD," J. Cryst. Growth **259**, 267 (2003).

[218] K. B. Nam, M. L. Nakarmi, J. Li, J. Y. Lin, and H. X. Jiang, "Mg acceptor level in AlN probed by deep ultraviolet photoluminescence," Appl. Phys. Lett. **83**, 878 (2003).

[219] M. Leroux, N. Grandjean, B. Beaumont, G. Nataf, F. Semond, J. Massies, and P. Gibart, "Temperature quenching of photoluminescence intensities in undoped and doped GaN," J. Appl. Phys. **86**, 3721 (1999).

[220] E. Calleja, M. A. Sánchez-Garćia, F. Calle, F. B. Naranjo, E. Muñoz, U. Jahn, K. Ploog, J. Sánchez, J. M. Calleja, K. Saarinen, P. Hautojärvi, "Molecular beam epitaxy growth and doping of III-nitrides on Si (111): layer morphology and doping efficiency," Mater. Sci and Eng. B **82**, 2 (2001).

[221] P. Kozodoy, H. Xing, S. P. DenBaars, U. K. Mishra, A. Saxier, R. Perrin, S. Elhamri, and W. C. Mitchel, "Heavy doping effects in Mg-doped GaN," J. Appl. Phys. **87**, 1832 (2000).

[222] E. Kurtz, S. Einfeldt, J. Nürnberger, S. Zerlauth, D. Hommel, and G. Landwehr, "p-type doping of ZnSe. On the properties of nitrogen in ZnSe:N," Phys. Status Solidi B **187**, 393 (1995).

[223] H. P. Gislason, B. H. Yang, and M. Linnarsson, "Shifting photoluminescence bands in high-resistivity Li-compensated GaAs," Phys. Rev. B **47**, 9418 (1993).

[224] L. Eckey, U. v. Gfug, J. Holst, A. Hoffmann, A. Kaschner, H. Siegle, C. Thomsen, B. Schineller, K. Heime, M. Heuken, O. Schoen, and R. Beccard, "Photoluminescence and Raman study of compensation effects in Mg-doped GaN epilayers," J. Appl. Phys. **84**, 5828 (1998).

[225] K. Thonke, Th. Gruber, N. Teofilov, R. Schönfelder, A. Waag, and R. Sauer, "Donor-acceptor pair transitions in ZnO substrate material," Physica B **308-310**, 945 (2001).

[226] F. Mireles, and S. E. Ulloa, “Acceptor binding energies in GaN and AlN,” Phys. Rev. B **58**, 3879 (1998).

[227] V. M. Andreev, M. N. Petrov, and I. G. Pichugin, “Doping mechanism and properties of Zn-doped GaN-epitaxial layers,” Cryst. Res. Technol. **18**, 435 (1983).

[228] W. B. Joyce, R. W Dixon, “Analytic approximations for the Fermi energy of an ideal Fermi gas,” Appl. Phys. Lett. **31**, 354 (1977).

[229] S. M. Sze, and K. K. Ng, “Physics of Semiconductor Devices,” John Wiley & Sons, Inc. (2007).

[230] H. Tang, W. Kim, A. Botchkarev, G. Popovici, F. Hamdani, and H. Morkoc, “Analysis of carrier mobility and concentration in Si-doped GaN grown by reactive molecular beam epitaxy,” Sol. Stat. Elec. **42**, 839 (1998).

[231] A. F. Wright, “Substitutional and interstitial carbon in wurtzite GaN,” J. Appl. Phys. **92**, 2575 (2002).

[232] J. T-Thienprasert, P. Reunchan, A, Janotti, and C. G. Van de Walle, “Carbon-nitrogen molecules in GaAs and GaP,” Phys. Rev. B **77**, 195209 (2008).

[233] U. Gosele, “Diffusion of zinc in gallium arsenide: A new model,” J. Appl. Phys. **52**, 4617 (1981).

[234] J. E. Northrup, “Screw dislocations in GaN: The Ga-filled core model,” Appl. Phys. Lett. **78**, 2288 (2001).

[235] Q. Yang, H. Feick, and E. R. Weber, “Observation of a hydrogenic donor in the luminescence of electron-irradiated GaN,” Appl. Phys. Lett. **82**, 3002 (2003).

[236] E. A. Davis, S. F. J. Cox, R. L. Lichti, and C. G. Van de Walle, “Shallow donor state of hydrogen in indium nitride,” Appl. Phys. Lett. **82**, 592 (2003).

[237] A. Y. Cho, and J. R. Arthur, “Molecular beam epitaxy,” Prog. Sol. Stat. Chem. **10**, 157 (1975).

[238] D. C. Look, H. Lu, W. J. Schaff, J. Jasinski, and Z. Liliental-Weber, “Donor and acceptor concentrations in degenerate InN,” Appl. Phys. Lett. **80**, 258 (2002).

[239] Z. Benzarti, I. Halidou, O. Tottereau, T. Boufaden, and B. El Jani, “Silicon effect on GaN surface morphology,” Microelectronic J. **33**, 995 (2002).

[240] L. Grenouillet, C. Bru-Chevallier, G. Guilot, P. Gilet, P. Duvaut, C. Vannuffel, A. Million, and A. Chenevas-Paule, “Evidence of strong carrier localization below 100 K in a GaInNAs/GaAs single quantum well,” Appl. Phys. Lett. **76**, 2241 (2000).

[241] A. Bell, S. Srinivasan, C. Plumlee, H. Omiya, F. A. Ponce, J. Christen, S. Tanaka, A. Fujioka, and Y. Nakagawa, “Exciton freeze-out and thermally activated relaxation at local potential fluctuations in thick $Al_xGa_{1-x}N$ layers,” J. Appl. Phys. **95**, 4670 (2004).

[242] D. Bimberg, M. Sondergeld, and E. Grobe, “Thermal dissociation of excitons bounds to neutral acceptors in high-purity GaAs,” Phys. Rev. B **4**, 3451 (1971).

[243] S. –N. Lee, T. Sakong, W. Lee, H. Paek, J. Son, E. Yoon, O. Nam, and Y. Park, “Characterization of optical and electrical quality of Mg-doped $In_xGa_{1-x}N$ grown by MOCVD,” J. Cryst. Growth **261**, 249 (2004).

[245] W. M. Linhart, J. Chai, R. J. H. Morris, M. G. Dowsett, C. F. McConville, S. M. Durbin, and T. D. Veal, “Giant reduction of InN surface electron accumulation: Compensation of surface donors by Mg dopants,” Phys. Rev. Lett. **109**, 247605 (2012).

[246] J. Krustok, H. Collan, and K. Hjelt, “Does the low-temperature Arrhenius plot of the photoluminescence intensity in CdTe point towards an erroneous activation energy?,” J. Appl. Phys. **81**, 1442 (1997).

[247] K. B. Nam, J. Li, J. Y. Lin, and H. X. Jiang, “Optical properties of AlN and GaN in elevated temperatures,” Appl. Phys. Lett. **85**, 3489 (2004).

[248] S. Fischer, C. Wetzel, E. E. Haller, B. K. Meyer, “On p-type doping in GaN-acceptor binding energies,” Appl. Phys. Lett. **67**, 1298 (1995).

[249] X. M. Duan, and C. Stampfl, “Defect complexes and cluster doping of InN: First-principles investigations,” Phys. Rev. B **79**, 035207 (2009).

[250] K. Kumakura, T. Makimoto, and N. Kobayashi, “High hole concentrations in Mg-doped InGaN grown by MOVPE,” J. Cryst. Growth **221**, 267 (2000).

[251] D. C. Herbert, “An extension of Haynes’ rule for bound excitons,” J. Phys. C: Sol. Stat. Phys. **17**, L901 (1984).

[252] S. E. Fred, “Light-Emitting Diodes,” 2nd edition: Cambridge University Press (2006).

[253] A. S. dos Santos, M. Masili, and J. J. De Groote, “Binding energies of excitons trapped by ionized donors in semiconductors,” Phys. Rev. B **64**, 195210 (2001).

[254] C. G. Van de Walle, and J. Neugebauer, “Universal alignment of hydrogen levels in semiconductors, insulators and solutions,” Nature **423**, 626 (2003).

[255] J. E. Fouguet, and A. E. Siegman, “Room-temperature photoluminescence times in a GaAs/Al_xGa_{1-x}As molecular beam epitaxy multiple quantum well structure,” Appl. Phys. Lett. **46**, 280 (1985).

[256] J. Tersoff, “Theory of semiconductor heterojunctions: The role of quantum dipoles,” Phys. Rev. B **30**, 4874 (1984).

[257] W. Zimmerman, “Experimental verification of Shockley-Read-Hall recombination theory in silicon,” Elec. Lett. **9**, 378 (1973).